Multidisciplinary Design Optimization
of a Strut-Braced Wing Aircraft

Joel M. Grasmeyer

Thesis submitted to the Faculty of the

Virginia Polytechnic Institute and State University

in partial fulfillment of the requirements for the degree of

Master of Science

in

Aerospace Engineering

W.H. Mason, Chair

B. Grossman

J.A. Schetz

April 13, 1998

Blacksburg, Virginia

Keywords: Multidisciplinary Design Optimization, Aircraft Design,
Strut-Braced Wing, Tip-Mounted Engines

Multidisciplinary Design Optimization
of a Strut-Braced Wing Aircraft

Joel M. Grasmeyer

(ABSTRACT)

The objective of this study is to use Multidisciplinary Design Optimization (MDO) to investigate the use of truss-braced wing concepts in concert with other advanced technologies to obtain a significant improvement in the performance of transonic transport aircraft. The truss topology introduces several opportunities. A higher aspect ratio and decreased wing thickness can be achieved without an increase in wing weight relative to a cantilever wing. The reduction in thickness allows the wing sweep to be reduced without incurring a transonic wave drag penalty. The reduced wing sweep allows a larger percentage of the wing area to achieve natural laminar flow. Additionally, tip-mounted engines can be used to reduce the induced drag. The MDO approach helps the designer achieve the best technology integration by making optimum trades between competing physical effects in the design space.

To perform this study, a suite of approximate analysis tools was assembled into a complete, conceptual-level MDO code. A typical mission profile of the Boeing 777-200IGW was chosen as the design mission profile. This transport carries 305 passengers in mixed class seating at a cruise Mach number of 0.85 over a range of 7,380 nmi.

Several single-strut configurations were optimized for minimum takeoff gross weight, using eighteen design variables and seven constraints. The best single-strut configuration shows a 15% savings in takeoff gross weight, 29% savings in fuel weight, 28% increase in L/D, and a 41% increase in seat-miles per gallon relative to a comparable cantilever wing configuration.

In addition to the MDO work, we have proposed some innovative, unconventional arch-braced and ellipse-braced concepts. A plastic solid model of one of the novel configurations was created using the *I-DEAS* solid modeling software and rapid prototyping hardware.

Acknowledgments

This research would not have been possible without the help of many individuals and institutions. I am grateful to my advisor, Dr. William Mason, who helped me build a conceptual-level aircraft design code from the ground up. His familiarity with the aerospace literature and his deep archives of design software were very beneficial to this research. His design intuition was also useful in refining the design algorithms to reflect reality.

All of the members of the truss-braced wing team have contributed in important ways to this work. I am grateful to Dr. Bernard Grossman for his many helpful comments on the written material related to this research, and for always being open to new ideas. I thank Dr. Joseph Schetz for his many insightful comments, and for keeping the group focused on the big picture. I thank Dr. Rakesh Kapania for his helpful and often humorous advice on structures and on the meaning of life. Finally, I owe many thanks to Dr. Raphael Haftka, from the University of Florida for his "virtual presence" via the teleconferencing, the World Wide Web, and e-mail. His brilliant suggestions often defined new directions for the research, and his astute intuition prevented us from wandering down many blind alleys in this research.

I also owe a debt of thanks to my fellow student members on the team. Amir Naghshineh-Pour persevered through many demanding situations to provide the wing bending material weight subroutine that was so essential to this research. Philippe-Andre Tetrault has done a superb job of investigating the transonic interference drag with computational fluid dynamics. His pioneering work in this area has given us many insights into the nature of the flow at the wing-strut intersection. Erwin Sulaeman joined the truss-braced wing team in the Spring of 1998. In a very short time he has made an amazing amount of progress toward evaluating the aeroelastic effects of the strut-braced wing configuration. Mike Libeau participated in this research as an undergraduate work-study student. In a few short months, Mike created a rapid prototyping model of one of the strut-braced wing concepts, and he wrote a subroutine to convert the configuration parameters to a DXF file for the creation of rendered images of the

Contents

List of Figures

List of Tables

Nomenclature

b	wing span
c	local chord
$c_{d_{cl}}$	interference drag coefficient due to the lift coefficient
$c_{d_{inclin}}$	interference drag coefficient due to the inclination angle
$c_{d_{int\,wing\text{-}fuse}}$	interference drag coefficient of a wing-fuselage intersection
$c_{d_{int\,wing\text{-}strut}}$	interference drag coefficient of a wing-strut intersection
$c_{d_{strut}}$	interference drag coefficient of a perpendicular wing-strut intersection
$c_{d_{sweep}}$	interference drag coefficient due to sweep
$c_{d_{wall}}$	interference drag coefficient of a perpendicular wing-wall intersection
$c_{d_{wave}}$	wave drag coefficient for a spanwise strip
C_l	variation in rolling moment coefficient with sideslip angle
$C_{l\,a}$	variation in rolling moment coefficient with aileron deflection
$C_{l\,,}$	variation in rolling moment coefficient with rudder deflection
C_n	variation of yawing moment coefficient with sideslip angle
$C_{n\,a}$	variation of yawing moment coefficient with aileron deflection
$C_{n\,,}$	variation of yawing moment coefficient with rudder deflection
C_y	variation of sideforce coefficient with sideslip angle
$C_{y\,a}$	variation of sideforce coefficient with aileron deflection
$C_{y\,,}$	variation of sideforce coefficient with rudder deflection
C_D	aircraft drag coefficient
$C_{D_{cruise}}$	aircraft drag coefficient at the initial cruise condition
$C_{n_{avail}}$	available yawing moment coefficient at the engine-out flight condition
$C_{n_{req}}$	required yawing moment coefficient at the engine-out flight condition
c_l	section lift coefficient
C_L	aircraft lift coefficient
d_{actual}	diameter of the rubber engine
$d_{baseline}$	diameter of the baseline engine
D_{cruise}	aircraft drag at the initial cruise condition
D_{ewm}	drag due to windmilling of failed engine
F_v	lateral force provided by the vertical tail
l_{actual}	length of the rubber engine
$l_{baseline}$	length of the baseline engine
l_e	engine moment arm (distance from fuselage centerline to engine centerline)
l_{tv}	horizontal distance between CG and engine nozzle
l_{vtail}	horizontal distance between CG and aerodynamic center of vertical tail

L/D	lift-to-drag ratio
L_{ext}	external rolling moment
M	Mach number
M_{crit}	critical Mach number
M_{dd}	drag-divergence Mach number
$n_{engines_{fuse}}$	number of engines on the fuselage
$n_{engines_{wing}}$	number of engines on the wing
q	dynamic pressure
q_{cruise}	dynamic pressure at cruise
$range$	aircraft design range
$reserve$	reserve range
S_{ref}	reference area
S_{strip}	area of a spanwise strip
S_{vtail}	vertical tail area
sfc_{cruise}	specific fuel consumption at cruise altitude and Mach number
$sfc_{s,sl}$	specific fuel consumption at static, sea-level condition
t/c	thickness-to-chord ratio
T_{eo}	maximum engine thrust at the engine-out flight condition
$T_{baseline}$	baseline engine thrust (static, sea-level)
T_{cruise}	required thrust at the initial cruise condition
T_{req}	required thrust (static, sea-level)
$Temp_{cruise}$	temperature at cruise altitude
$Temp_{sl}$	temperature at sea-level
V	velocity
W_{engine}	baseline engine weight
$W_{engine_{calc}}$	calculated rubber engine weight
$W_{initial}$	initial cruise weight
W_{zf}	zero-fuel weight
W_{to}	takeoff weight
Y_{ext}	external sideforce
z_{tv}	vertical distance between CG and engine nozzle
z_{vtail}	vertical distance between CG and aerodynamic center of vertical tail
	sideslip angle (positive with relative wind from right)
$_a$	aileron deflection (positive for right up, left down)
$_r$	rudder deflection (positive right)
	thrust vectoring angle
	bank angle (positive right roll)
$_a$	airfoil technology factor
	sweep angle
	ratio of density at cruise altitude to density at sea level
$C_{L_{cc}}$	change in vertical tail lift coefficient due to circulation control

Chapter 1

Introduction

The cantilever wing configuration has dominated the design of large transonic transports since the introduction of the Boeing 707 in the 1950s. Modern transonic transports such as the Boeing 777 and the MD-11 still bear a strong resemblance to the Boeing 707. Many advances have been made in the design of large transports, but they have been evolutionary modifications of the original cantilever wing configuration. The truss-braced wing configuration offers the potential to make a revolutionary advance in the efficiency of the modern transport. The truss-braced wing concept embraces several synergistic design features to obtain a significant increase in performance. The structural efficiency of the truss allows the span to increase without an increase in wing weight or thickness (they may actually decrease). The increased span reduces the induced drag, and a decrease in thickness reduces the transonic wave drag and allows the wing sweep to be reduced. The reduced wing sweep and the smaller chord Reynolds numbers encourage natural laminar flow, which reduces the parasite drag [1]. Obtaining the most desirable trade-off between these effects requires the use of Multidisciplinary Design Optimization (MDO).

In the summer of 1996, Dennis Bushnell, Chief Scientist at the NASA Langley Research Center, challenged the Multidisciplinary Analysis and Design (MAD) Center at Virginia Tech to apply the MDO methodology to the design of a truss-braced wing configuration to seek a quantum increase in performance relative to the cantilever wing configuration. A multidisciplinary team of graduate students and faculty members was assembled to perform the

study. The author performed the aerodynamics, stability and control, and propulsion analyses. He also integrated the disciplines together in a computational MDO architecture. Amir Naghshineh-Pour performed the structural analysis and created a subroutine to calculate the bending material weight of an arbitrary wing/strut configuration. Philippe-Andre Tetrault performed a detailed Computational Fluid Dynamics (CFD) study of various wing-strut intersection geometries to evaluate the transonic effects of the interference drag. The newest member of the team, Erwin Sulaeman, is evaluating the aeroelasticity effects of the truss-braced wing configurations. The faculty members on this project were B. Grossman, R.T. Haftka (University of Florida), R.K. Kapania, W.H. Mason, and J.A. Schetz. The team met once per week to exchange information and discuss the progress of the work.

The idea of using a truss-braced wing for a long-range, transonic transport aircraft was first proposed by Werner Pfenninger at Northrop in the early 1950s [2]. He continued this work on and off until his retirement from NASA Langley in the late 1980s. A model of one of Pfenninger's configurations is shown in Figure 1-1. In the 1960s, Lockheed studied the use of a truss-braced wing on a C-5A fuselage for a long range military transport [3]. This design featured a wing with an aspect ratio of 20 and active tip controls for gust alleviation. In the late 1970s, Boeing studied the use of a truss-braced with laminar flow control for a very large (440 ft. span), long range military transport [4] and [5]. The Boeing study concluded that the truss-braced wing would have a slightly higher takeoff gross weight than a comparable cantilever wing configuration. In 1980, NASA performed a preliminary design study of a subsonic business jet employing a truss-braced wing with an aspect ratio of 25 [6]. The 1980 study showed that the truss-braced wing configuration had a 20% savings in fuel weight relative to a cantilever wing configuration. Another NASA study was performed in 1981 on the use of a truss-braced wing for a high-altitude manned research aircraft [7]. This study concluded that an optimum cantilever design had a 26% increase in range relative to a baseline cantilever design, while an optimum truss-braced wing had a 31% increase in range.

Figure 1-1: Pfenninger/NASA truss-braced wing concept (NASA photo)

The studies mentioned above have pointed out many of the critical design issues associated with the truss-braced wing configuration. However, none of these studies have been performed using a Multidisciplinary Design Optimization (MDO) methodology. Because of the tight coupling between aerodynamics and structures in the truss-braced wing design problem, an MDO approach is required to assess the true potential of the concept. The use of MDO for a wide variety of applications has been documented in survey papers by Ashley [8], Sobieski and Haftka [9], and Kroo [10]. MDO has also been applied to the design of the High-Speed Civil Transport at Virginia Tech [11], [12], and [13].

The truss-braced wing configuration can use tip-mounted engines to obtain a reduction in induced drag, as some studies have suggested [14] and [15]. The tip-mounted engines also provide added inertia relief for the wing structure. With the engines located at the wingtips, an engine failure would create a very large yawing moment. To maintain equilibrium flight at the engine-out flight condition, circulation control can be used on the vertical tail to increase its effectiveness. The circulation of the vertical tail airfoil can be controlled by blowing air through slots at the rear of an elliptical section, or by combining the slots with a deflecting flap for some redundancy. The air for blowing can be provided by the Auxiliary Power Unit (APU), which is already located in the tailcone. In their study of a circulation control stern plane for submarine applications, Englar and Williams [16] have shown that section lift coefficients of 2.8 are possible with a 20% ellipse. In normal flight, a small amount of blowing could be used to reduce the drag of the vertical tail, or even generate some thrust. The circulation control concept, together with a stability and control analysis, is used to incorporate the engine-out condition

3

explicitly as a constraint. The present model does not impose a weight penalty for the circulation control mechanism.

Thrust vectoring with a third engine mounted at the base of the vertical tail was also investigated as a means to handle the engine-out condition. We found that the relatively small deflection angle allowed by thrust vectoring (15°) was not sufficient to generate a large enough yawing moment. The extra weight, maintenance, cost, and complexity of the third engine also discouraged the use of thrust vectoring.

The buckling of the strut under the -1 g load condition proved to be the critical structural design challenge in the single-strut configuration. To address this issue we allow the strut to be inactive in compression, and we optimize the strut force at the 2.5 g load condition. The configurations presented in this thesis were optimized with no aeroelastic constraints.

To perform the truss-braced wing study, a suite of approximate analysis tools was assembled into a complete, conceptual-level MDO code capable of evaluating both strut-braced and cantilever wing configurations. The initial truss-braced wing studies have been performed with a single-strut-braced wing configuration, since it is the most basic representation of the truss-braced wing topology. The code was validated against several modern commercial transport aircraft, and it showed good agreement with the available data. Chapter 3 describes the MDO methodology and the design code in more detail.

When using the MDO methodology, the designer does not simply set up the problem, let the optimizer find the optimum solution, and then build the first optimum design. MDO is not intended to replace the experience and intuition of a human designer with a computer code. Instead, it should be seen as one of the many design tools in the designer's toolbox. One of the most effective uses of MDO is to perform sensitivity studies by varying one of the key configuration parameters, technologies, or assumptions. Sensitivity studies have traditionally been performed by selecting a baseline or "strawman" design and then varying one parameter at a time to observe the effect on the total system performance. However, this technique does not compare the full potential of each change, since the fixed design cannot adapt to the change.

For example, suppose we wanted to see the effect of airfoil technology on the performance of a design. With the traditional method, the designer would increase the airfoil technology by some increment while keeping the rest of the configuration fixed. The wave drag would go down due to the better drag rise performance of the new airfoil, and the reduction in drag would allow a reduction in the fuel weight required to perform the mission.

Now let us perform the sensitivity study using the MDO methodology. In this case, the designer increases the airfoil technology, but instead of keeping the rest of the configuration parameters fixed, he allows them to become design variables and then he optimizes the configuration for a specified objective. In this case, the wing would tend to unsweep to increase the amount of laminar flow, decrease the structural span, and increase the maximum lift coefficient capability, resulting in a drag reduction. The drag reduction would allow a reduction in fuel weight. The fuel weight would allow a reduction in wing weight, which would then allow a reduction in the rest of the structural weight. All of these effects would continue rippling through all of the aircraft components and all of the design disciplines until the optimum design is found. By using MDO, the design intelligently evolves to take maximum advantage of the increased airfoil technology. Instead of comparing two non-optimal configurations the designer is comparing two optimum configurations that express the full potential of the change in airfoil technology. Several sensitivity studies like the example above are presented in Chapter 4.

In addition to the detailed MDO study of the single-strut configuration, some innovative truss-bracing concepts were conceived in occasional brainstorming sessions. One such design concept, originally proposed by J.A. Schetz [17], is the arch-braced strut. A plastic solid model was created using the *I-DEAS* software, and the Fused Deposition Modeling (FDM) rapid prototyping hardware at Virginia Tech. A subroutine was also written by Mike Libeau [18] to convert the configuration parameters of a given design into a DXF file. This allowed the creation of rendered three-dimensional images, animations, and virtual reality objects using *AutoCAD* on the PC, and *Infini-D* on the Mac. These "imagineering" activities are discussed in Chapter 5.

The conclusions are presented in Chapter 6, and the areas of future work are presented in Chapter 7. The Bibliography contains all of the papers related to the truss-braced wing research organized by subject. The Appendix lists all of the configuration parameters for the four main designs presented in this thesis.

Chapter 2

Problem Statement

The truss-braced wing concept is best suited to a long-range mission, where the increase in efficiency can be fully utilized. A typical mission profile of the Boeing 777-200IGW was selected as the design mission profile for this study. As shown in Figure 2-1, it has a range of 7,380 nmi at Mach 0.85 with 305 passengers in a three-class configuration. An additional 500 nmi of cruise was added to satisfy the reserve fuel requirements. Fixed fuel fractions are used for warm-up, taxi, takeoff, and climb, and the Breguet range equation is used for cruise.
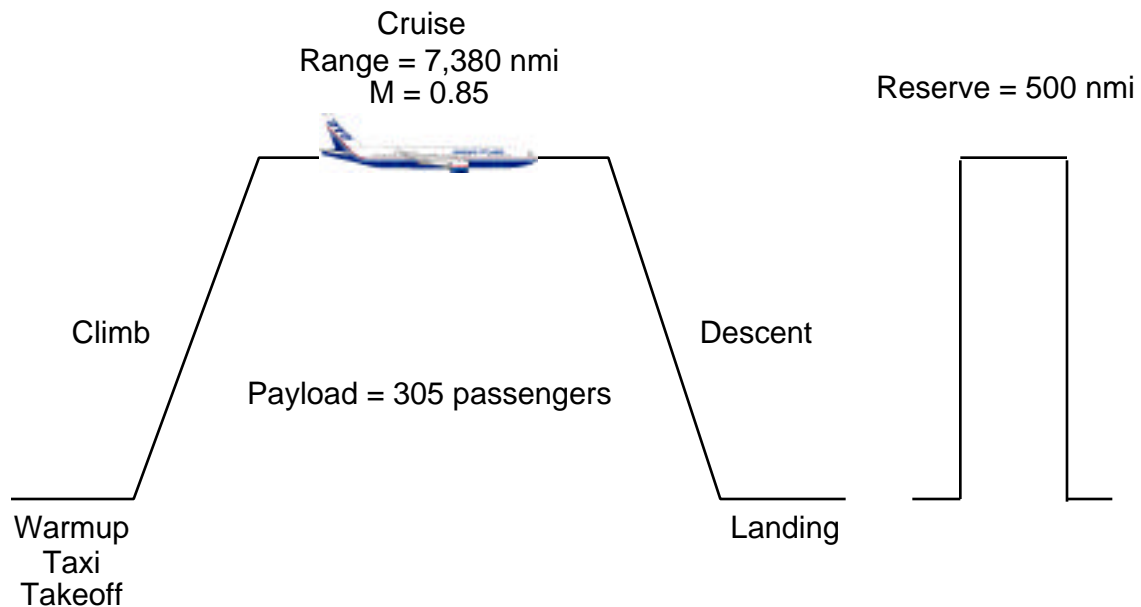
Figure 2-1: Boeing 777-200IGW mission profile

The traditional objective in the design of a large transport is to minimize the takeoff gross weight. This is a good measure of the total system cost, since the acquisition cost and indirect operating cost are strongly driven by the empty weight, and the direct operating cost is strongly driven by the fuel weight. Jensen, Rettie, and Barber [19] performed a study in which they created optimum designs for several figures of merit such as takeoff gross weight, life cycle cost, acquisition cost, direct operating cost, and fuel cost. They concluded that the configurations optimized for minimum takeoff gross weight had the smallest penalty with respect to the off-design figures of merit. Thus, takeoff gross weight is adopted as the primary objective function in this work. The sensitivity study in Section 4.18 compares the effects of optimizing the configuration for different objective functions.

Chapter 3

Methodology

The first step in the truss-braced wing study was to design and implement a multidisciplinary design optimization architecture capable of evaluating both cantilever and truss-braced configurations. The following sections describe the setup of the optimization problem, the top-level MDO architecture, and the details of the major analysis modules in the code.

3.1.   *Definition of the Optimization Problem*

The objective of the truss-braced wing optimization problem is to minimize the takeoff gross weight of the configuration, subject to realistic constraints. The Design Optimization Tools (DOT) software from Vanderplatts [20] is used to perform the optimizations with the method of feasible directions.

3.1.1. Design Variables

The single-strut-braced configuration is parameterized with the 18 design variables shown in Table 3-1. This includes 12 wing shape variables, such as span, sweep, t/c distribution, chord distribution, and the spanwise position of the wing-strut intersection. These are shown graphically in Figure 3-1. The vertical separation of the wing and strut at the root is specified to be equal to the fuselage diameter. The fuselage of the Boeing 777 is used for all of the configurations, and the size remains constant. The other 6 design variables are the zero-fuel weight, fuel weight, cruise altitude, optimum strut force, the increase in the vertical tail lift

coefficient due to circulation control, and the spanwise position of the engine. The fuselage and tail geometry of the Boeing 777-200IGW is used in all of the designs, and it remains fixed throughout the optimization.

Table 3-1: Design variables

Number	Description
1	Spanwise position of wing-strut intersection
2	Semispan
3	Wing sweep
4	Strut sweep
5	Wing root chord
6	Wing chord at wing-strut intersection
7	Wing tip chord
8	Strut root chord
9	Strut tip chord
10	Wing inboard average t/c
11	Wing outboard average t/c
12	Strut t/c
13	Strut force
14	Vertical tail lift coefficient increment due to circulation control
15	Zero-fuel weight
16	Fuel weight
17	Spanwise position of engine
18	Average cruise altitude
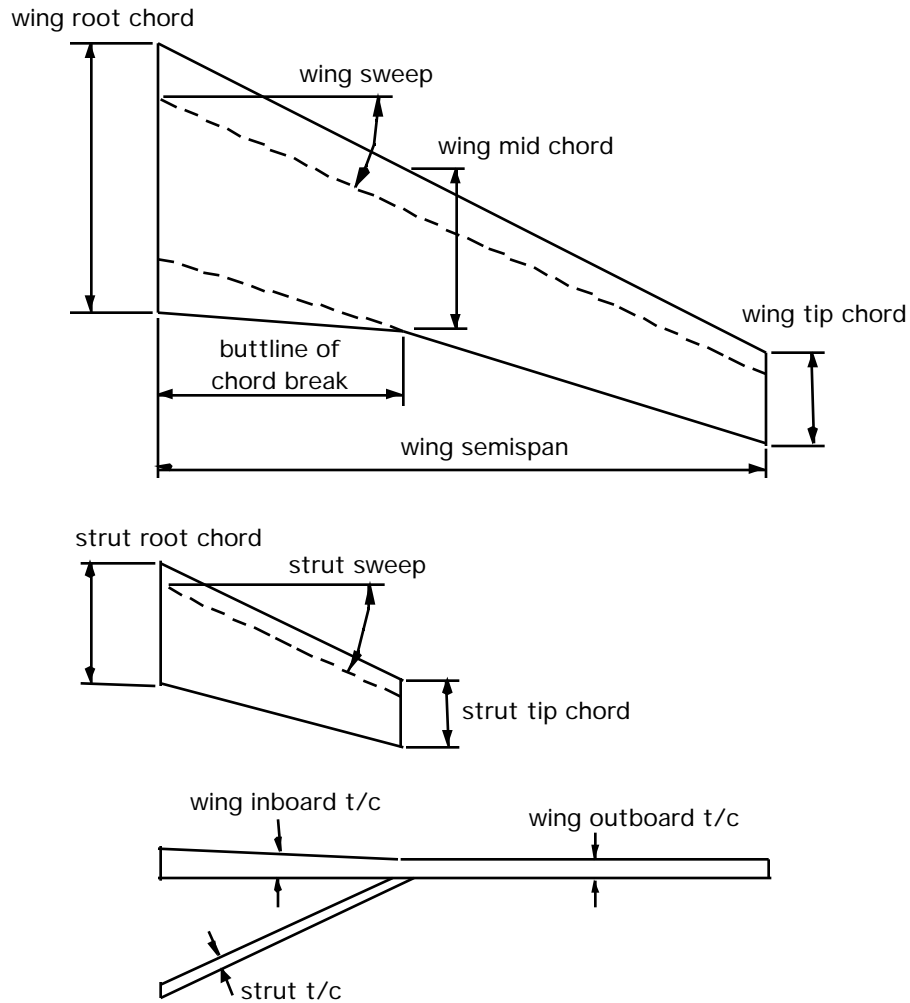
Figure 3-1: Wing geometry

3.1.2. Constraints

Seven inequality constraints are used in the optimization to obtain realistic configurations, as shown in Table 3-2. The weight equations from NASA Langley's Flight Optimization System (FLOPS) are used to calculate most of the structural weight and all of the non-structural weight of the aircraft [21]. When using empirical weight equations, many of the aircraft structural components are sized based on an assumed takeoff gross weight. Therefore, the calculated zero-fuel weight is a function of the initially assumed zero-fuel weight plus the fuel weight. In a traditional aircraft design methodology, an internal iteration loop is used to guarantee that the calculated zero-fuel weight is equal to the assumed zero-fuel weight. However, when an optimizer is already part of the code, it is more efficient to cast the zero-fuel weight and fuel

weight as design variables and use a constraint to enforce convergence [12]. This is the role of the first constraint.

The second constraint ensures that the calculated aircraft range is greater than the range requirement specified in the design mission profile. An additional 500 nmi is added for reserve fuel requirements.

The third constraint ensures that the maximum aircraft lift coefficient is large enough to maintain equilibrium flight at the approach speed and the maximum landing weight. The approach speed is currently assumed to be 140 kts., which is the approach speed of the Boeing 777. The approach speed is an input value to the design code, so it can be easily changed by the user. The maximum landing weight is a user-specified fraction of the takeoff gross weight. In this work, the maximum landing weight is 80% of the takeoff gross weight. The maximum lift coefficient of the unswept wing is assumed to be 3.3.[*] The maximum lift coefficient of the swept wing is then calculated assuming a loss proportional to the cosine of the quarter-chord sweep angle.

The fourth constraint limits the maximum section lift coefficient at the initial cruise flight condition to be less 0.70[**]. This prevents shock stall at high speeds.

The fifth constraint ensures that the fuel tanks have adequate capacity to carry the fuel required to fly the mission. The code has the capability to place extra fuel tanks in the fuselage outside of the wing carry-through structure, but the optimum designs shown in this report do not require additional fuel capacity since the fuel volume constraint is satisfied with some margin for these designs.

The engine-out constraint guarantees that the control system can achieve a sufficient yawing moment to maintain equilibrium flight after an engine failure at the minimum control speed as defined by FAR 25.149.

The wingtip deflection constraint ensures that the wingtip or tip-mounted engine does not strike the ground during a taxi bump load. The current maximum allowable deflection of the wingtip itself is 25 ft., based on the fuselage height and landing gear length of the Boeing 777. This includes a 5 ft. margin for a tip-mounted engine.

---

[*] The value of 3.3 was chosen based on the assumption that the maximum lift coefficient of the swept wing of the Boeing 777 is 2.8, and the maximum lift coefficient is proportional to the cosine of the quarter-chord sweep angle. Since the 777 has a quarter-chord sweep of 31.6°, the following relationship is used: $3.3 \cos(31.6°) = 2.8$.

[**] This value was also chosen based on the Boeing 777. The maximum section lift coefficient on the clean wing of the 777 at the takeoff weight, cruise altitude, and cruise Mach number is 0.70. The value of 0.70 was determined by performing an analysis of the 777 with the truss-braced wing design code.

In addition to the inequality constraints mentioned above, side constraints are used to bound each design variable. Table 3-3 lists the two most important side constraints. The upper side constraint on the semispan design variable guarantees that the wing span is within the FAA 80 meter gate box limit. The lower side constraints on the wing and strut t/c design variables limit the minimum allowable wing and strut t/c values to 5%. The minimum t/c constraint has initially been arbitrarily specified, but it may be refined in the future when a more detailed systems analysis is performed.

Table 3-2: Inequality constraints

Number	Description
1	Zero-fuel weight convergence
2	Range
3	Maximum aircraft lift coefficient at approach speed
4	Maximum allowable section lift coefficient at the beginning of cruise
5	Fuel volume
6	Engine-out
7	Wingtip deflection at the taxi bump load condition

Table 3-3: Side constraints

Number	Description
1	80 meter gate box limit on the wing span
2	Minimum allowable t/c of 5% on the wing and strut

3.2. *Multidisciplinary Approach*

Since the aerodynamics, structures, propulsion, and controls in the truss-braced wing problem are tightly coupled, it is essential to use a multidisciplinary approach to assess the true potential of the configuration. Figure 3-2 shows the connectivity for the truss-braced wing design code architecture. This MDO tool integrates several analysis modules for aerodynamics, structures, and performance. The modular architecture allows for easy integration of higher-fidelity analysis modules, and it provides the capability to evaluate more complex truss topologies in the future.

A brief overview of each analysis module is given below. The complete documentation for the truss-braced wing design code can be found in Ref. [22].
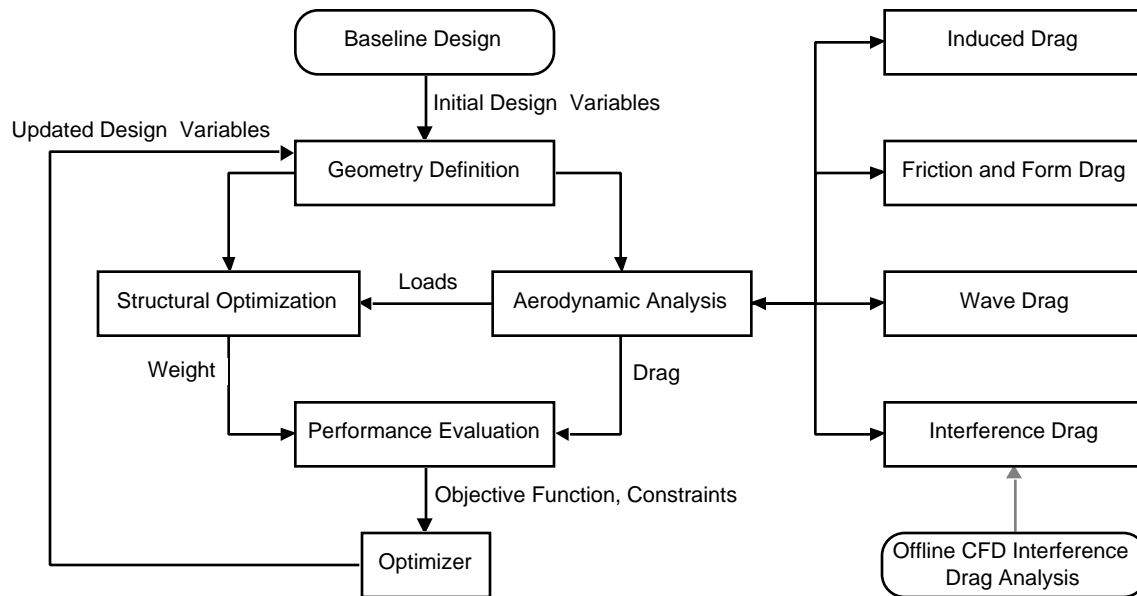
Figure 3-2: MDO code architecture

3.3.   Aerodynamics

The aerodynamic performance is evaluated by modules for the induced drag, parasite drag, transonic wave drag, and interference drag. The stability and control derivatives are also estimated using a DATCOM-based method [23].

3.3.1. Induced Drag

The induced drag module uses a discrete vortex method to calculate the induced drag in the Trefftz plane [24]. Given an arbitrary, non-coplanar wing/truss configuration, it provides the optimum load distribution corresponding to the minimum induced drag.[*] Although the pitching moment about a specified center of gravity location can be specified, we did not impose this constraint on the designs presented in this work (see Section 4.14).

Several studies have shown that the induced drag can be reduced by using tip-mounted engines [14] and [15]. Figure 3-3 shows the induced drag reduction as a function of the lift coefficient and aspect ratio. This relationship was derived from a plot of percent total drag reduction given by Miranda and Brennan [15]. The MDO code uses a simple model based on Figure 3-3 to approximate the induced drag reduction due to tip-mounted engines. Notice that the aerodynamic advantage of tip-mounted engines gets smaller with increasing aspect ratio.

---

[*] For our near-planar designs almost all of the load is carried by the wing.
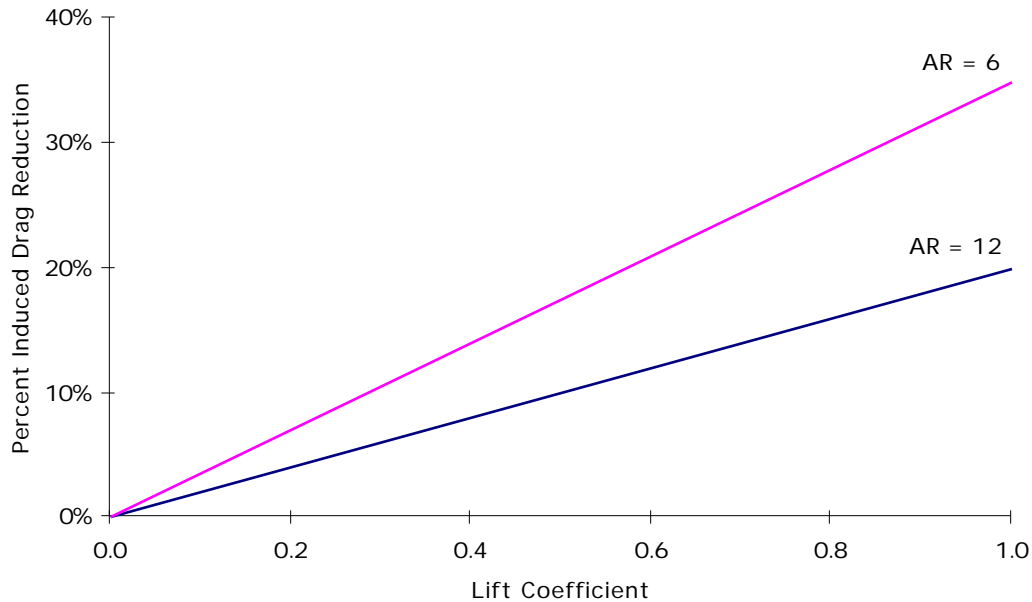
Figure 3-3: Drag reduction due to tip-mounted engines [15]

3.3.2. Parasite Drag

To calculate the parasite drag, the amount of laminar flow is estimated using the transition Reynolds number vs. sweep data from Braslow and Collier [25]. The data for the F-14 and 757 glove experiments is shown in Figure 3-4. A laminar flow technology factor was added to the code to allow modification of the transition Reynolds number assumption. A value between zero and unity is specified, where zero corresponds to the 757 glove experiment and unity corresponds to the F-14 glove experiment.

After determining the transition location, the skin friction is found using the Eckert Reference Temperature method for laminar flow and the Van Driest II formula for turbulent flow. The combined skin friction of the laminar and turbulent portions of the flow is then calculated using Schlicting's composite skin friction formula. The effects of thickness are included by calculating form factors for wings and bodies. This methodology has been implemented in the FRICTION algorithm [26].
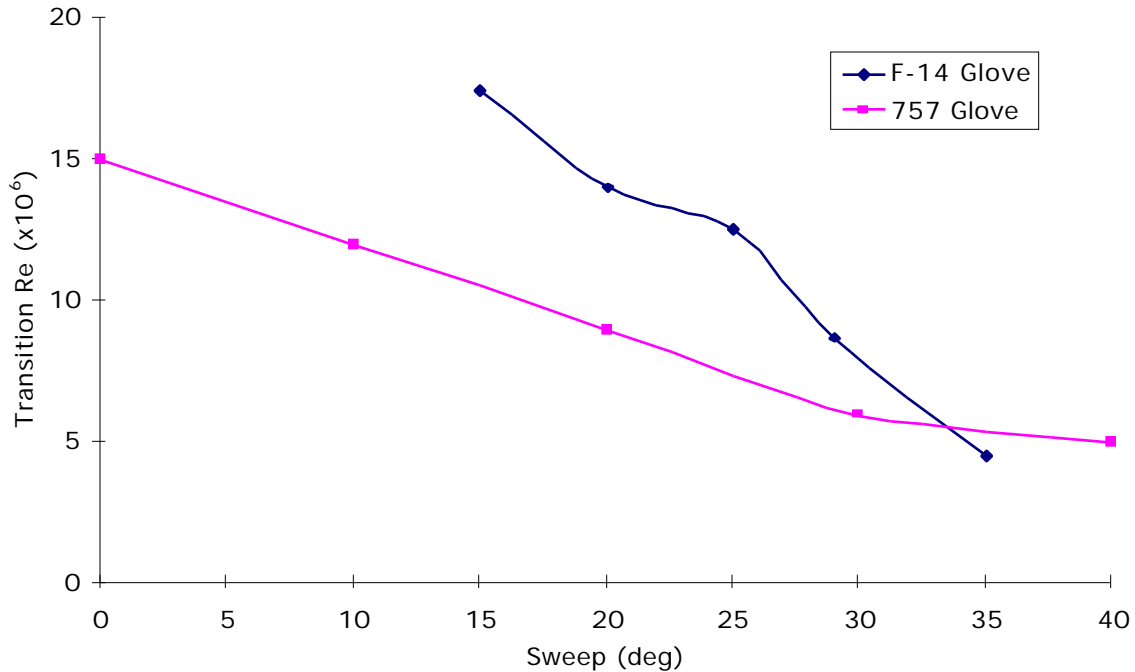
Figure 3-4: Transition Reynolds number vs. sweep [25]

3.3.3. Wave Drag

The wave drag is approximated with the Korn equation, extended to include sweep using simple sweep theory [27] and [28]. This model estimates the drag divergence Mach number as a function of an airfoil technology factor ($_a$), the thickness-to-chord ratio (t/c), the lift coefficient (c_l), and the sweep angle ( ):

$$M_{dd} = \frac{_a}{\cos } - \frac{(t/c)}{\cos^2 } - \frac{c_l}{10\cos^3 } . \tag{3-1}$$

The airfoil technology factor has a value of 0.87 for a NACA 6-series airfoil section, and a value of 0.95 for a supercritical section.

With this approximation for the drag divergence Mach number, we can now calculate the critical Mach number. The definition of the drag divergence Mach number is taken to be:

$$\frac{C_D}{M} = 0.1 . \tag{3-2}$$

Lock proposed the following empirically-derived shape of the drag rise [29]:

$$C_D = 20\,(M - M_{crit})^4. \tag{3-3}$$

15

The definition of the drag divergence Mach number is equated with the derivative of the drag rise formula given above to produce the following equation:

$$-\frac{C_D}{M} = 0.1 = 80 \left(M - M_{crit}\right)^3 .$$

(3-4)

Equation 3-4 can then be solved for the critical Mach number as:

$$M_{crit} = M_{dd} - \left(\frac{0.1}{80}\right)^{1/3} .$$

(3-5)

Finally, the wave drag coefficient is calculated as:

$$c_{d_{wave}} = 20 \left(M - M_{crit}\right)^4 \frac{S_{strip}}{S_{ref}} \qquad for \ M > M_{crit,}$$

(3-6)

The local t/c, c_l, and half-chord sweep angle are specified for a number of spanwise strips along the wing and strut, and the drag of each strip is combined to form the total wave drag. In the equation above, the wave drag for each strip is multiplied by the ratio of the strip area (S_{strip}) to the reference area (S_{ref}). The number of spanwise strips can be input by the user. The designs presented in this work were created using eight spanwise strips.

This method has been validated with the Boeing 747-100, as shown in Figure 3-5. The solid lines represent the current model predictions, and the discrete data points represent the Boeing 747 flight test data [30]. The predictions show good agreement with the data over a wide range of Mach numbers and lift coefficients. The results are sensitive to the value of the airfoil technology factor. A value of 0.89 was used for the Boeing 747 results in Figure 3-5. Based on an analysis of the Boeing 777, a value of 0.955 was used for the cantilever and strut-braced configurations presented here.
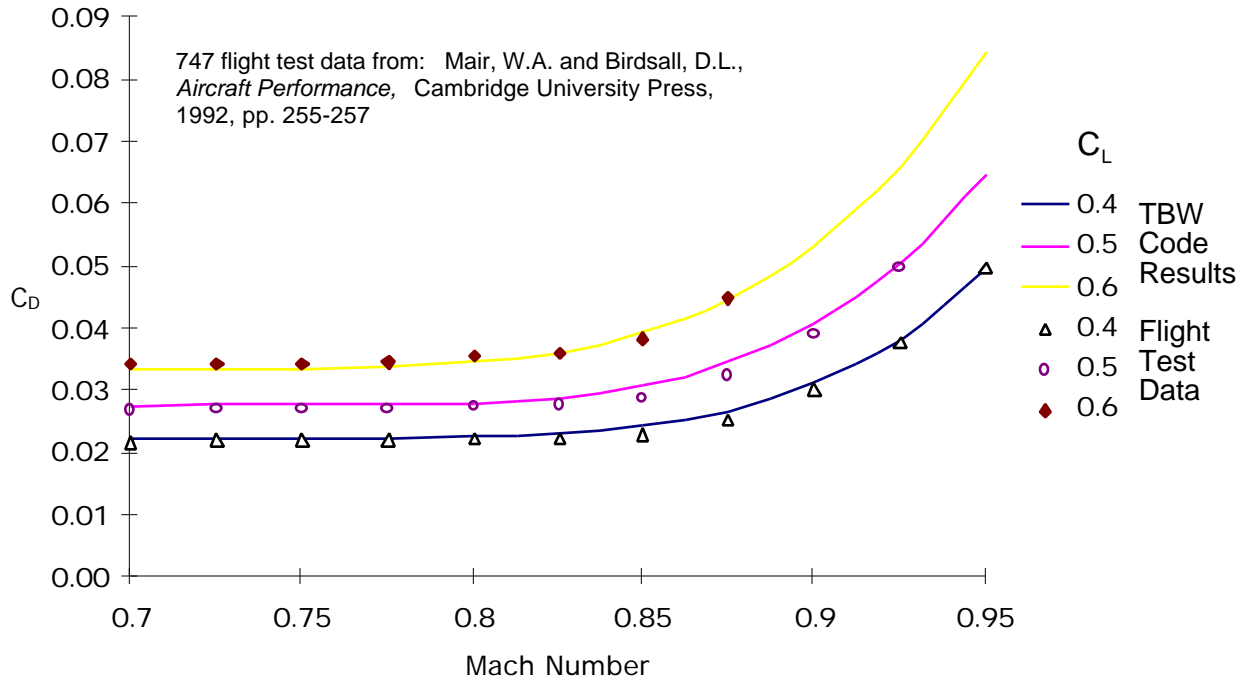
Figure 3-5: Boeing 747-100 drag rise comparison

3.3.4. Interference Drag

The interference drag is currently estimated using the equations and wind tunnel data given by Hoerner in Chapter 8 of *Fluid-Dynamic Drag* [31]. Since the wind tunnel experiments were performed at low Mach numbers, the extrapolation of this data to transonic Mach numbers is not expected to provide an accurate measure of the interference drag, but simply an indication of the trends. However, no relevant transonic interference drag data was found. A sensitivity study with respect to the magnitude of the wing-strut interference drag is shown in Section 4.8.

Five fundamental interference drag effects were identified from the Hoerner data. These five effects are combined in different ways to calculate the interference drag for a wing-fuselage intersection, and a wing-strut intersection.

The first effect is the interference drag due to a wing intersecting a flat wall at a perpendicular angle (90°). The drag coefficient due to this effect is given by:

$$c_{d_{wall}} = \left(0.8\,(t/c)^3 - 0.0003\right) \frac{c^2}{S_{ref}}. \tag{3-7}$$

17

The second effect is the interference drag due to a streamlined section intersecting another streamlined section at a perpendicular angle (90°). This is equivalent to a perpendicular wing-strut intersection. The drag coefficient due to this effect is given by:

$$c_{d_{strut}} = \left(17 \, (t/c)^4 - 0.05 \, (t/c)^2\right) \frac{c^2}{S_{ref}} \cdot \quad (3\text{-}8)$$

The t/c and c in this equation are taken here to be the average values of the wing and strut.

The third effect is the interference drag due to the lift coefficient. The drag coefficient due to this effect is given by:

$$c_{d_{cl}} = \left(0.1 \, c_l^2\right) \frac{c^2}{S_{ref}} \cdot \quad (3\text{-}9)$$

This equation comes from the statement, "At any rate, the interference drag approximately increases as the square of the lift coefficient." [31, p. 8-11]. The coefficient preceding the c_l^2 term is the slope of the $c_{d_{cl}}$ vs. c_l curve. The value of 0.1 corresponds to the slope of the experimental curve given by Hoerner.

The fourth effect is the interference drag reduction due the sweep of the intersection. The drag coefficient due to this effect is given by:

$$c_{d_{sweep}} = \left(-0.000018 \quad ^2 + 0.00009 \quad \right) \frac{c^2}{S_{ref}} \quad (3\text{-}10)$$

The sweepback angle ( ) is defined as 0° for a perpendicular intersection in the side view. This equation is a curve fit to the data given on p. 8-11 of Hoerner [31]. Figure 3-6 shows the original data along with the curve fit. For this plot, $c^2 = S_{ref}$.
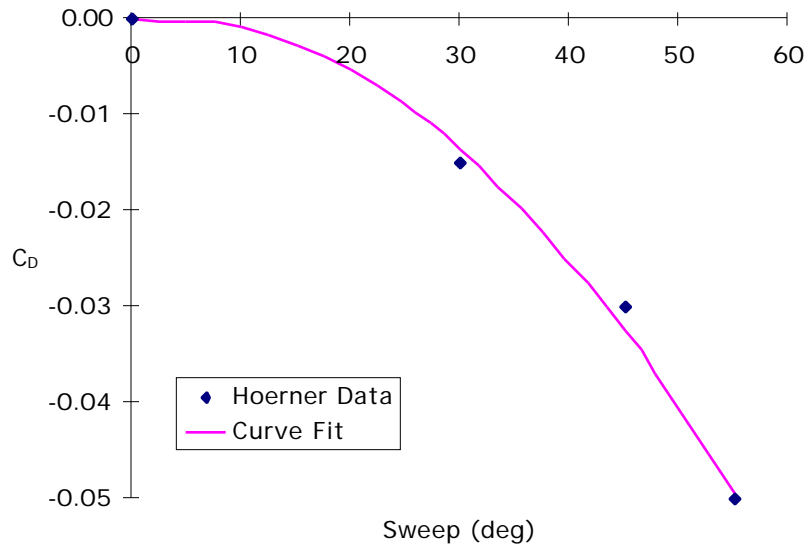
Figure 3-6: Sweep effect on interference drag coefficient

The fifth effect is the interference drag due the inclination angle of the intersection. The drag coefficient due to this effect is given by:

$$c_{d_{inclin}} = \left(0.000006\ \lambda^2 + 0.0015\ \lambda \right) \frac{c^2}{S_{ref}} \tag{3-11}$$

The inclination angle (λ) is defined as 0° for a perpendicular intersection in the front view. This equation is a curve fit to the data given on p. 8-11 of Hoerner [31]. Figure 3-7 shows the original data along with the curve fit. For this plot, $c^2 = S_{ref}$.
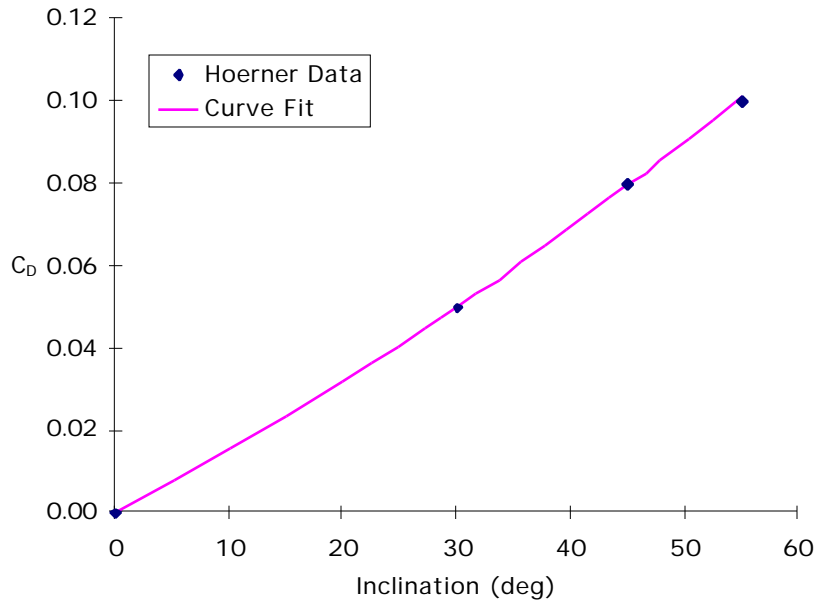
Figure 3-7: Inclination effect on interference drag coefficient

The five effects shown above are combined in the following ways to form the total interference drag for the wing-fuselage and wing-strut intersections.

Wing-fuselage: $$c_{d_{int\,wing\text{-}fuse}} = c_{d_{wall}} + c_{d_{cl}} + c_{d_{sweep}} + c_{d_{inclination}}$$ (3-12)

Wing-strut: $$c_{d_{int\,strut}} = c_{d_{strut}} + c_{d_{cl}} + c_{d_{sweep}} + c_{d_{inclination}}$$ (3-13)

All of the interference drag equations above assume that no fillets are being used at the intersections of the surfaces. On p. 8-12, Hoerner states: "the interference drag of a strut junction can thus be reduced to 10% of the unfaired configuration or less by means of a fairing extending one strut chord beyond the trailing edges." Therefore, the interference drag calculated above is reduced by a factor of 10 in our work.

Since the interference drag methodology is approximate and based on low-speed data, a sensitivity study with respect to the magnitude of the wing-strut interference drag was performed. This study is shown in Section 4.8. In the future, we plan to incorporate the results of off-line CFD analyses of wing-strut intersections at transonic speeds to refine these predictions.

3.4.   Propulsion

A simple "rubber engine" sizing methodology is used to scale the weight and size of the baseline engines to match the required thrust. The rubber engine weight is assumed to be linearly proportional to the thrust required at the initial cruise condition.

$$W_{engine_{calc}} = \frac{T_{req}}{\left(\dfrac{T_{baseline}}{W_{engine}}\right)} \tag{3-14}$$

The thrust requirement is determined by matching the required thrust at the initial cruise flight condition with the drag at that condition. On page 80 of Raymer [32], he states that thrust matching at cruise is an acceptable way to obtain the required thrust for an aircraft designed primarily for cruise efficiency. Therefore, we first calculate the drag at cruise as:

$$D_{cruise} = C_{D_{cruise}} q_{cruise} S_{ref} \tag{3-15}$$

The required thrust per engine at cruise is calculated by dividing the total aircraft drag by the total number of engines:

$$T_{cruise} = \frac{D_{cruise}}{n_{engines_{wing}} + n_{engines_{fuse}}} \tag{3-16}$$

The final step is to account for the loss of thrust due to altitude and Mach number. This is known as the thrust lapse relationship. The functional form of the thrust lapse is taken from equation 2.42 on p. 36 of *Aircraft Engine Design* [33]. The coefficients in the equation were adjusted using a nonlinear regression analysis with a GE-90-like engine deck provided by NASA Langley. The following equation contains the adjusted coefficients:

$$T_{req} = \frac{T_{cruise}}{\left[0.4307 + 0.3578(1.2265 - M)^{2.3137}\right]^{0.7365}} \tag{3-17}$$

In addition to a weight savings, a decrease in the amount of required thrust would also correspond to a drag savings due to the smaller engine size. The length and diameter of the engine are scaled proportional to the square root of the ratio of the required thrust to the baseline thrust:

$$l_{actual} = l_{baseline} \sqrt{\frac{T_{req}}{T_{baseline}}} \tag{3-18}$$

$$d_{actual} = d_{baseline} \sqrt{\frac{T_{req}}{T_{baseline}}} \qquad (3\text{-}19)$$

To estimate the drag savings, the nacelle drag is multiplied by the ratio of the required thrust to the baseline engine thrust. This is equivalent to scaling the diameter and the length of the nacelle by square root of the thrust ratio, since the friction drag is proportional to the wetted area.

When this rubber engine sizing methodology is applied to the baseline cantilever aircraft, the required sea-level static thrust is 87,824 lb., which results in an engine weight of 22,407 lb. The engine thrust and weight predicted from the NASA engine deck are 90,764 lb. and 23,157 lb., respectively. Therefore, for this case, the rubber engine sizing methodology underpredicts the engine weight by 3%.

The engine deck provided by NASA was also used to create the following relation for the specific fuel consumption as a function of altitude and Mach number. A nonlinear regression analysis was used to adjust the coefficients in the functional form presented by Mattingly, et al. [33]. The following equation contains the adjusted coefficients.

$$sfc_{\ cruise} = \left(\frac{Temp_{cruise}}{Temp_{sl}}\right)^{0.4704} (sfc_{s,sl} + 0.4021 M) \qquad (3\text{-}20)$$

3.5.   Fuel Capacity and Distribution

The fuel capacity subroutine calculates the fuel capacity of the wing, strut, and fuselage tanks, and the weight distribution of the fuel along the span. Several assumptions must be made when calculating the fuel capacity. Figure 3-8 shows a cross-section of the wing, including the fuel tank. According to Raymer [32], p. 228, the ratio of the volume of an integral wing tank to the externally measured volume is 0.85. This is a fixed assumption in the present code, since integral fuel tanks are used on large commercial transports. The relative chord of the fuel tank can be specified by the user with an input parameter that specifies the percent chord (x/c) of the tank. The initial truss-braced wing studies have assumed that the fuel tank occupies 50% of the chord. The fuel tank is assumed to be between the front and rear spars, which are typically at the 15% and 65% chord positions. The fuel density is also an input parameter. Large transports typically use Jet-A fuel, which has a nominal density of 6.8 lb./gallon [34].
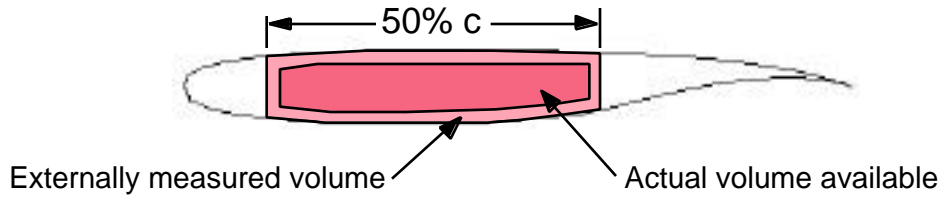
Figure 3-8: Cross-section of wing and fuel tank

Fuel can be stored in five different fuel tanks, as shown in Figure 3-9. The fuel capacity can be increased by adjusting the capacity of the fuselage fuel tanks with an input parameter. The fuselage fuel tanks do not include the fuel capacity of the wing carry-through tank, which is calculated separately. The outer portion of the outboard wing tank does not contain any fuel. In the initial truss-braced wing studies, the fuel tank extends to 78% span, which is the outer limit for the Boeing 777.
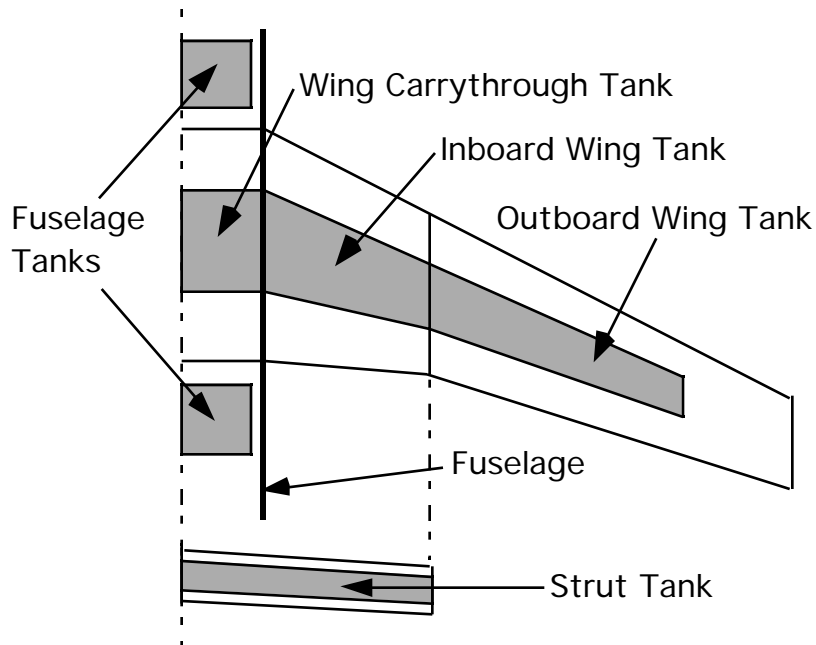
Figure 3-9: Fuel tank arrangement

The wing tanks are divided into a number of spanwise strips to calculate the fuel weight distribution. If the fuel does not occupy the entire tank volume, fuel can be shifted inboard or outboard to provide inertia relief for the wing structure, resulting in a lower wing weight.

The method above predicts that the fuel capacity of a Boeing 777-200IGW is 314,864 lb. The actual fuel capacity is 307,496 lb., resulting in a 2% error. NASA Langley's Flight Optimization System (FLOPS) also has an equation for calculating the fuel volume [21]. However, the FLOPS

fuel volume equation is based on the average wing *t/c* and the taper ratio of the trapezoidal wing. Therefore, the FLOPS method is less accurate than the integration method described above. The method described above is also capable of placing fuel in the strut, while the FLOPS fuel volume equation assumes a cantilever wing.

3.6.   Weight Estimation

A flowchart of the weight estimation methodology is shown in Figure 3-10. The weight estimation routines from NASA Langley's Flight Optimization System (FLOPS) are used to estimate the aircraft weight [21]. Since FLOPS only uses a correction factor to estimate the bending material weight of a strut-braced wing, a more detailed method was developed and implemented by Amir Naghshineh-Pour in a new subroutine [35]. The bending material weight subroutine uses a piecewise linear beam model to calculate the wing bending material weight based on the configuration parameters and load distributions at the critical load cases (discussed below). This value is then substituted for the FLOPS bending material weight in the FLOPS weight equations. Replacing the bending material weight from FLOPS with other estimates has been done in High Speed Civil Transport research at Virginia Tech for several years [36]. In the future, a bending material weight response surface could be created from several offline finite element method (FEM) optimizations [37] and [38]. This response surface could then be substituted for the bending material weight subroutine.
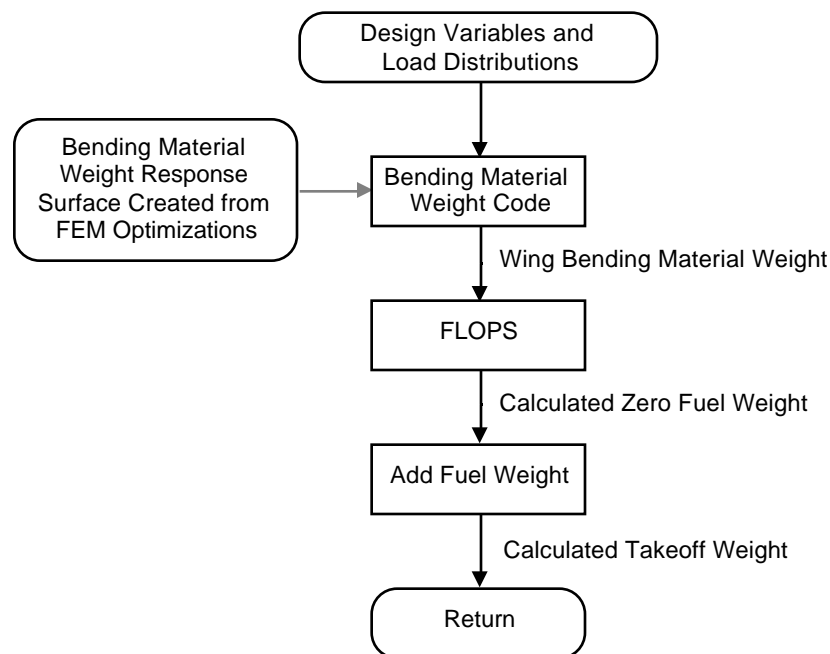
Figure 3-10: Flowchart of weight subroutine

Two maneuver load conditions (2.5 *g* and -1.0 *g*), and a 1.67 *g* taxi bump load condition are used to estimate the wing bending material weight. Coster and Haftka [39] showed that for a truss-braced wing subjected to negative *g* maneuvers, a significant weight penalty is required to prevent the strut from buckling. They evaluated the effects of buckling on both single-strut-braced wing configurations and truss-braced wing configurations. The results revealed that using a truss would reduce the weight penalty due to buckling by approximately 50% relative to a single strut. However, the weight penalty was still significant. Hence, to eliminate the weight penalty due to strut buckling a different design philosophy was proposed by Dr. Haftka [40]. The strut is assumed to be inactive in compression during the -1.0 *g* maneuver load case and the 1.67 *g* taxi bump case. This could be done with a telescoping sleeve mechanism or a hinge arrangement. During positive *g* maneuvers, the strut is in tension. Since the wing is clamped to the fuselage, it acts as a cantilever beam in the negative load cases and as a strut-braced beam in the positive load cases. Moreover, the strut force at the 2.5 *g* load case is optimized to minimize the wing bending material weight. On a typical optimum single-strut design, this means that the strut would become fully engaged at around 0.75 *g*. At loads between 0 *g* and 0.75 *g*, a spring would be used to gradually increase the strut force up to the strut engagement point (see Figure 3-11). The optimum strut force at 2.5 *g* is less than the 2.5 *g* strut force that would be obtained if the strut was built as a rigid member and engaged immediately at 0 *g* (this could be thought of as the pre-force or jig-shape force). This design approach results in a significant reduction in the bending material weight compared to a wing in which a completely rigid strut is designed to withstand the buckling loads.
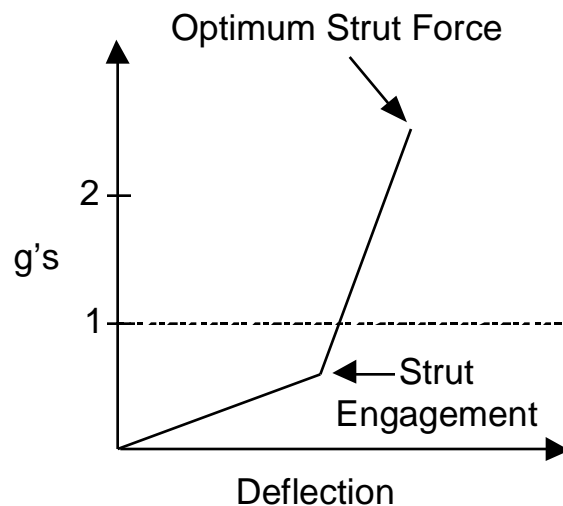
Figure 3-11: Illustration of bilinear strut stiffness

3.7. Stability and Control

The use of tip-mounted engines demands careful attention to the engine-out analysis. The failure of a tip engine requires the airframe to produce a large yawing moment to maintain equilibrium flight at the engine-out flight condition.

The engine-out constraint is established by constraining the maximum available yawing moment coefficient ($C_{n_{avail}}$) to be greater than the required yawing moment coefficient ($C_{n_{req}}$) for the engine-out flight condition:

$$C_{n_{avail}} \quad C_{n_{req}} \qquad (3\text{-}21)$$

The required yawing moment coefficient is the yawing moment coefficient required to maintain steady flight with one failed outboard engine at 1.2 times the stall speed, as specified by FAR 25.149. The remaining outboard engine must be at the maximum available thrust, and the bank angle cannot be larger than 5°.

Figure 3-12 shows the engine-out geometry for a twin-engine configuration. The yawing moment coefficient required to maintain steady flight with an inoperative engine is given by:

$$C_{n_{req}} = \frac{(T_{eo} + D_{ewm})l_e}{qS_{ref}b} \qquad (3\text{-}22)$$

where T is the maximum available thrust at the given Mach number and altitude, and D_{ewm} is the drag due to the windmilling of the failed engine. The lateral force of the vertical tail (F_v) provides most of the yawing moment required to maintain steady flight after an engine failure.
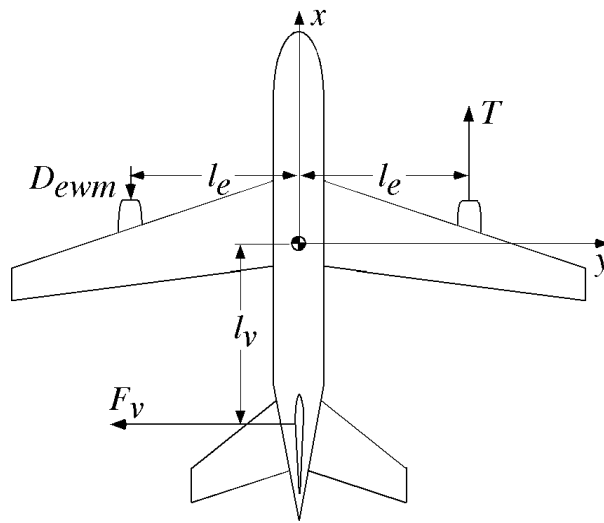
Figure 3-12: Engine-out geometry

The maximum available yawing moment coefficient is obtained at an equilibrium flight condition with a given bank angle ( ) and a given maximum rudder deflection ($_r$). The bank angle is limited to a maximum of 5° by FAR 25.149, and the aircraft is allowed to have some sideslip ( ). The stability and control derivatives are calculated using the empirical method of Ref. [41] (which is essentially DATCOM [23]). The available yawing moment is then calculated using a combination of rudder deflection, thrust vectoring, and circulation control.

The sideslip angle is found by summing the forces along the y-axis:

Sideforce Equation:

$$C_{y_a} a + C_{y_r} r + C_y + C_L sin - \frac{T \sin}{qS_{ref}} - C_{L_{cc}} \frac{S_{vtail}}{S_{ref}} = -\frac{Y_{ext}}{qS_{ref}} \tag{3-23}$$

In a conventional control system, the vertical tail is the dominant controller for generating a yawing moment. However, thrust vectoring and circulation control can be used to generate additional yawing moments. Since the engine-out condition is a critical constraint for a truss-braced wing with tip-mounted engines, the capability to model thrust vectoring and circulation control on the vertical tail was added to the code. The fifth term in the equation above ($\frac{T \sin}{qS_{ref}}$) is due to the thrust being vectored at an angle to the centerline, and the sixth term ($C_{L_{cc}} \frac{S_{vtail}}{S_{ref}}$) is due to the change in C_L at the vertical tail due to circulation control. Since the external sideforce (Y_{ext}) is zero, and C_{y_a} is assumed to be zero, this equation can be simplified and solved for the sideslip angle:

$$= \frac{- C_{y_r} r - C_L sin + \frac{T \sin}{qS_{ref}} + C_{L_{cc}} \frac{S_{vtail}}{S_{ref}}}{C_y} \tag{3-24}$$

The aileron deflection required to maintain equilibrium flight is obtained by summing the rolling moments about the x-axis:

Rolling Moment Equation:

$$C_{l_a} a + C_{l_r} r + C_l - \frac{T \sin}{qS_{ref}} \frac{z_{tv}}{b} - C_{L_{cc}} \frac{S_{vtail}}{S_{ref}} \frac{z_{vtail}}{b} = -\frac{L_{ext}}{qS_{ref}b} \tag{3-25}$$

By setting the external rolling moment (L_{ext}) equal to zero, this equation can be solved for the aileron deflection:

$$\delta_a = \frac{- C_{l_r}\, \delta_r - C_l + \dfrac{T \sin}{q S_{ref}}\,\dfrac{z_{tv}}{b} + C_{L_{cc}}\dfrac{S_{vtail}}{S_{ref}}\dfrac{z_{vtail}}{b}}{C_{l_a}} \tag{3-26}$$

The rudder deflection is initially set to the given maximum allowable steady-state value, and the sideslip angle and aileron deflection for equilibrium flight are determined by Eqs. (3-24) and (3-26). The maximum allowable steady-state deflection is typically 20°-25°. This allows for an additional 5° of deflection for maneuvering. In the computer code, a warning statement is printed if the calculated deflection exceeds the maximum allowable deflection.

The maximum available yawing moment is found by summing the contributions due to the ailerons, rudder, and sideslip:

Yawing Moment Equation:

$$C_{n_{avail}} = C_{n_a}\, \delta_a + C_{n_r}\, \delta_r + C_n + \frac{T \sin}{q S_{ref}}\,\frac{l_{tv}}{b} + C_{L_{cc}}\frac{S_{vtail}}{S_{ref}}\frac{l_{vtail}}{b} \tag{3-27}$$

This value of the available yawing moment coefficient is then constrained in the optimization problem to be greater than the required yawing moment coefficient, as shown in Eq. (3-21). The details of the stability and control derivative estimation and engine-out analysis are given in Reference [42].

The use of circulation control on the vertical tail creates a large sideforce at relatively low sideslip angles. It effectively shifts the lift curve up by an increment in the vertical tail lift coefficient. At this point in the study, the increment in the vertical tail lift coefficient is implemented as a design variable with an upper bound of 1.0. Most tip-mounted engine configurations to date have required a change in the vertical tail lift coefficient of about 0.9. According to the data given by Englar and Williams [16], this is a reasonable value. The current model assumes no weight penalty for the circulation control mechanism.

3.8. Performance

The performance subroutine calculates the range of a given configuration, based on the specific fuel consumption, cruise velocity, lift-to-drag ratio, and weights. The range calculation is performed with the Breguet range equation for a cruise-climb flight profile:

$$range = \frac{V\,(L/D)}{sfc_{cruise}} \, ln\left(\frac{W_{initial}}{W_{zf}}\right) - reserve \tag{3-28}$$

where:

$$W_{initial} = 0.956 \; W_{to} \tag{3-29}$$

The equation above states that 4.4% of the fuel is burned during warm-up, taxi, takeoff, and climb. The reserve range is currently assumed to be 500 nmi.

3.9. Validation

The complete design code was validated with the Boeing 747-100, the Boeing 777-200IGW, and a single-strut-braced military transport from a Boeing design study published in 1978 [43]. Each validation showed good agreement with the available weight, drag, and performance data. Our model of the Boeing 777 also compared favorably to a Boeing 777 model created by Matt Sexstone at NASA Langley [44].

Jane's lists three values for the maximum takeoff gross weight of the Boeing 747-100: 710,000 lb., 735,000 lb., and 750,000 lb. The truss-braced wing code shows good agreement, with a predicted takeoff gross weight of 719,000 lb. The code also shows excellent agreement with respect to the wing weight. The actual wing weight is 88,019 lb. [46], and the truss-braced wing code predicts a wing weight of 88,705 lb. A validation of the drag estimation methodology is shown in Figure 3-5. The code shows good agreement with the flight test data over a range of Mach number and lift coefficient.

Unfortunately, the drag breakdown of the Boeing 747-100 was not available. Therefore, the drag breakdown from a Boeing study of a single-strut-braced wing military transport was used to validate the individual drag components [43]. A three-view of the configuration is shown in Figure 3-13.

29
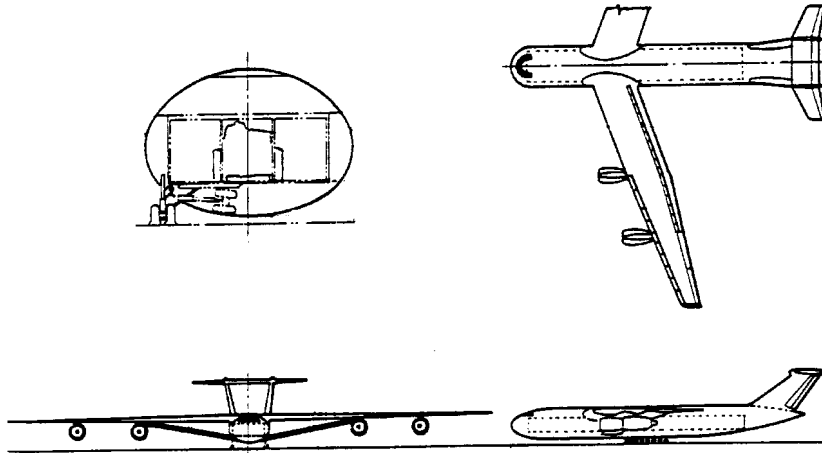
Figure 3-13: Boeing single-strut-braced transport

This configuration was assumed to be completely turbulent. The Boeing study did not list the wing-fuselage interference drag separately. However, when the wing-fuselage interference drag predicted by the truss-braced wing code is combined with the fuselage drag, the sum agrees quite well with the Boeing data, as shown in Figure 3-14. The rest of the drag components also agree reasonably well.
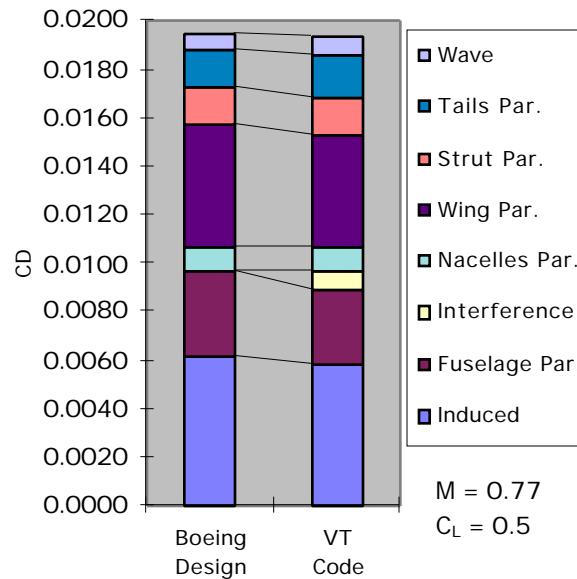
Figure 3-14: Single-strut drag breakdown comparison

Additional validations were performed for the induced drag subroutine and the wing bending material weight subroutine. These validations can be found in Refs. [22] and [35], respectively.

Chapter 4

Results

The goal of this study is to evaluate the feasibility of the truss-braced wing concept and compare the performance with the cantilever wing configuration. For this purpose, we have created two cantilever configurations to make such comparisons.

When performing an MDO study using relatively low-fidelity analysis codes, it is important to validate the codes with a baseline configuration with known performance. For this study, we created a computational model of the Boeing 777-200IGW. The weight and performance predicted by the MDO code were found to be in good agreement with the available data. This design is referred to as the current technology baseline cantilever configuration (Figure 4-1).

In the truss-braced wing MDO studies, we have introduced advanced technology concepts such as natural laminar flow and relaxed static stability to increase performance. We also use a rubber engine sizing method to match the engine size and weight to the required thrust, and several structural components are sized based on the takeoff gross weight. With these assumptions, the optimizer can redesign the baseline configuration to achieve the maximum benefit. It would be wrong to compare a truss-braced wing utilizing these assumptions and design degrees of freedom with a current technology cantilever design. Therefore, an advanced technology optimized cantilever configuration (Figure 4-2) was created by allowing the span, t/c, sweep, and chord distribution to be design variables and minimizing the takeoff gross weight. This configuration allows us to make valid comparisons between the cantilever and truss-braced wing concepts under the same set of technology assumptions with the same design methodology.
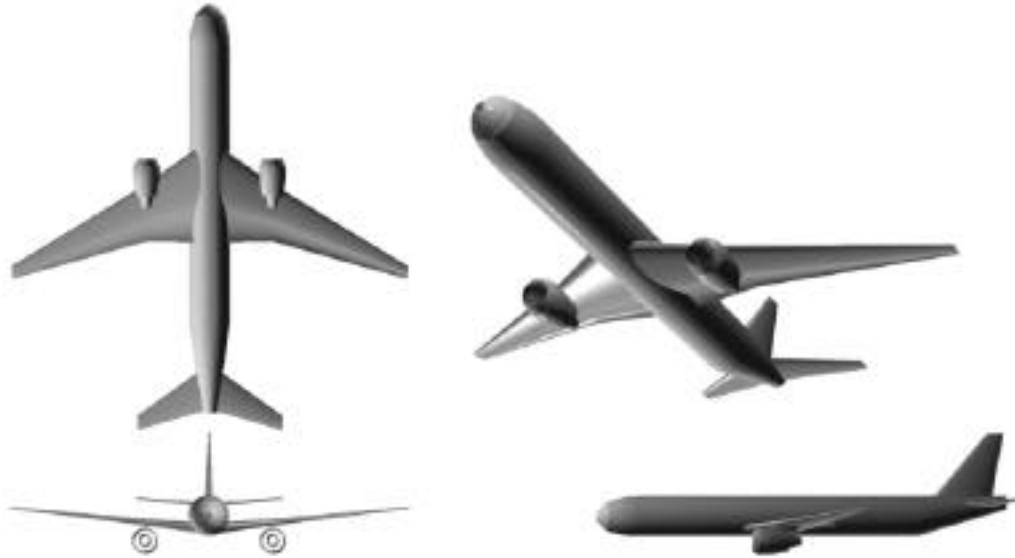
Figure 4-1: Current technology baseline cantilever configuration

Figure 4-2: Advanced technology optimized cantilever configuration

A single-strut-braced high wing configuration is currently used as the most basic representation of the truss-braced wing concept. Two variations on this concept are shown below. The first single-strut configuration was created by fixing the engines at the wingtips and optimizing seventeen design variables for minimum takeoff gross weight (Figure 4-3). The second configuration was created by allowing the spanwise position of the engines to be an additional design variable (Figure 4-4).[*]

---

[*] We assume that the induced drag reduction due to tip-mounted engines is effective only when the engine is located exactly at the tip. If the engines were located at 99% of the span, no induced drag reduction would be calculated. For this reason, two single-strut optimizations were performed: one starting with the engines at the tip, and one starting with the engines partially inboard.

The following two sections will show the drag, weight, and cost comparisons between the four designs. The remaining sections will show the sensitivity of the optimum single-strut design with tip-mounted engines to changes in sweep, the amount of laminar flow, the airfoil technology, the wing-strut interference drag, and the design Mach number.

Figure 4-3: Optimum single-strut configuration with tip-mounted engines

Figure 4-4: Optimum single-strut configuration with under-wing engines[*]

---

[*] Clearly the strut-pylon-nacelle integration details need to be resolved. Opportunities for additional drag reduction may arise when this is done.

4.1. Comparison of Cantilever and Strut-Braced Designs

Table 4-1 shows a configuration summary of the four designs. The complete parameter set is shown in the Appendix. The advanced technology optimized cantilever design shows a slight increase in span from the current technology cantilever configuration. The sweep also increased from 31.6° to 36.7° in order to reduce the wave drag. The cruise *L/D* increased from 18.8 to 21.7, and the takeoff gross weight decreased from 632,081 lb. to 568,031 lb.

Table 4-1: Configuration comparison

	Current Technology Cantilever	Advanced Technology Cantilever	SS with Tip Engines	SS with Under-Wing Engines
Wing Span (ft)	199.9	206.6	198.9	258.7
Wing Area (ft2)	4,607	4,365	3,829	3,259
Aspect Ratio	8.7	9.8	10.3	20.5
Inboard Wing 1/4-Chord Sweep (deg)	31.6	36.7	27.3	24.5
Outboard Wing 1/4-Chord Sweep (deg)	31.6	36.7	27.3	24.5
Strut 1/4-Chord Sweep (deg)	N/A	N/A	17.7	16.3
Wing t/c at the Centerline	15.1%	15.4%	13.3%	11.9%
Wing t/c at the Chord Breakpoint	10.9%	10.5%	5.0%**	5.0%**
Wing t/c at the Tip	10.9%	10.5%	5.0%**	5.0%**
Strut t/c	N/A	N/A	5.0%**	5.0%**
Cruise L/D / Max L/D	18.8 / 20.9	21.7 / 24.0	24.4 / 27.4	27.8 / 31.5
Specific Range (nmi/1000 lb)	26.0	33.5	43.7	50.6
Seat Miles per Gallon (seats*nmi/gal)	60.5	74.7	94.2	105.2
Wing Weight (lb)	77,318	79,420	55,544	68,070
Takeoff Gross Weight (lb)	632,081	568,031	488,990	481,236

** The wing chord breakpoint, tip, and strut *t/c* values have converged to the minimum allowable value of 5%.

The advanced technology cantilever design shows a 10% savings in takeoff gross weight relative to the current technology cantilever configuration. This weight savings is due in large part to the advanced technology assumptions such as partial laminar flow, relaxed static stability, and rubber engine sizing. The slight changes in the configuration shape also contributed to the weight savings.

Using the same technology assumptions and design methodology, the optimum single-strut design with tip-mounted engines achieves a weight savings of 23% relative to the current

technology cantilever configuration (14% relative to the advanced technology optimum cantilever configuration). The wing weight is only 55,544 lb., even though the span is about the same as the current technology cantilever configuration. The sub-200 ft. span would allow this strut-braced design to operate in the same gates as the Boeing 747 and 777. The structural efficiency of the strut allows the t/c to be reduced to 13.3% at the root, and 5.0% outboard of the chord breakpoint (5% was chosen for the initial studies as the minimum allowable t/c). The reduction in thickness allows the wing to unsweep to 27.3°, and the strut has 17.7° of sweep. The result is an L/D of 24.4 and a takeoff gross weight of 488,990 lb. This is a 79,000 lb. reduction from the advanced technology cantilever design, and a 143,000 lb. reduction from the current technology cantilever design.

The span of the single-strut design with tip-mounted engines was limited by the wingtip deflection constraint during the taxi bump load case. A further increase in span would have caused the engines to strike the ground during the worst case taxi bump. Therefore, a second single-strut design was created with the spanwise position of the engine as an additional design variable. By moving the engine slightly inboard, the optimizer could increase the span to 258.7 ft., decrease the root t/c to 11.9%, and decrease the sweep to 24.5°. These configuration changes resulted in a cruise L/D of 27.8. The lower drag required less thrust, resulting in an 800 lb. weight savings on each engine, which further alleviated the tip strike constraint. The wing weight for this design increased to 68,070 lb., but the large fuel savings allowed the takeoff gross weight to decrease by about 7,000 lb. from the previous single-strut design. The FAA 80 meter gate box limit is equivalent to a wingspan of 262.5 ft. Therefore, this design is barely within the maximum allowable gate box, which may present operational limitations on the design.

Note that the two single-strut configurations exploited two different modes for obtaining their low weight. The tip-mounted engine design used the drag reduction available from mounting the engines at the tip to reduce the wing span and hence the wing weight. In contrast, the under-wing engine design obtained a lower fuel weight by significantly increasing the L/D. The induced drag was reduced by increasing the span, at the expense of a heavier wing. Increased laminar flow due to smaller chords and lower sweep also contribute to the low drag of this design. The resulting takeoff gross weights were very similar, with the under-wing engine configuration producing a slightly lower weight. This is a good example of how the MDO methodology can educate the designer about the nature of the design space and also uncover synergisms that might be overlooked by using a more traditional design methodology. In this case, the designer could

select one of the configurations for further study based on constraints that cannot be modeled mathematically.

The drag at the intersection of the strut and the engine pylon has not been calculated with a high-fidelity method. The existing drag model uses an empirical method to estimate the interference drag for the strut and the engine pylon separately, without considering their close proximity. Since the optimum spanwise position of the engines is at nearly the same buttline as the wing-strut intersection, a further drag reduction may be possible by creatively integrating the strut intersection with the engine nacelle and pylon. Future interference drag studies need to address this issue.

Since the *t/c* of the outboard wing panel is only 5%, one would expect that a larger amount of laminar flow could be achieved on the outer panel by allowing it to have a sweep angle independent of the inboard panel sweep. This optimization was performed, and the resulting design has a wing with an inboard sweep of 26.9˚, and an outboard sweep of 19.3˚. The takeoff gross weight of this design is 476,717 lb., which is a 0.9% savings relative to the single-sweep design. Since the structural analysis does not model the additional weight and complexity that would be required at this discontinuous joint, the actual weight savings may be negligible, or the weight may actually increase.

4.2.   *Understanding the Optimum Configurations*

To gain a better understanding of how the strut-braced wing configuration achieves the dramatic increase in *L/D*, a comparison of the drag breakdown is shown in Figure 4-5. The absolute drag is shown because the reference areas are different, and the optimizer determines the optimum cruise altitude for each design, resulting in different dynamic pressures. The absolute drag also drives the fuel consumption through the required thrust and hence the required engine size. The shaded bars show how the various components of the drag add up to form the total drag at the average cruise condition. Starting from the top, the bars represent the wing-strut interference drag, the wing-fuselage and strut-fuselage interference drag, the wave drag, the tail parasite drag, the strut parasite drag, the wing parasite drag, the total parasite drag of the engine nacelles, the fuselage parasite drag, and the induced drag. The wing-strut interference drag is actually plotted at the top of the last two bars, but the predicted values are too small to be visible on the chart. Note that the parasite drag of the fuselage and tails is nearly equal for the four designs, since only the wing geometry was allowed to change.
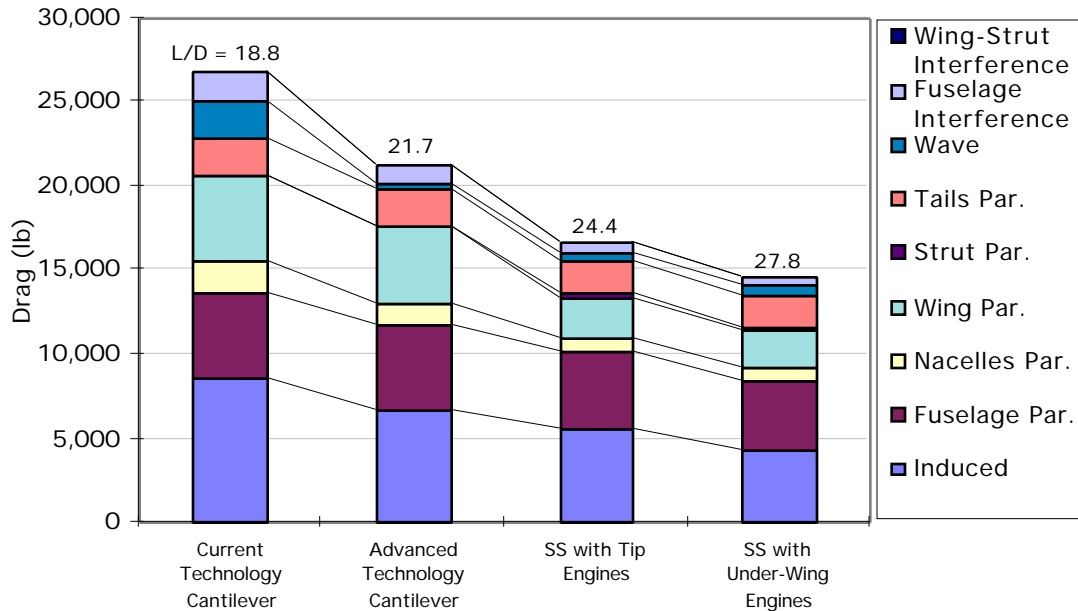
Figure 4-5: Drag comparison

The most dramatic change in drag for the advanced technology cantilever design relative to the current technology cantilever configuration is the reduction in induced drag due to the increase in span and decrease in weight and wing area. The average cruise lift coefficient decreased from 0.46 for the current technology configuration to 0.44 for the advanced technology configuration. The nacelle drag is somewhat smaller, since the higher *L/D* and lower weight of the optimum cantilever design reduce the required thrust, which results in smaller engines. The wing parasite drag actually decreased slightly, since 9.3% of the wing area became laminar. The wave drag was significantly reduced by the added sweep.

The optimum single-strut design with tip engines shows a further reduction in induced drag. The induced drag *coefficient* is actually slightly larger than the induced drag coefficient of the advanced technology cantilever design, but the large reduction in wing area resulted in a decrease in the *absolute* induced drag. The air density is also lower, since the optimum average cruise altitude increased from 35,987 ft. to 39,432 ft. The interaction of the tip-mounted engines with the wingtip vortex results in a 12.5% savings in induced drag, and a 4.9% savings in total drag for this design (relative to the same configuration with no induced drag reduction due to the tip engines). This drag savings would translate to a savings of 3.3% in takeoff gross weight.

Since the strut allows a smaller *t/c*, the wing can unsweep without a wave drag penalty. The reduction in sweep allows 32% of the wing area to become laminar. The strut also has some

parasite drag, but since it has a small chord and a low sweep angle, it is completely laminar and has very little drag.

The optimum single-strut design with under-wing engines shows the most significant reduction in induced drag, since the span increased to 258.7 ft. The smaller wing area and decreased air density due to a further increase in cruise altitude to 41,900 ft. also reduced the absolute drag. Further unsweeping of the wing to 24.5˚ results in 46% of the wing becoming laminar.

The interference drag is currently estimated using the low-speed data and empirical equations presented in Hoerner's *Fluid-Dynamic Drag* [31]. The Hoerner data shows that the wing-fuselage interference drag can be reduced with an increase in sweep. Since the advanced technology cantilever design has more sweep than the current technology cantilever design, the interference drag is lower, despite the increase in thickness. The Hoerner data shows that the wing-fuselage interference drag is a function of $(t/c)^3$. Additionally, the drag coefficient is normalized by the chord squared over the reference area squared. Therefore, a wing-fuselage intersection with a large t/c and large chord will have high interference drag, and an intersection with a small t/c and small chord will have low interference drag. Since the strut-braced wing has a smaller t/c and a much smaller wing root chord relative to the cantilever designs, it achieves a significant reduction in the wing-fuselage interference drag.

The main concern with strut-braced wing configurations has traditionally been the interference drag at the wing-strut intersection. However, since the average t/c and the average chord are both relatively small at the intersection, the interference drag is almost negligible. The reliability of this prediction is somewhat questionable, since the Hoerner data does not include transonic effects. Therefore, detailed CFD and experimental studies need to be performed to locally shape the intersection geometry to avoid a large interference drag penalty.

Figure 4-6 shows the weight breakdown for the four designs. Starting from the top, the three shaded bars represent the fuel weight, the wing and strut weight, and the zero-fuel weight minus the weight of the wing and strut.

700,000

600,000

500,000

Weight (lbs)

400,000

300,000

200,000

100,000

0

632,081

258,116

77,318

296,647

Current
Technology
Cantilever

568,031

209,249

79,420

279,363

Advanced
Technology
Cantilever

488,990

165,798

55,544

267,648

SS with Tip
Engines

481,236

148,473

68,070

264,693

SS with
Under-Wing
Engines

□ Fuel
■ Wing and Strut
■ Zero Fuel - Wing
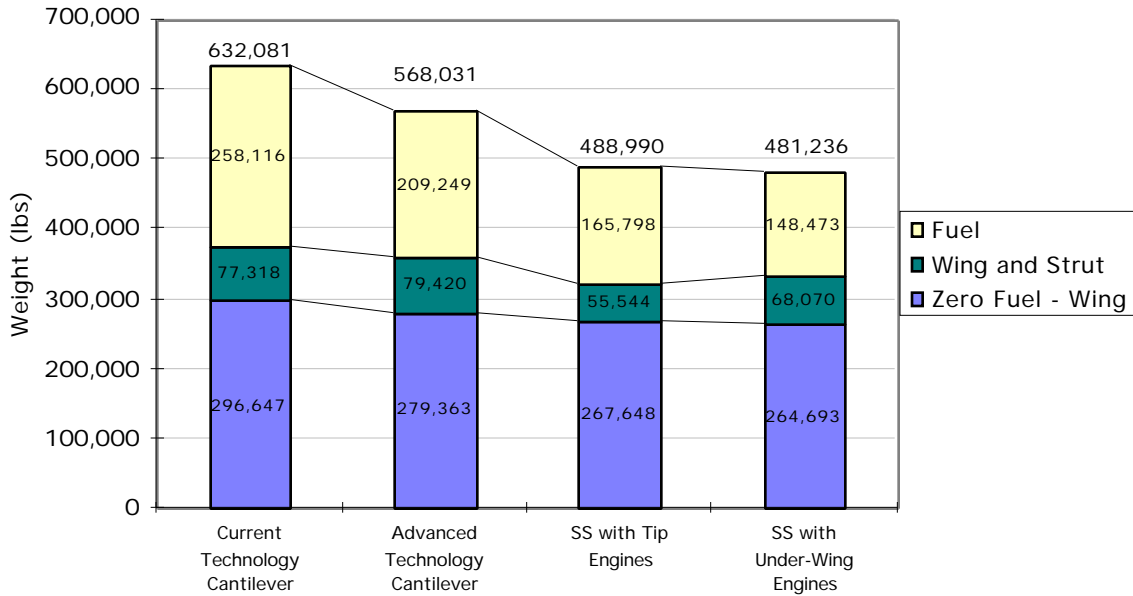
Figure 4-6: Weight comparison

Because of the increased cruise efficiency, the advanced technology cantilever design shows a 49,000 lb. fuel weight savings relative to the current technology configuration, and the optimum single-strut designs show a fuel weight savings of 92,000 lb. and 110,000 lb., respectively

The wing weight of the advanced technology cantilever design actually increased slightly due to the increase in span from 199.9 ft. to 206.6 ft. The strut-braced wing configurations achieved lower wing weights than the cantilever designs, even though the aspect ratios increased from 8.7 and 9.8 to 10.3 and 20.5. This counterintuitive result can be understood by looking at Figure 4-7. It shows the wing weight vs. aspect ratio for a series of cantilever and strut-braced configurations. The span was fixed for each design, and the rest of the design variables were optimized for minimum takeoff gross weight. The rightmost point on each curve corresponds to a wing with a span of 262.5 ft., which is equivalent to the 80 meter gate box limit. The three curves represent a cantilever wing, a strut-braced wing with tip-mounted engines, and a strut-braced wing with under-wing engines at an optimum spanwise position. The strut-braced wings clearly pay a much smaller weight penalty for an increase in aspect ratio.

Notice that the strut-braced wing curves in Figure 4-7 diverge at an aspect ratio of 9.4. As the aspect ratio of the strut-braced wing with tip-mounted engines increases above this point, the wing weight increases rapidly since a significant amount of stiffness must be added to the wing to prevent the tip engines from striking the ground during a taxi bump. However, if the spanwise

position of the engines is allowed to become a design variable, the engines tend to move inboard (thus sacrificing the induced drag reduction due to tip-mounted engines), and the span can increase without a large weight penalty. The upper limit for a strut-braced wing with under-wing engines is an aspect ratio of 21.1.
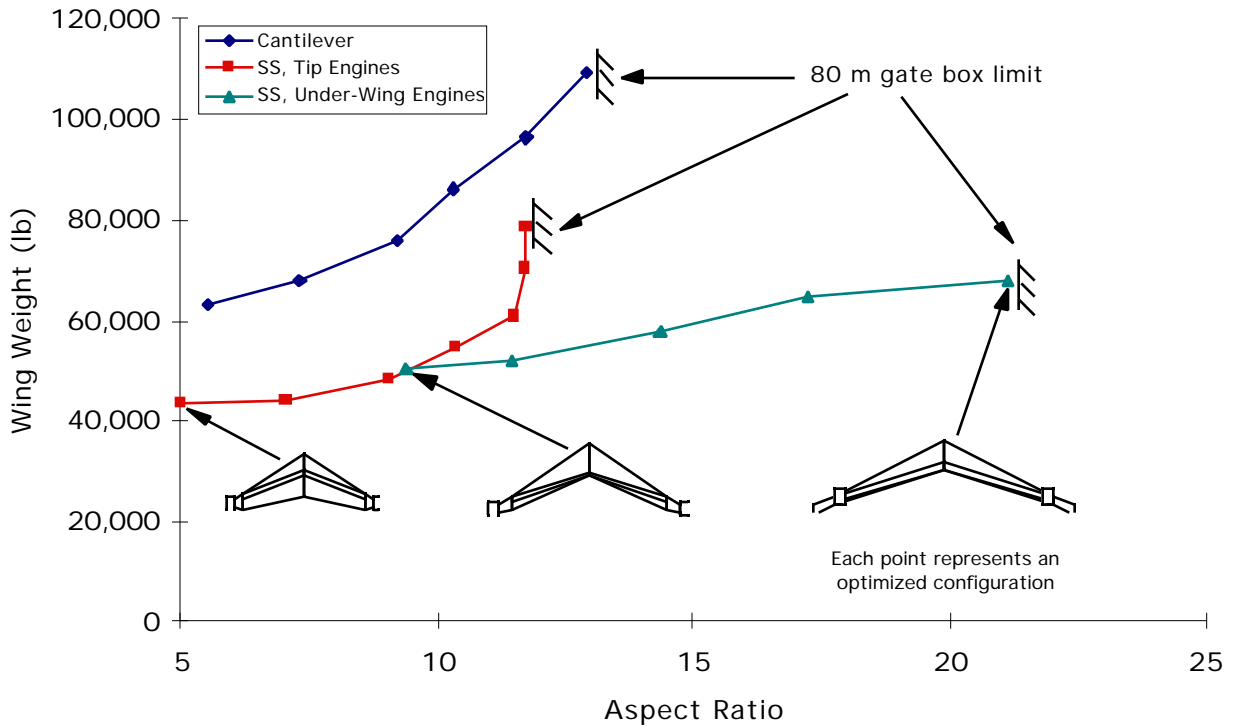
Figure 4-7: Wing weight vs. aspect ratio

The cost breakdowns, shown in Figure 4-8, were estimated using the FLOPS cost model. Beginning from the top, the shaded bars represent the acquisition cost (AC), direct operating cost (DOC), and indirect operating cost (IOC). The costs are shown in year 2000 dollars. The fuel price was assumed to be $1.00 per gallon, and the airframe production quantity was assumed to be 1,000. A 30 year lifetime was used with a passenger load factor of 65%.

For this set of assumptions, the largest cost savings for the strut-braced wing configurations is seen in the direct operating cost (DOC). This is a result of the large fuel weight reduction due to the increased *L/D*.
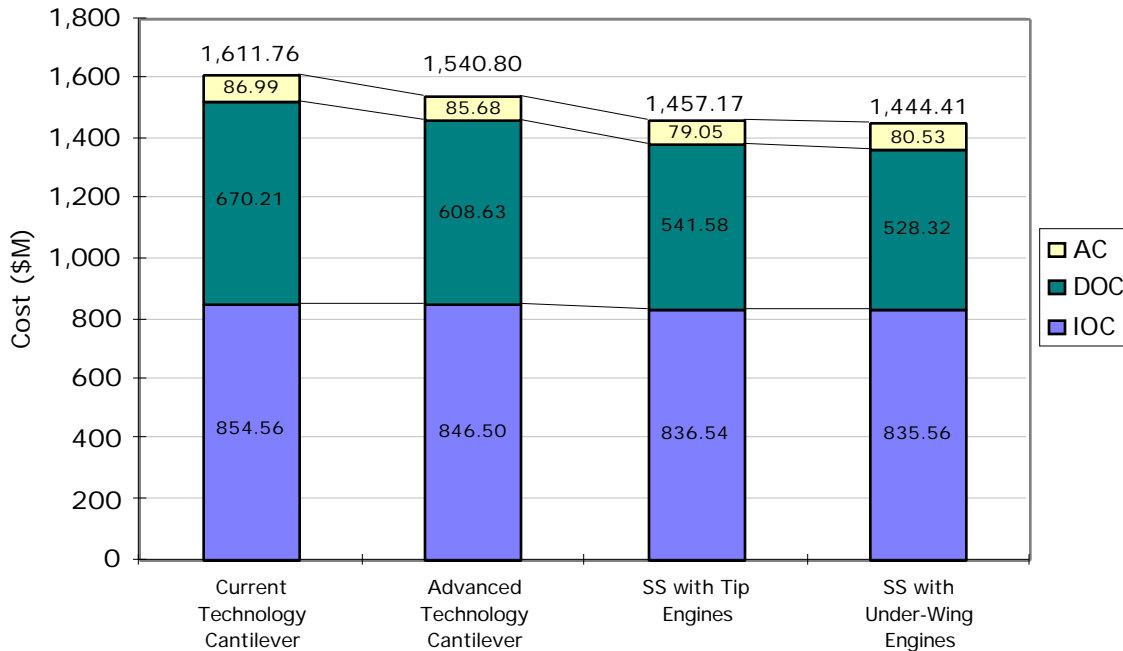
Figure 4-8: Cost comparison

4.3. *Why does the optimum cantilever design show such a large weight savings?*

The advanced technology optimum cantilever configuration has a 64,050 lb. (10.1%) weight savings relative to the current technology cantilever configuration (Table 4-1). Since the optimum cantilever configuration in Figure 4-2 looks very similar to the current technology baseline cantilever configuration in Figure 4-1, the reason for the large weight savings is not immediately apparent.

The weight savings is due to the cumulative effects of:

- Allowing the optimizer to optimize the span, sweep, chord, and *t/c* distributions for minimum takeoff gross weight.
- Scaling the engine weight and size in proportion to the required thrust with the rubber engine sizing methodology.
- Optimizing the aerodynamic load distribution for minimum trim drag with the assumption of relaxed static stability.
- Assuming that the wing can achieve partial laminar flow via the transition Reynolds number vs. sweep relationship shown in Section 3.3.2.

41

Each of these effects is shown independently in Table 4-2. The weight breakdown comparison is shown in Figure 4-9. The first column represents the current technology baseline cantilever configuration.

The design in the second column was created by allowing the optimizer to optimize the wing shape for minimum takeoff gross weight without introducing any of the advanced technology assumptions. The optimizer chose to reduce the span, increase the sweep, and reduce the t/c. The cruise L/D increased from 18.8 to 19.7, and the wing weight increased slightly, resulting in a total weight savings of 11,580 lb. When Boeing designed the 777, they most likely used a weight growth margin to accommodate future derivative configurations. Therefore the wing of the 777 was designed to handle a slightly larger takeoff gross weight. The configurations shown in this work were designed with no weight growth margin. If a weight growth margin had been used, the weight savings of the optimum cantilever configuration would have been smaller.

The next three columns were created by keeping the configuration shape fixed and independently introducing rubber engine sizing, relaxed static stability, and partial laminar flow. These technology insertions result in a weight savings of 7,795 lb., 9,841 lb., and 12,283 lb., respectively.

The sum of these independent effects is: 11,580 + 7,795 + 9,841 + 12,283 = 41,499 lb. However, when the configuration is optimized with all of the advanced technology assumptions, the savings in takeoff gross weight is 64,050 lb. This is a quantitative example of synergy–the whole is greater than the sum of the parts. The use of the MDO methodology allows the effect of each technology assumption to ripple through the entire system which amplifies the weight savings. Additionally, the optimizer evolves the shape of the configuration to take maximum advantage of the advanced technology assumptions.

Table 4-2: Configuration comparison for advanced technology insertions

	Current Technology Cantilever	Current Technology Optimum	Rubber Engine Sizing	Relaxed Static Stability	Partial Laminar Flow	Advanced Technology Cantilever
Wing Span (ft)	199.9	195.6	199.9	199.9	199.9	206.6
Wing Area (ft^2)	4,607	4,575	4,607	4,607	4,607	4,365
Aspect Ratio	8.7	8.4	8.7	8.7	8.7	9.8
Inboard Wing 1/4-Chord Sweep (deg)	31.6	33.3	31.6	31.6	31.6	36.7
Outboard Wing 1/4-Chord Sweep (deg)	31.6	33.3	31.6	31.6	31.6	36.7
Strut 1/4-Chord Sweep (deg)	N/A	N/A	N/A	N/A	N/A	N/A
Wing t/c at the Centerline	15.1%	14.8%	15.1%	15.1%	15.1%	15.4%
Wing t/c at the Chord Breakpoint	10.9%	9.2%	10.9%	10.9%	10.9%	10.5%
Wing t/c at the Tip	10.9%	9.2%	10.9%	10.9%	10.9%	10.5%
Strut t/c	N/A	N/A	N/A	N/A	N/A	N/A
Cruise L/D	18.8	19.7	18.6	19.3	19.4	21.7
Specific Range (nmi/1000 lb)	26.0	27.8	26.1	27.0	27.2	33.5
Seat Miles per Gallon (seats*nmi/gal)	60.5	63.8	60.9	62.6	63.3	74.7
Wing Weight (lb)	77,318	79,841	76,628	76,514	76,639	79,420
Takeoff Gross Weight (lb)	632,081	620,501	624,286	622,240	619,798	568,031
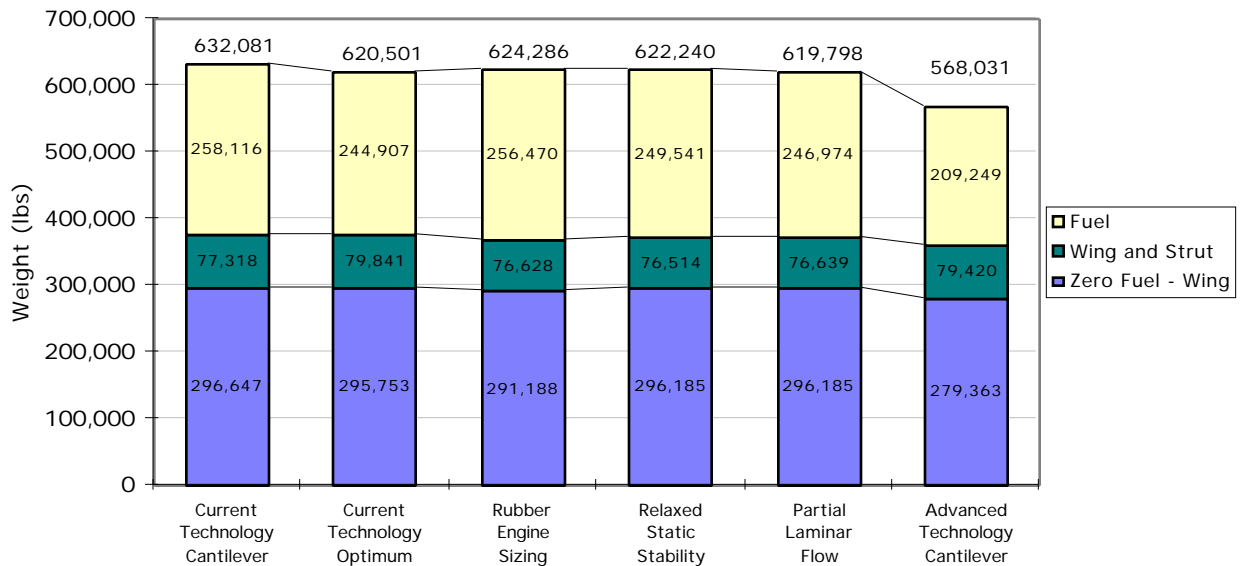
Figure 4-9: Weight breakdown comparison for advanced technology insertion study

4.4. Convergence History

Figure 4-10 shows the convergence history for the advanced technology optimum cantilever configuration. The starting point for the optimization was the baseline cantilever configuration. The design variables are shown in the first ten plots, and the objective function (takeoff gross weight) is shown in the final plot. Notice that the wing centerline chord stays at 52 ft., which is the wing centerline chord of the Boeing 777. A lower side constraint was placed on the wing

centerline chord to provide enough room for the 777 landing gear to retract into the wing. This side constraint is active for the optimum configuration.
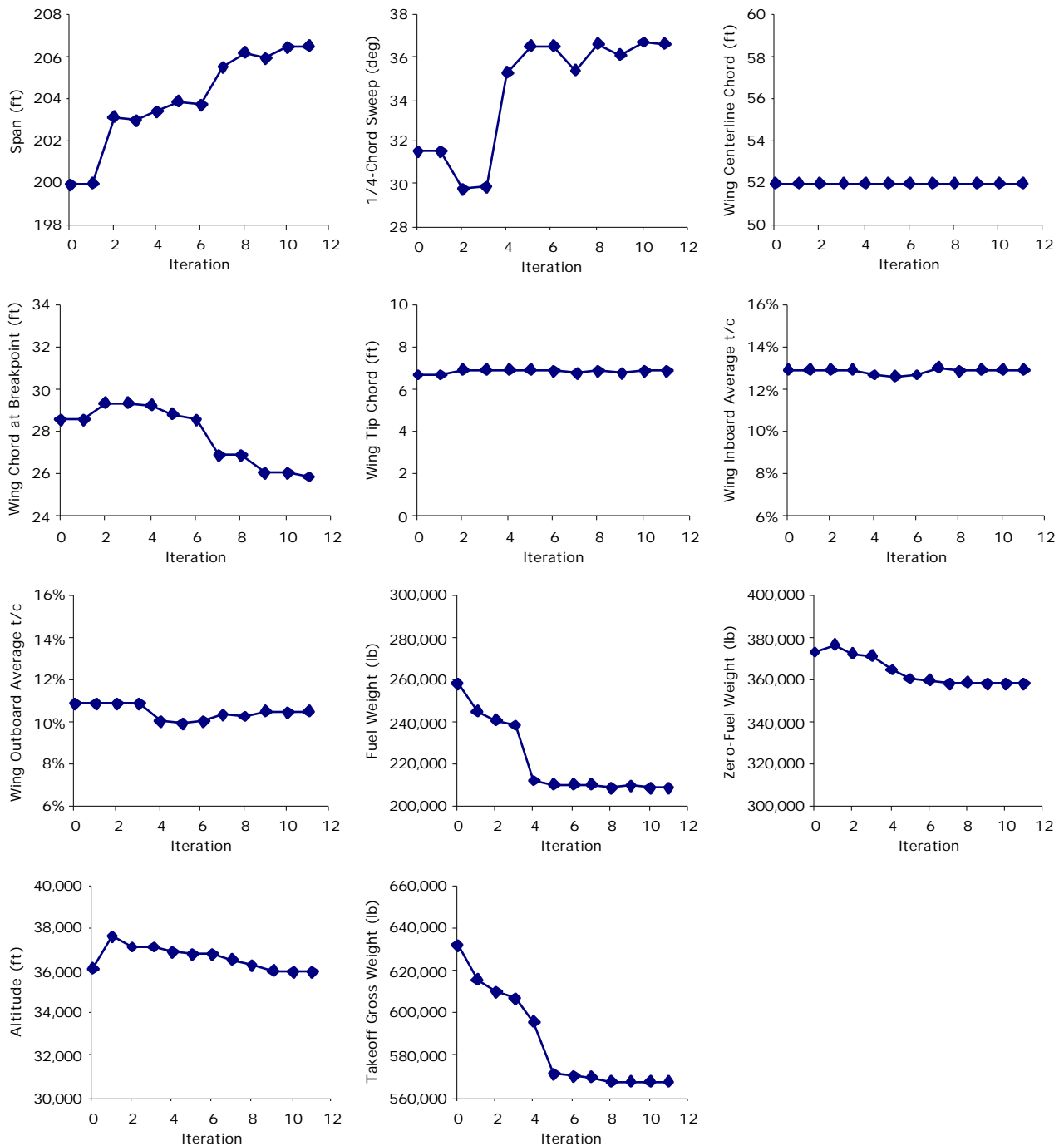
Figure 4-10: Convergence history from baseline cantilever to optimum cantilever

4.5. Why is the sweep so high?

Since the amount of laminar flow decreases with increased sweep due to cross-flow instability, we initially expected the optimum strut-braced wing to be driven to a very low sweep angle to maximize the amount of laminar flow. However, the optimum design has a wing with a sweep of 27.3˚ (Figure 4-11).

To understand why the optimizer chose this sweep, two additional designs were created by forcing the wing and strut quarter-chord sweep angles to 50% of their original sweep (Figure 4-12), and to zero sweep (Figure 4-13). With the sweep angles fixed, the configurations were then optimized by allowing the rest of the design variables to remain free. The results are shown in Table 4-3.

As the wing is forced to unsweep, the wing root t/c becomes smaller in an attempt to avoid a transonic wave drag penalty and a large interference drag penalty. The t/c values of the outboard wing panel and the strut are already up against the minimum allowable t/c constraint of 5%, so they cannot get thinner. As a result, the wing weight increases by 6,244 lbs. for the 50% sweep configuration, and by 8,101 lbs. for the fully unswept configuration.

Figure 4-11: Original optimum single-strut configuration

Figure 4-12: Partially unswept configuration

Figure 4-13: Fully unswept configuration

Table 4-3: Configuration comparison for unswept configurations

	Original Optimum Design	50% Sweep	No Sweep
Wing Span (ft)	198.9	203.9	199.5
Wing Area (ft2)	3,829	4,593	4,840
Aspect Ratio	10.3	9.1	8.2
Inboard Wing 1/4-Chord Sweep (deg)	27.3	13.7	0.0
Outboard Wing 1/4-Chord Sweep (deg)	27.3	13.7	0.0
Strut 1/4-Chord Sweep (deg)	17.7	8.9	0.0
Wing t/c at the Centerline	13.3%	10.1%	8.4%
Wing t/c at the Chord Breakpoint	5.0%[**]	5.0%[**]	5.0%[**]
Wing t/c at the Tip	5.0%[**]	5.0%[**]	5.0%[**]
Strut t/c	5.0%[**]	5.0%[**]	5.0%[**]
Cruise L/D / Max L/D	24.4 / 27.4	22.5 / 27.8	22.1 / 27.5
Specific Range (nmi/1000 lb)	43.7	37.6	36.3
Seat Miles per Gallon (seats*nmi/gal)	94.2	83.1	81.0
Wing Weight (lb)	55,544	61,788	63,645
Takeoff Gross Weight (lb)	488,990	522,409	530,206

[**] The wing mid, tip, and strut *t/c* values have converged to the minimum allowable value of 5%.

Figure 4-14 presents the drag breakdown for the three configurations. As the wing is unswept, the amount of laminar flow on the wing increases from 31.9% on the original configuration to 46.6% and 59.8%, respectively for the unswept configurations. However, the large increase in required wing area reduces the savings in absolute parasite drag to a minimal amount. The most significant penalty for unsweeping the wing is the large increase in the wave drag.

The weight breakdown is shown in Figure 4-15. The largest weight change is the weight growth of the wing due to the reduced *t/c* of the unswept configurations. The increase in wing weight requires a larger wing area, which results in more drag, which requires more fuel, which also requires more wing area, and so on. This is a classic example of how the ripple-through effect can amplify a small weight growth in one component into a significant increase in the takeoff gross weight.
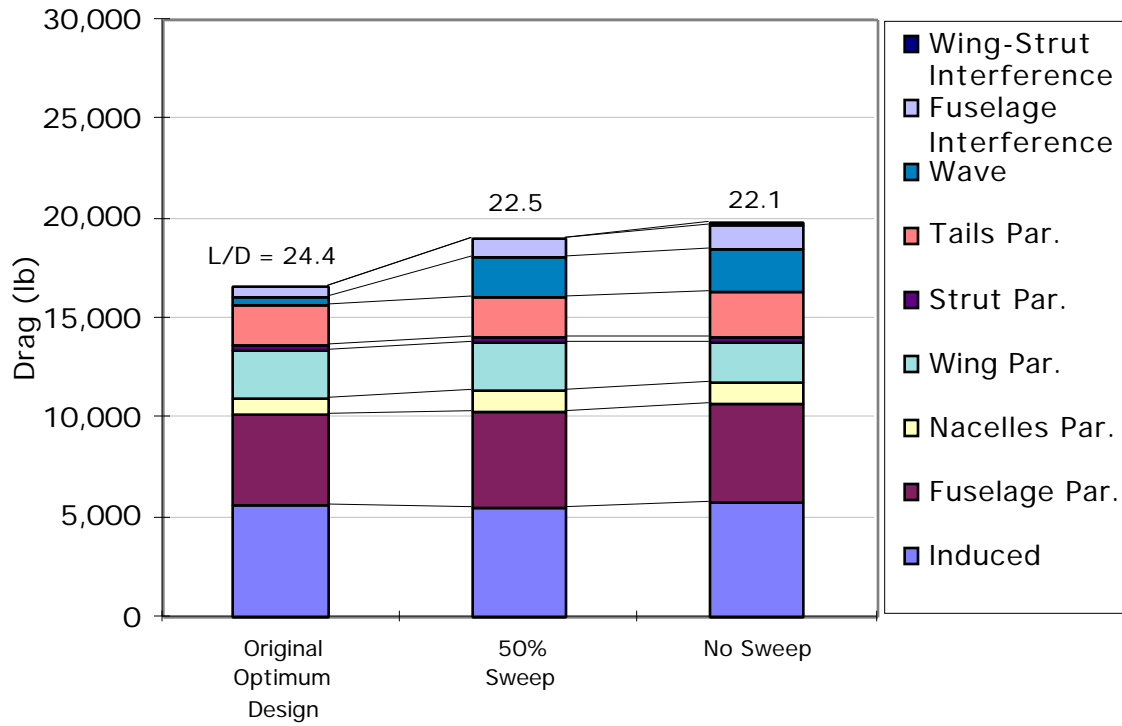
Figure 4-14: Drag comparison for unswept configurations
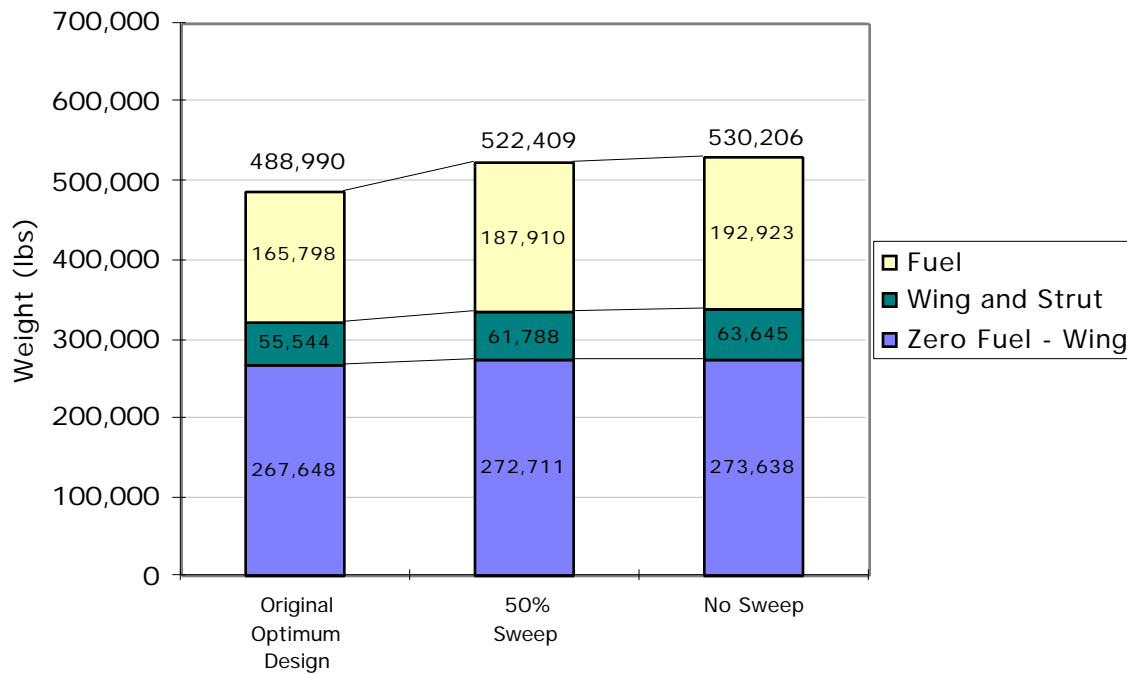
Figure 4-15: Weight comparison for unswept configurations

With the current assumptions and technology constraints, the optimum strut-braced wing configurations have sweep angles that are higher than our initial expectations. By creatively breaking down the traditional design constraints with advanced technology, the optimum wing sweep can be reduced, resulting in even greater performance.

For example, to avoid the rapid growth of wing weight with decreasing t/c, a load alleviation strategy could be used to shift the load distribution inboard at the critical load cases. To avoid the dramatic increase in wave drag with a decrease of sweep, a porous airfoil could be used to weaken the shock and improve the transonic drag rise characteristics.

This type of technology insertion study can be performed quite easily with the MDO code by changing a given technology level or modeling assumption, and re-optimizing the configuration to take maximum advantage of the change. The following sections will show sensitivities to the amount of laminar flow on the wing and strut, the airfoil technology, the wing-strut interference drag, and the design Mach number. The optimum single-strut design with tip-mounted engines is used as the baseline configuration for these studies.

4.6. Sensitivity to Laminar Flow

Figure 4-16 shows the laminar flow on the advanced technology optimum cantilever configuration. The shaded areas represent the laminar flow regions. Because of the relatively high sweep angle, only 5% of the chord is laminar near the wing root, and 20% is laminar at the tip. Figure 4-17 shows the amount of laminar flow on the optimum strut-braced configuration. The strut is displaced aft of the wing for the illustration. The lower sweep and smaller chord Reynolds numbers of the strut-braced configuration allows it to achieve 25% laminar flow near the wing root, 61% at the tip, and 100% laminar flow on the strut.
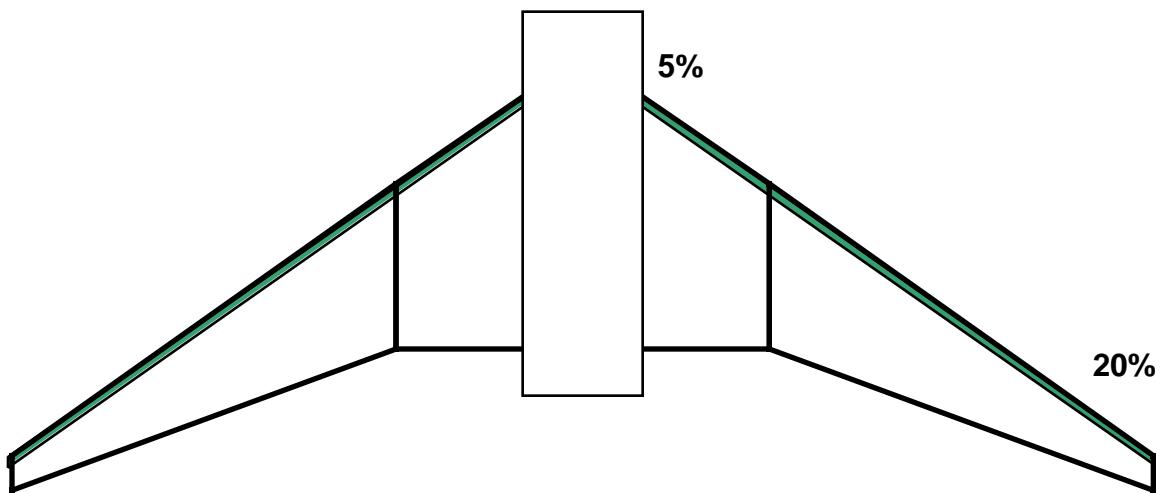
Figure 4-16: Laminar flow on advanced technology optimum cantilever design (shaded regions are laminar)
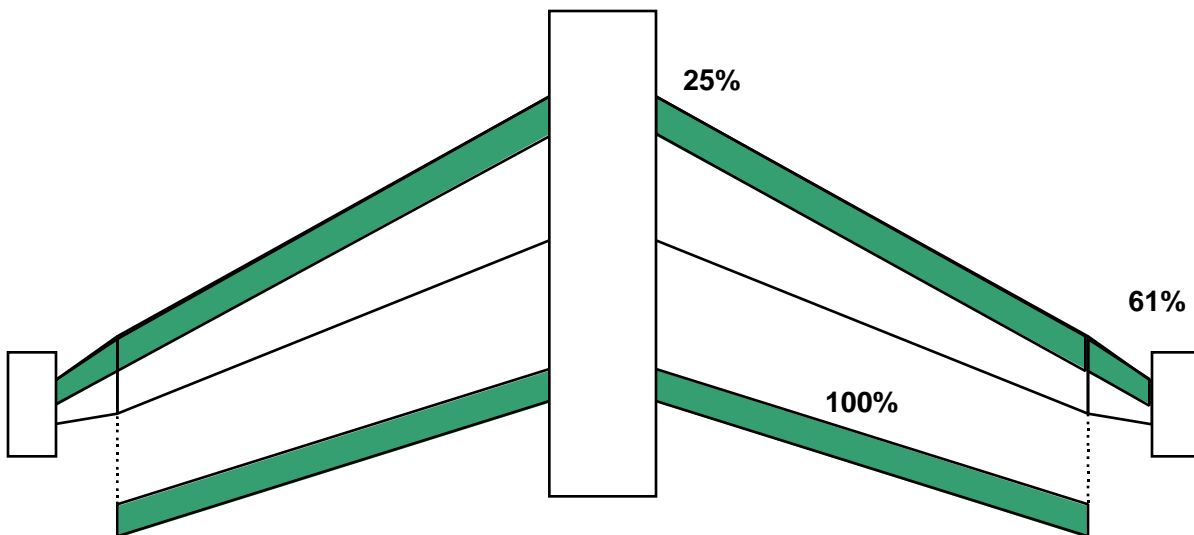
Figure 4-17: Laminar flow on optimum single-strut design (shaded regions are laminar)

Since laminar flow was originally perceived as a key to the success of the strut-braced wing configuration, a sensitivity study was performed with respect to the amount of laminar flow (Figure 4-18). The amount of laminar flow on the wing and strut was varied between 0% and 100% (by changing the transition Reynolds number), and the single-strut configuration with tip-mounted engines was optimized for minimum takeoff gross weight at each point. About 32% of the wing area is laminar for the original optimum single-strut design. The change in takeoff gross weight between a fully turbulent wing/strut and a fully laminar wing/strut is about 104,000 lb. The fuselage, nacelles, and tails are assumed to be fully turbulent, and they represent 63% of the total wetted area for the advanced technology cantilever design, 62% for the single-strut design with tip-mounted engines, and 58% for the single-strut design with under-wing engines.
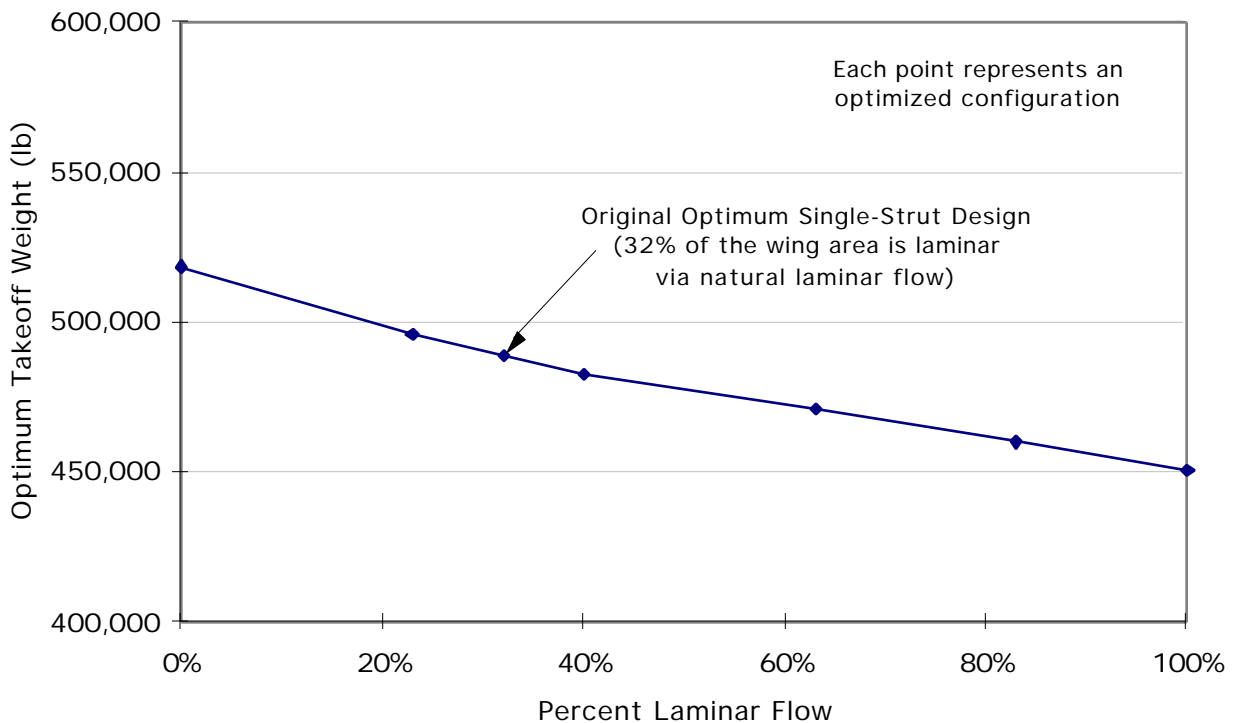
Figure 4-18: Sensitivity of the single-strut design to the amount of laminar flow

4.7.   Sensitivity to the Airfoil Technology Factor

The shape and performance of the optimum wing design is very sensitive to the airfoil technology. The airfoil technology is modeled in the MDO code by the airfoil technology factor in the Korn equation [27]. A value of 0.87 corresponds to a NACA 6-series airfoil section, while a value of 0.95 corresponds to a supercritical section.

The airfoil technology factor was varied from 0.86 to 0.98, and the configuration was re-optimized at each point. Since the higher technology airfoils have better drag rise characteristics, the wing tends to unsweep with increasing airfoil technology, resulting in more laminar flow and less drag. This study shows that changing the airfoil from a NACA 6-series section to a supercritical section would result in a weight savings of about 40,000 lb.
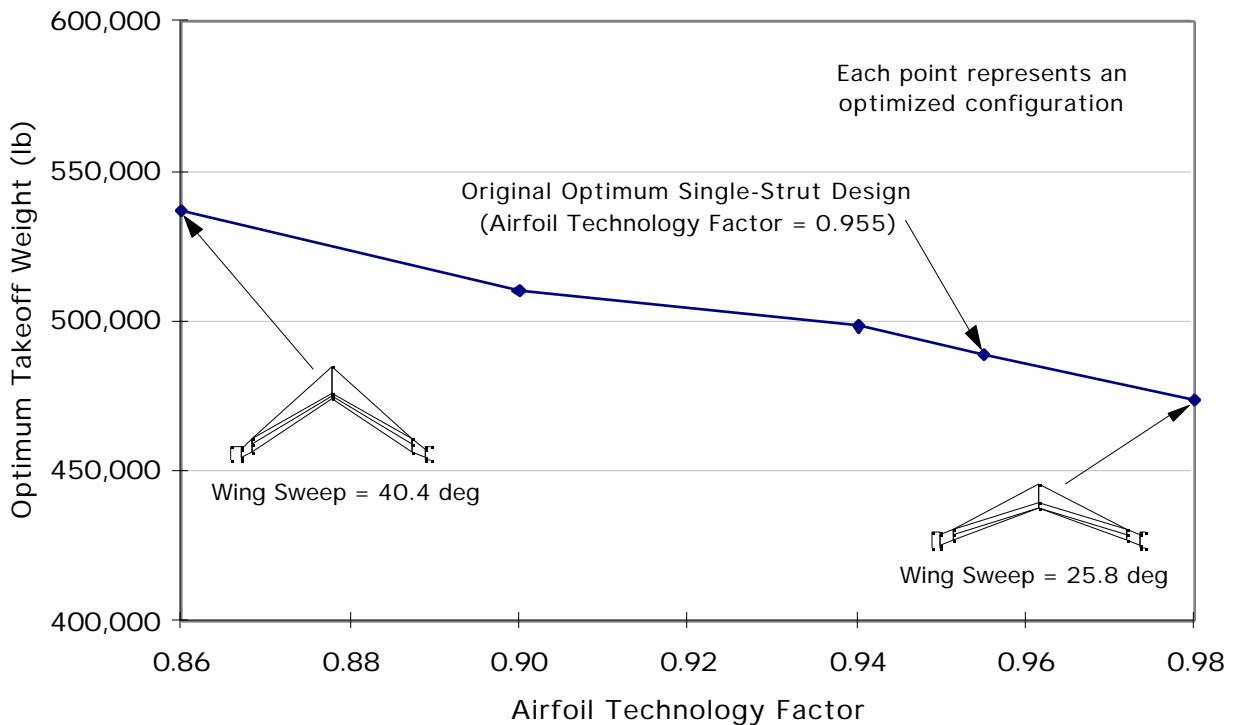
Figure 4-19: Sensitivity to the airfoil technology factor

4.8.   Sensitivity to the Wing-Strut Interference Drag

Since the interference drag calculations are currently based on the low-speed Hoerner data, the accuracy of the wing-strut interference drag requires more detailed analysis. To evaluate the impact of a potential increase in the wing-strut interference drag, a sensitivity study was performed by multiplying the Hoerner-predicted wing-strut interference drag by various amounts (Figure 4-20). Even when the Hoerner prediction is multiplied by a factor of 100, the takeoff gross weight only increases by about 27,700 lbs. The accuracy of this prediction will be improved in the future by creating a response surface from detailed CFD calculations.
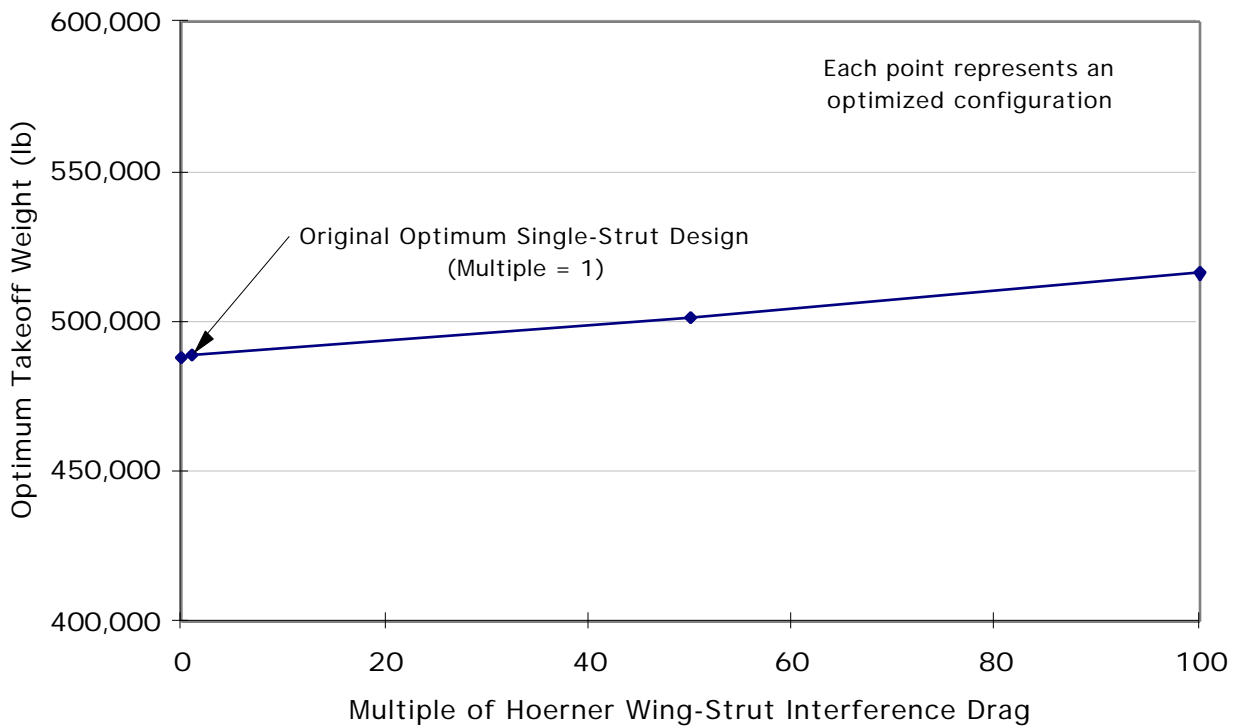
Figure 4-20: Sensitivity to the magnitude of the wing-strut interference drag

4.9. Sensitivity to the Design Mach Number

The single-strut and cantilever configurations are quite sensitive to the design Mach number, as shown in Figure 4-21. The planforms of the optimum strut-braced configurations are shown for Mach 0.6 and 0.9. At Mach 0.6, the optimum strut-braced configuration shows a weight savings of 55,910 lb. (12%) over the cantilever configuration. At Mach 0.9, the strut-braced configuration has a 82,357 lb. (14%) weight savings over the advanced technology optimum cantilever configuration. Therefore, the advantage of the strut-braced wing increases with increasing design Mach number.
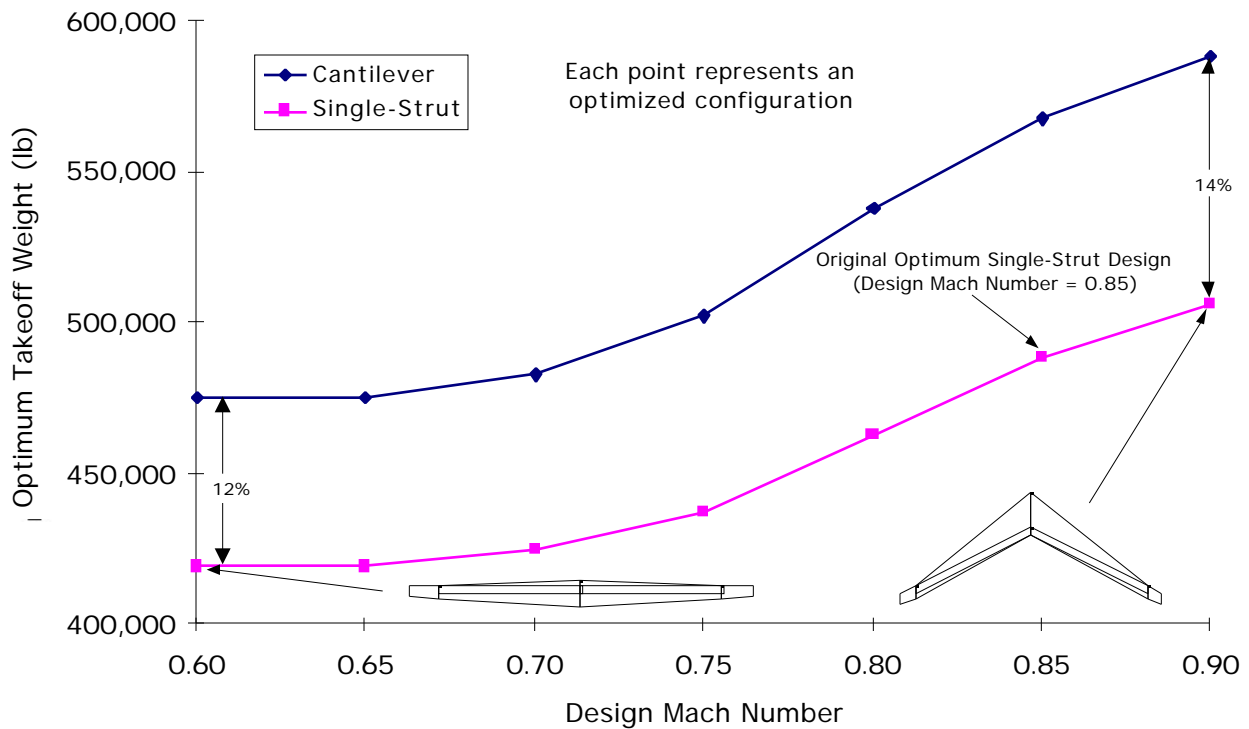
Figure 4-21: Optimum takeoff weight vs. design Mach number

4.10. Sensitivity to Aeroelastic Tailoring and the Use of Composites

Aeroelastic tailoring and the use of composites can significantly reduce the wing weight. If the entire configuration is re-optimized around the lighter wing structure, the takeoff gross weight can be reduced by an amount greater than the wing weight reduction alone via the "ripple-through" effect.

The use of aeroelastic tailoring is modeled in FLOPS with a correction factor ranging from 0 (no aeroelastic tailoring) to 1 (full use of aeroelastic tailoring). A value of 1 corresponds to a 10% savings in the wing bending material weight. Figure 4-22 shows the weight breakdowns for the original optimum single-strut configuration with tip-mounted engines (no aeroelastic tailoring, metal wing), the configuration optimized with aeroelastic tailoring, and two designs with the use of composites (described below). The use of aeroelastic tailoring results in a total weight savings of 5,608 lb. (1.1%) relative to the configuration with no aeroelastic tailoring.

The use of composites has been modeled using two independent methods: within the wing bending material weight estimation subroutine (wing.f) and within FLOPS. To model the use of composites within the bending material weight subroutine, the strength, stiffness, and density are adjusted to the values for a composite laminate. The use of composites is modeled in FLOPS with a correction factor ranging from 0 (no composites) to 1 (full use of composites). A value of 1 corresponds to a 40% savings in the wing bending material weight, a 17% savings in the secondary structural weight of the wing, and a 30% savings in the non-structural wing weight. The weight breakdowns for the optimum configurations with the use of composites are shown in Figure 4-22. The configuration with the use of composites modeled by the wing bending material weight subroutine has a total weight savings of 29,727 lbs. (6.1%), and the configuration with the use of composites modeled by FLOPS has a total weight savings of 31,462 lbs. (6.4%) relative to the optimum design with a metal wing.
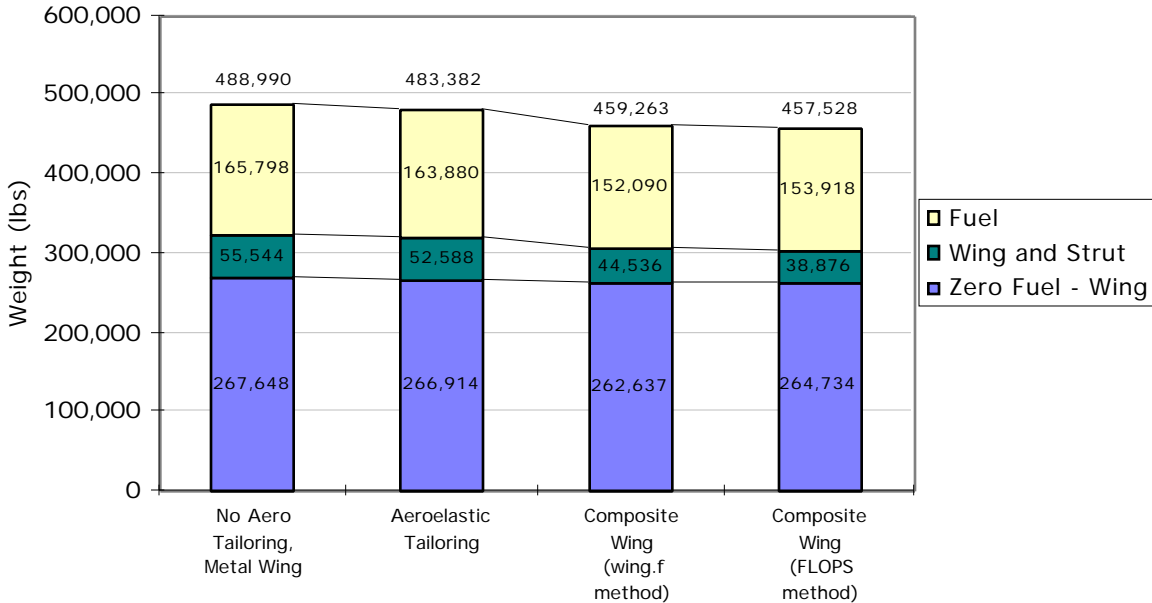
Figure 4-22: Weight comparison for aeroelastic tailoring and composites sensitivity study

4.11. Sensitivity to the Minimum t/c Constraint

In Table 4-1 the optimum thickness-to-chord ratios for the wing chord breakpoint, wing tip, and strut are at the minimum permitted value of 5%. Since the minimum permitted *t/c* was chosen somewhat arbitrarily, each single-strut design was re-optimized with no lower side constraint on the *t/c*. As shown in Table 4-4, the optimum unconstrained *t/c* for the outboard panel of the wing (from the chord breakpoint to the tip, constant *t/c*) on the tip-mounted engine design is 4.2%, and the optimum unconstrained strut *t/c* for this design is 4.96%. For the under-wing engine configuration, the optimum *t/c* for the outboard wing panel is 3.5%, and the optimum strut *t/c* is 3.7%. Even though the lower side constraints for the *t/c* parameters are inactive in those calculations, the taxi bump wingtip deflection constraint provides a natural lower limit on the *t/c* values. When this study was performed before the taxi bump deflection constraint was added to the code, the *t/c* of the outboard wing panel decreased to 2%, and the sweep of the outboard panel decreased to 0°.

To minimize the number of design variables in the original single-strut parameter set, the outboard wing quarter-chord sweep was forced to be equal to the inboard wing quarter-chord sweep angle. This is probably a good idea from a manufacturability perspective, since a kink in the wing structure may result in added structural weight and increased complexity and cost in construction. A kinked wing may also have some aerodynamic and aeroelastic problems. However, a kinked wing was still evaluated using the current math model to assess the potential weight savings.

The optimum *t/c* and sweep distribution of the wing is determined by competing structural and aerodynamic objectives. The structures subroutine wants the wing *t/c* to be large in order to maximize the moment of inertia of the wing box and minimize the wing weight. The wave drag subroutine wants the wing *t/c* to be small to minimize the transonic wave drag. The wave drag subroutine also wants the wing sweep to be large in order to minimize the wave drag. However, the friction drag subroutine wants the wing sweep to be small in order to reduce the cross-flow instability and maximize the amount of laminar flow. The structures subroutine also wants the wing sweep to be small to minimize the ratio of the structural span to the aerodynamic span (proportional to $1/\cos$).

In Table 4-4, notice that the inboard wing sweep of the tip-mounted engine configuration increased from 27.3° to 29.0°, and the outboard wing sweep decreased from 27.3° to 26.2°. This

change is even more dramatic on the under-wing engine configuration, where the inboard wing sweep increased from 24.5° to 27.6°, and the outboard wing sweep decreased from 24.5° to 15.7°.

Table 4-4: Configuration comparison for minimum *t/c* constraint sensitivity study

	Tip Engines, 5% t/c Const.	Tip Engines, No t/c Const.	U-W Engines, 5% t/c Const.	U-W Engines, No t/c Const.
Wing Span (ft)	198.9	197.4	258.7	255.6
Wing Area (ft^2)	3,829	3,709	3,259	3,142
Aspect Ratio	10.3	10.5	20.5	20.8
Inboard Wing 1/4-Chord Sweep (deg)	27.3	29.0	24.5	27.6
Outboard Wing 1/4-Chord Sweep (deg)	27.3	26.2	24.5	15.7
Strut 1/4-Chord Sweep (deg)	17.7	17.8	16.3	15.4
Wing t/c at the Centerline	13.3%	14.8%	11.9%	13.6%
Wing t/c at the Chord Breakpoint	5.0%	4.2%	5.0%	3.5%
Wing t/c at the Tip	5.0%	4.2%	5.0%	3.5%
Strut t/c	5.0%	4.96%	5.0%	3.7%
Cruise L/D	24.4	24.2	27.8	27.8
Specific Range (nmi/1000 lb)	43.7	43.5	50.6	51.4
Seat Miles per Gallon (seats*nmi/gal)	94.2	94.1	105.2	107.0
Wing Weight (lb)	55,544	54,188	68,070	63,811
Takeoff Gross Weight (lb)	488,990	487,260	481,236	473,660

In this example, the system-level objective is to minimize the takeoff gross weight of the aircraft. Figure 4-23 shows the weight breakdowns for the tip-mounted engine and under-wing engine configurations with and without the 5% *t/c* constraint. The tip-mounted engine configuration shows a weight savings of 1,730 lbs. (0.35%) and the under-wing engine configuration shows a weight savings of 7,576 lbs. (1.6%).
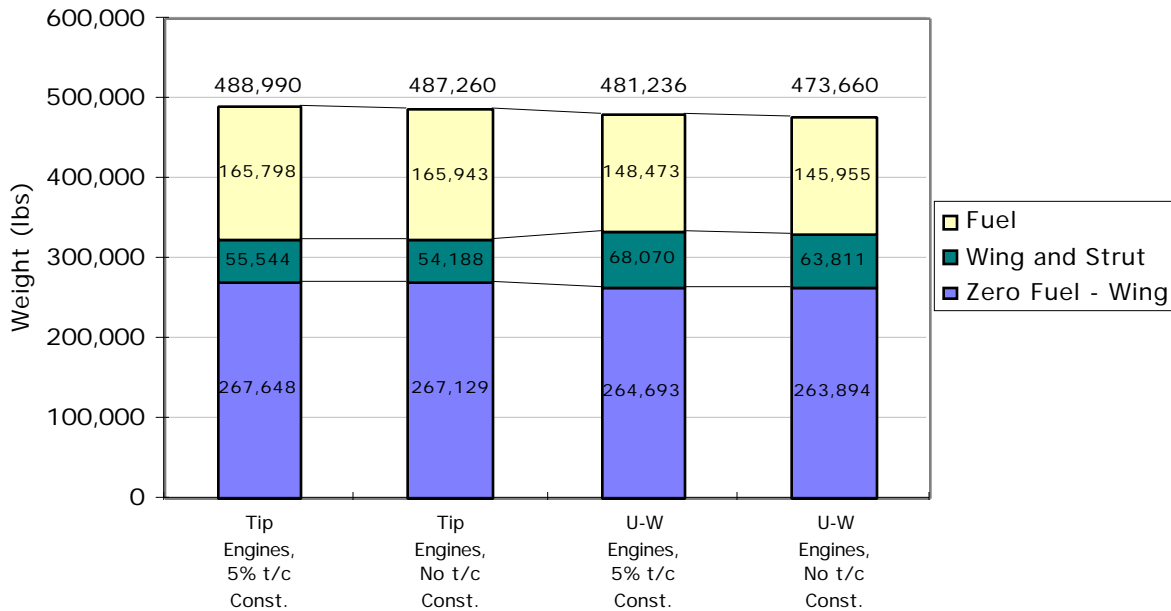
Figure 4-23: Weight comparison for minimum *t/c* constraint sensitivity study

This discussion illustrates the power of the MDO methodology. The traditional way to evaluate a set of competing objectives in a complex system is to perform parametric trade studies throughout the design space. However, a human designer can only visualize the effect of two design variables at a time, and his intuition is limited and often biased by past experience. Furthermore, each two-dimensional parametric plot is only valid when all of the other design parameters are fixed. These limitations require the design team to perform several iterations to converge on the solution. Since every design project has a deadline, there may not be enough time to perform enough iterations to find the optimum solution. The MDO methodology concurrently evaluates all of the competing objectives mentioned above. It implicitly determines the optimum values of sweep and *t/c* to maximize the performance of the total system.

4.12. *L/D and Specific Range vs. Mach and Altitude*

Figure 4-24 shows the variation of *L/D* vs. Mach number and altitude for the optimum single-strut design with tip-mounted engines. Notice the large plateau with *L/D* values ranging from 26 to 27. As the Mach number increases, the altitude for maximum *L/D* increases. Also notice how *L/D* drops off significantly as the Mach number increases through the range of 0.8 to 0.9.

Figure 4-25 shows the specific range vs. Mach number and altitude. The specific range is plotted in nautical miles per 1,000 lbs. of fuel. The maximum specific range of 46.2 nmi/1,000 lbs. occurs near Mach 0.81 at 45,000 ft.
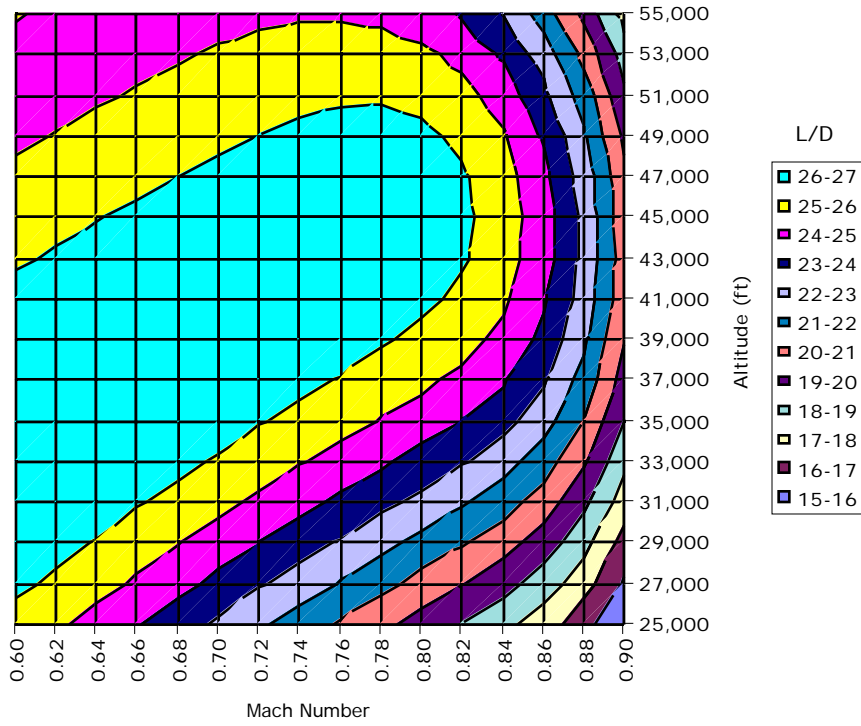
Figure 4-24: *L/D* vs. Mach number and altitude
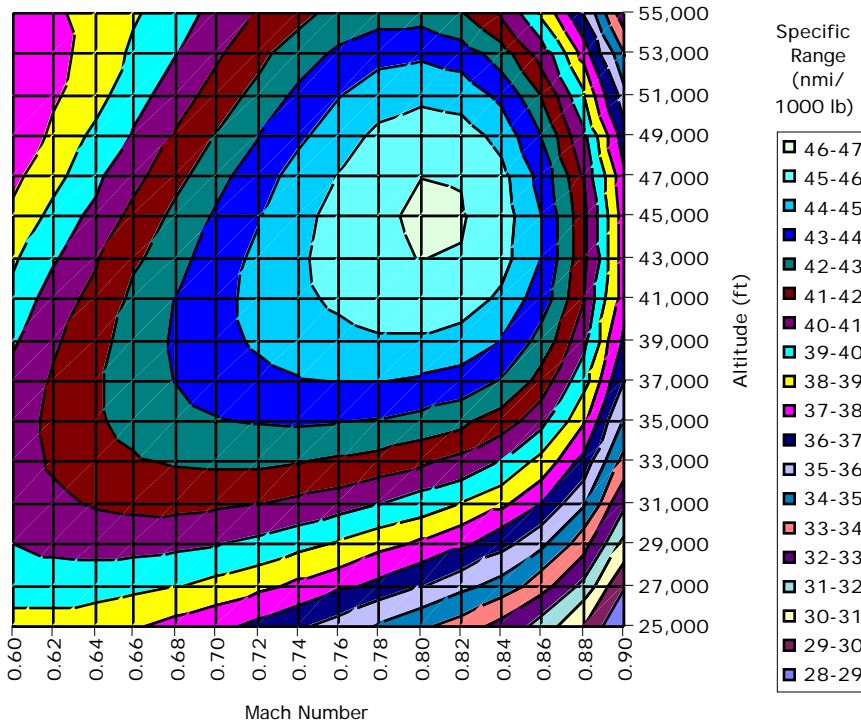
Figure 4-25: Specific range vs. Mach number and altitude

Figure 4-26 shows *L/D* and specific range vs. Mach number at the optimum cruise altitude of the original single-strut design (39,432 ft.). Notice how *L/D* drops off rapidly as the Mach number increases through the range of 0.8 to 0.9. The specific range decreases for decreasing Mach numbers below 0.8 because it is proportional to the velocity.
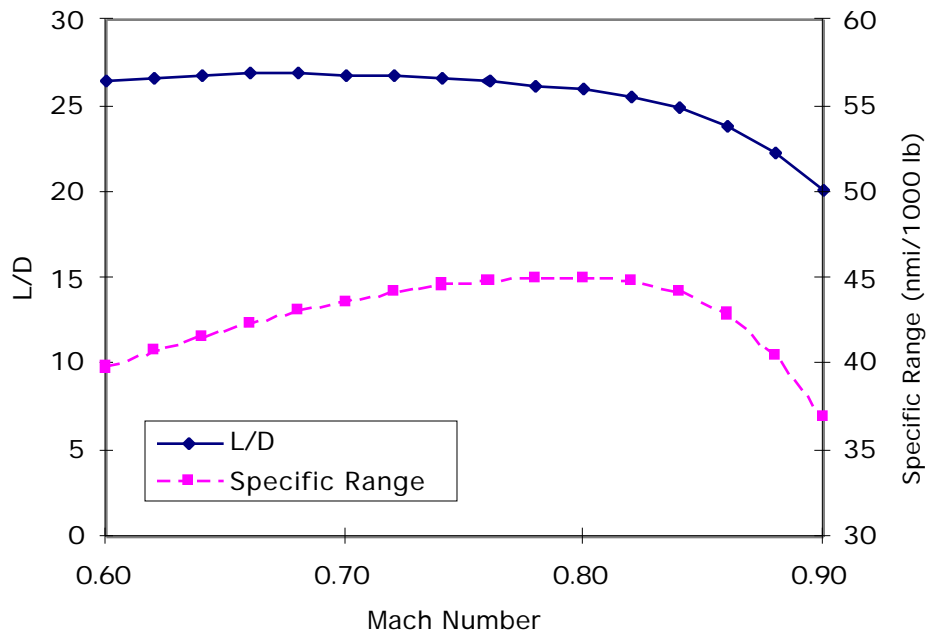
Figure 4-26: *L/D* and specific range vs. Mach number (Altitude = 39,432 ft.)

Figure 4-27 shows *L/D* and specific range vs. altitude at the cruise Mach number of 0.85. The maximum *L/D* at Mach 0.85 occurs at about 45,000 ft. However, the aircraft cannot actually fly at this Mach number and altitude, because it would violate the maximum allowable section lift coefficient constraint, resulting in a shock stall somewhere along the wing. The section lift coefficient constraint at Mach 0.85 corresponds to a maximum allowable aircraft lift coefficient of 0.52, which in turn corresponds to a maximum allowable altitude of 39,432 ft. This constraint is shown in the figure, with the feasible range of altitudes to the left of the constraint.
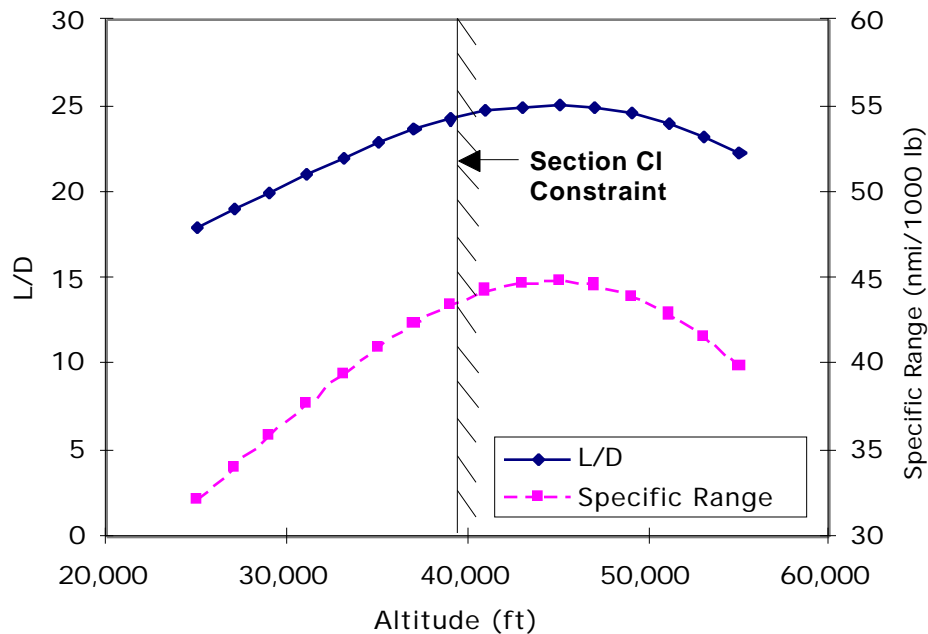
Figure 4-27: *L/D* and specific range vs. altitude (Mach = 0.85)

4.13. Trim Drag vs. CG Position

Every aircraft has a CG position that creates a load distribution corresponding to the minimum drag of the configuration. For an aircraft with a conventional tail, the minimum-drag load distribution is achieved when the horizontal tail carries a small lifting load. However, stability and control requirements impose an aft CG limit, which is ahead of the CG position for minimum drag. When the CG is ahead of the minimum-drag position, the non-optimum load distribution imposes a trim drag penalty. The non-optimum load distribution is found by specifying the CG position and requiring the pitching moment coefficient to be zero in the induced drag code. This methodology was used to create the plot shown in Figure 4-28.

Figure 4-28 shows the trim drag vs. the center of gravity (CG) position for the baseline cantilever design, the optimum single-strut design with tip-mounted engines, and the MD-11. The experimental data given in Reference [47] for the MD-11 is also shown by the discrete data points. The trim drag is plotted as a percentage of the total drag, and the CG position is plotted as a percentage of the mean aerodynamic chord (MAC). The predicted trim drag of the MD-11 is reasonably close to the MD-11 data. Since the same methodology was applied to the baseline cantilever and single-strut designs, these should be reasonably accurate as well.

The horizontal tail of the MD-11 employs a leading edge icing system and a slotted elevator to increase the effectiveness. This allows a 30% reduction in tail area relative to a conventional horizontal tail (i.e. the DC-10), which is sized with ice buildup on the leading edge, and no slotted elevator. The baseline cantilever and single-strut designs use a conventionally-sized horizontal tail. Since the horizontal tail of the MD-11 is relatively small, the trim drag increases more rapidly as the CG moves away from the minimum-drag position.

The minimum-drag CG position is at 55% MAC for the MD-11, 80% MAC for the baseline cantilever design, and 110% MAC for the single-strut configuration. The horizontal shift between the curves for the baseline cantilever and single-strut designs is the difference in MAC. The baseline cantilever design has an MAC of 26.22 ft., while the single-strut design has an MAC of 19.49 ft. The smaller MAC makes the same absolute shift in CG position appear as a larger change in percent MAC.

Note that the MD-11 curve represents a configuration where the size of the horizontal tail was sized to a set of stability and control requirements, whereas the horizontal tails of the baseline cantilever and single-strut configurations have not been sized to stability and control requirements.
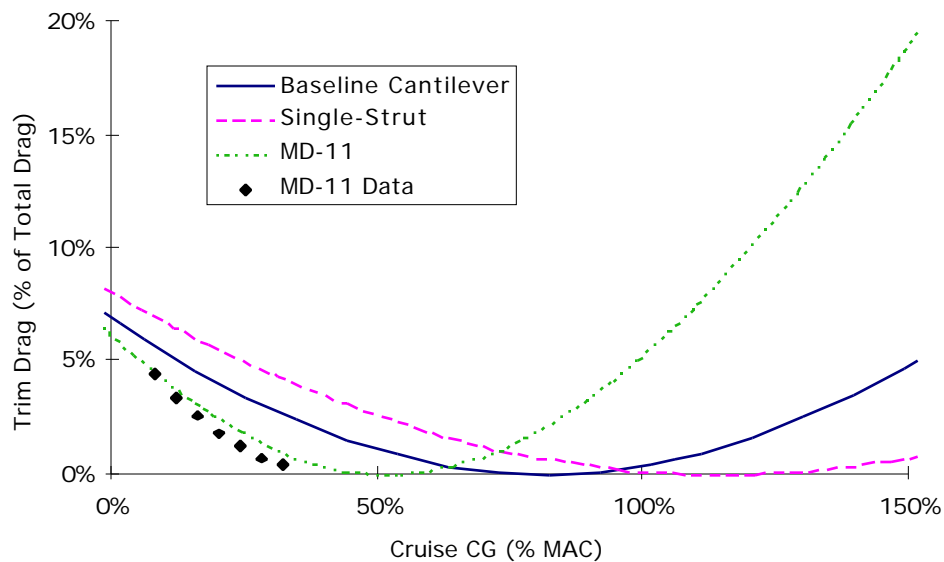
Figure 4-28: Trim drag vs. cruise CG position

4.14. Optimum Load Distributions

The induced drag code determines the optimum load distribution corresponding to minimum induced drag using a Trefftz plane analysis. This method requires the specification of the design lift coefficient, and it has the option to specify a desired pitching moment coefficient. For the advanced technology optimum cantilever and optimum single-strut designs, the optimum load distribution was determined without specifying a pitching moment constraint. This means that the CG would have to be at the point of minimum trim drag in Figure 4-28. The size of the horizontal tail was held fixed to the size of the Boeing 777 horizontal tail for all configurations.

The optimum load distributions for the wing, strut, and horizontal tail on the optimum single-strut design with tip-mounted engines are shown in Figure 4-29 for a CG position at 110% of the mean aerodynamic chord. At this CG position, the tail is actually lifting. The strut carries a small load relative to the wing, and the strut load becomes slightly negative near the wing-strut intersection. This may be beneficial in reducing the interference drag by providing a high pressure area inside the wing-strut intersection, which could help prevent a local shock. The discrete jump in the wing load distribution at the wing-strut intersection is necessary to make up for the negative load carried by the strut. For nearly planar configurations, the minimum induced drag occurs when the sum of all of the load distributions is elliptic. This is also why the inboard region of the wing load distribution is flat. The addition of the elliptic horizontal tail load over this region makes the sum of the load distributions elliptic.

The lift coefficient distribution for the optimum single-strut design is shown in Figure 4-30 for a CG position at 110% MAC. This lift coefficient distribution corresponds to the average cruise condition. The maximum allowable section lift coefficient constraint is applied at the beginning of cruise when the aircraft is at a higher weight. Since the strut has a small chord and a high load near the root, it has large lift coefficients near the root. At the initial cruise condition, the lift coefficient at the root of the strut reaches the maximum allowable lift coefficient of 0.7.
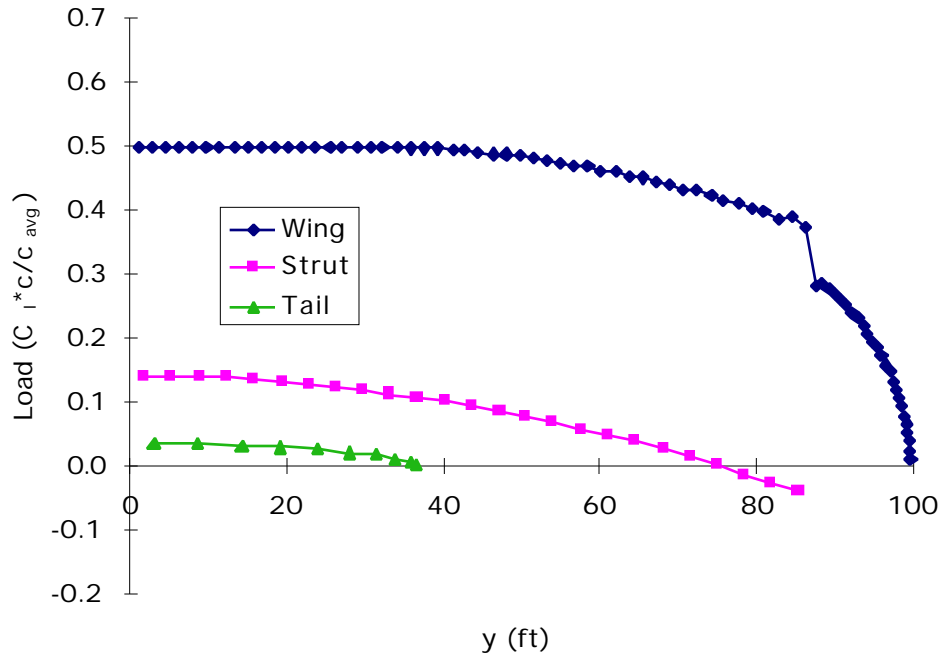
Figure 4-29: Load distribution for single-strut design at CG = 110% MAC
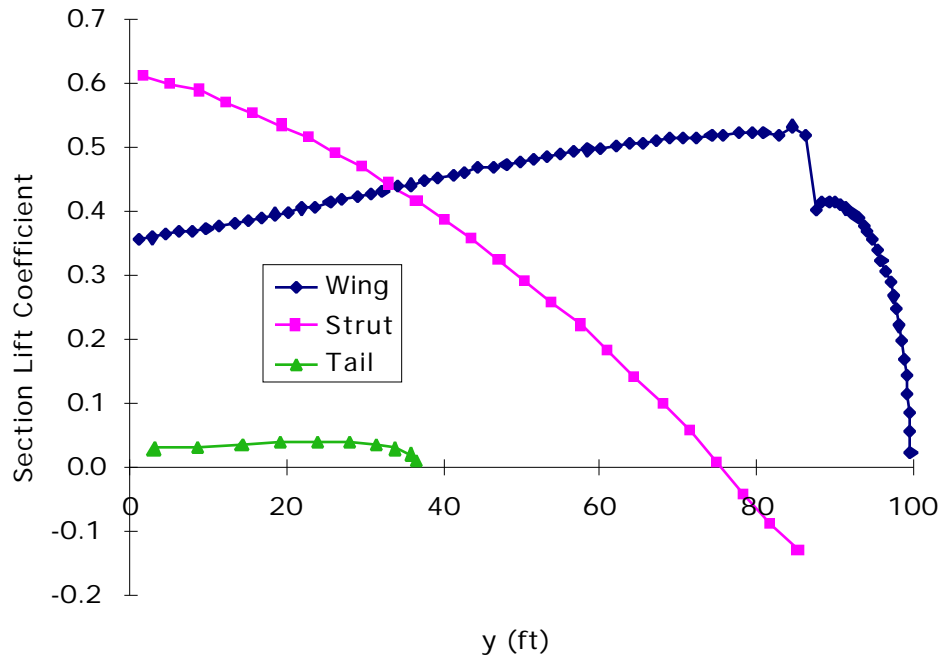
Figure 4-30: Section lift coefficient distribution for single-strut design at CG = 110% MAC

Figure 4-31 shows the load distributions for the optimum single-strut design at a CG position of 25% MAC. This load distribution was created by making the pitching moment constraint active in the Trefftz plane analysis, and setting the desired pitching moment coefficient to zero.

This CG position requires the tail to carry a negative load in order to maintain a zero pitching moment coefficient. Notice that in this case the inboard region of the wing has to carry a higher load in order to compensate for the negative load carried by the tail.

The lift coefficient distributions for the optimum single-strut design at a CG position of 25% MAC are shown in Figure 4-32. The strut lift coefficients have become smaller because the wing is forced to carry a larger load to compensate for the negative load carried by the horizontal tail.
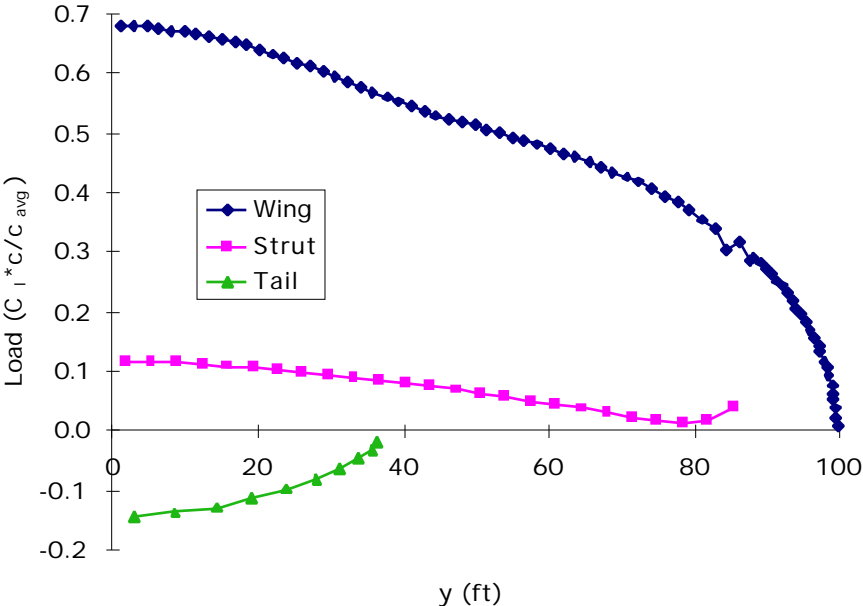
Figure 4-31: Load distribution for single-strut design at CG = 25% MAC
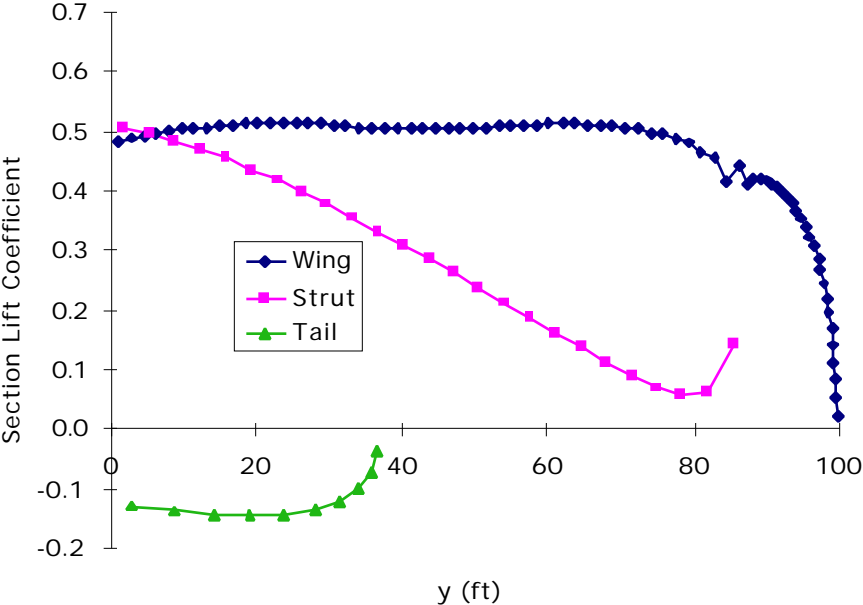
Figure 4-32: Section lift coefficient distribution for single-strut design at CG = 25% MAC

4.15.   *Use of Thrust Vectoring for Engine-Out Control*

The original optimum single-strut configurations presented in Section 4.1 used circulation control on the vertical tail to handle the engine-out flight condition. The engine-out condition may also be handled by placing a third engine at the base of the vertical tail and vectoring the thrust. Table 4-5 shows a comparison between the original optimum single-strut designs (with circulation control) and the designs optimized with thrust vectoring. Figure 4-33 shows the weight breakdown comparison. The original designs have two wing-mounted engines, while the thrust-vectoring designs have two wing-mounted engines and one tail-mounted engine. The thrust vectoring angle was limited to 15˚.

The first two columns of Table 4-5 and Figure 4-33 compare the tip-mounted engine configurations. Since thrust vectoring is not as effective as circulation control in generating a large yawing moment, the span is forced to become smaller on the thrust vectoring design (198.9 ft. to 169.1 ft.). The reduction in span allows the wing weight to go down, but the induced drag increases significantly because of the reduction in span, resulting in an *L/D* of 20.9. The takeoff gross weight of the thrust vectoring design is 26,978 lbs. (5.5%) heavier than the circulation control design.

The second two columns of Table 4-5 and Figure 4-33 compare the under-wing engine configurations. Since the engine position is a design variable in this configuration, the engines can be moved inboard to reduce the yawing moment and satisfy the engine-out constraint. The yawing moment is also reduced by the smaller engine size in the thrust vectoring configuration. Since the total required thrust is divided among three engines instead of two, the thrust per engine is reduced from 58,102 lbs. to 40,013 lbs. The engine moved from 77% of the semispan to 72% of the semispan. Since the engine becomes lighter and moves farther inboard for the thrust vectoring configuration, it provides less inertia relief at the critical structural load cases. As a result, the wing weight increases from 68,070 lbs. to 76,774 lbs. The takeoff gross weight of the under-wing engine thrust vectoring configuration is 43,340 lbs. (9%) higher than the configuration with circulation control.

Table 4-5: Configuration comparison for the use of thrust vectoring for engine-out control

	Tip Engines, Circ. Ctrl.	Tip Engines, Thrust Vectoring	Under-Wing Engines, Circ. Ctrl.	Under-Wing Engines, Thr. Vect.
Wing Span (ft)	198.9	169.1	258.7	258.7
Wing Area (ft^2)	3,829	3,664	3,259	3,567
Aspect Ratio	10.3	7.8	20.5	18.8
Inboard Wing 1/4-Chord Sweep (deg)	27.3	29.8	24.5	25.0
Outboard Wing 1/4-Chord Sweep (deg)	27.3	29.8	24.5	25.0
Strut 1/4-Chord Sweep (deg)	17.7	20.5	16.3	16.2
Wing t/c at the Centerline	13.3%	12.7%	11.9%	12.0%
Wing t/c at the Chord Breakpoint	5.0%	5.0%	5.0%	5.0%
Wing t/c at the Tip	5.0%	5.0%	5.0%	5.0%
Strut t/c	5.0%	5.0%	5.0%	5.0%
Cruise L/D	24.4	20.9	27.8	28.1
Specific Range (nmi/1000 lb)	43.7	35.5	50.6	46.8
Seat Miles per Gallon (seats*nmi/gal)	94.2	80.1	105.2	97.2
Wing Weight (lb)	55,544	46,432	68,070	76,774
Takeoff Gross Weight (lb)	488,990	515,968	481,236	524,576
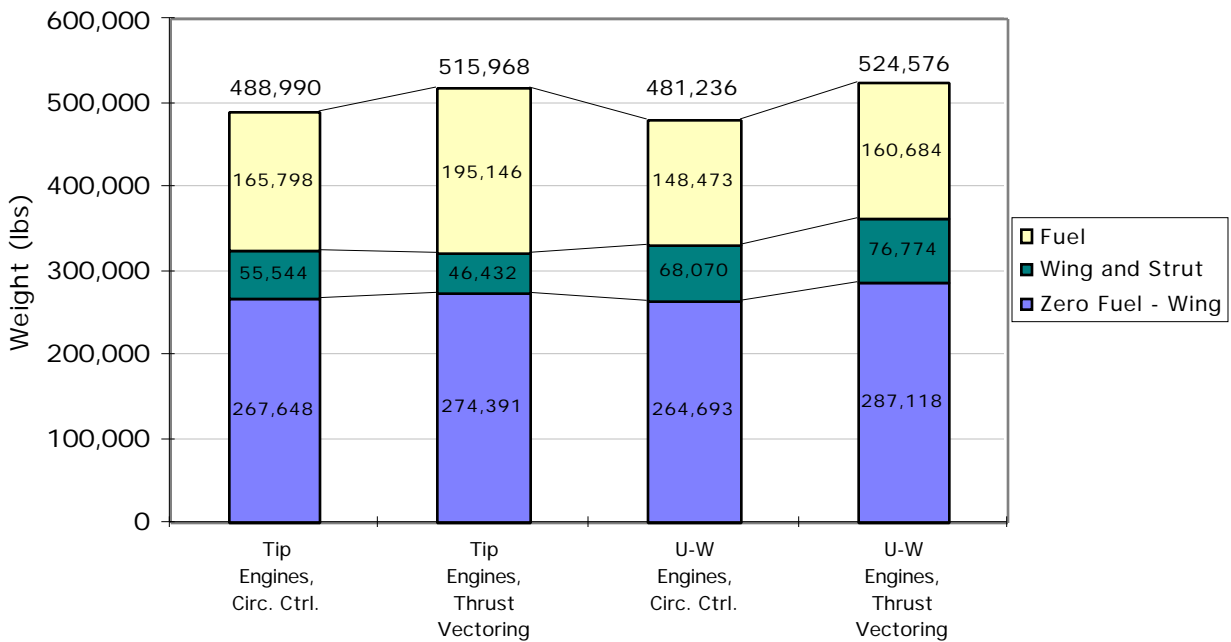
Figure 4-33: Weight comparison for the use of thrust vectoring for engine-out control

4.16.   Use of a Conventional Vertical Tail for Engine-Out Control

The tip-mounted and under-wing engine configurations were also evaluated with the use of a conventional tail for engine-out control. The vertical tail was allowed to scale up with the same proportions as the vertical tail on the Boeing 777. A conventional vertical tail is less effective at generating yawing moments than thrust vectoring or circulation control, but it is the most conservative approach.

Table 4-6 shows the configuration comparison for the tip-mounted engine configurations, and Figure 4-34 shows the weight breakdown comparison. An attempt was made to use a conventional vertical tail with two tip-mounted engines, but a feasible configuration could not be found. A feasible configuration was possible with three engines (two at the tips, one at the base of the vertical tail), because the total required thrust is divided among three engines instead of two, resulting in less thrust per engine. Since the conventional vertical tail is less effective than the use of circulation control, the span is reduced from 198.9 ft. to 176.2 ft. to reduce the yawing moment produced by the tip engine at the engine-out condition. The span reduction allows the wing weight to decrease from 55,544 lbs. to 50,010 lbs., but the induced drag is higher, resulting in an *L/D* reduction from 24.4 to 20.5. The vertical tail is 1.87 times larger than the vertical tail on the Boeing 777.

Table 4-6: Tip engine configuration comparison for the use of a conventional vertical tail for engine-out control

	2 Tip Engines, Circ. Ctrl.	3 Engines (2 Tip), Conv. Tail
Wing Span (ft)	198.9	176.2
Wing Area (ft^2)	3,829	3,801
Aspect Ratio	10.3	8.2
Inboard Wing 1/4-Chord Sweep (deg)	27.3	30.3
Outboard Wing 1/4-Chord Sweep (deg)	27.3	30.3
Strut 1/4-Chord Sweep (deg)	17.7	19.5
Wing t/c at the Centerline	13.3%	13.4%
Wing t/c at the Chord Breakpoint	5.0%	5.0%
Wing t/c at the Tip	5.0%	5.0%
Strut t/c	5.0%	5.0%
Cruise L/D	24.4	20.5
Specific Range (nmi/1000 lb)	43.7	33.7
Seat Miles per Gallon (seats*nmi/gal)	94.2	76.4
Wing Weight (lb)	55,544	50,010
Takeoff Gross Weight (lb)	488,990	532,154
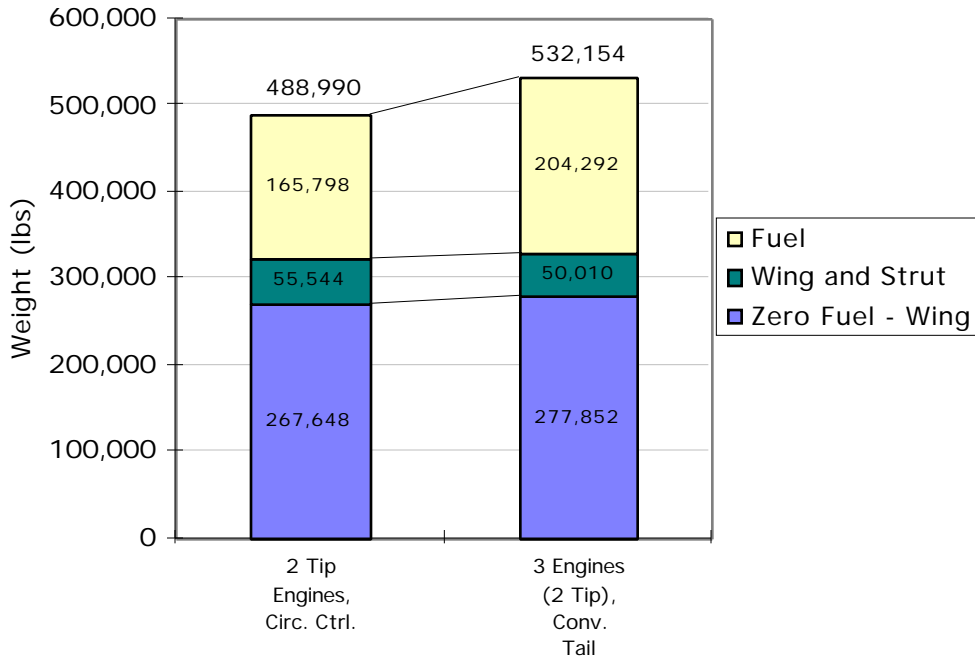
Figure 4-34: Tip engine weight comparison for the use of a conventional vertical tail for engine-out control

Table 4-7 shows the configuration comparisons for the under-wing engine configurations, and Figure 4-35 shows the weight breakdown comparisons. Feasible designs were found for both two-engine and three-engine configurations. The under-wing engine configuration is much more flexible, since the engine position is a design variable, and the engines can be moved inboard until the yawing moment is reduced enough to satisfy the engine-out constraint. The engines are located at 77% of the semispan for the configuration with circulation control. The engine position moves to 49% of the semispan for the two-engine configuration, and 38% for the three-engine configuration. The vertical tail is 73% larger than the Boeing 777 vertical tail for the two-engine configuration, and 22% smaller for the three-engine configuration.

Notice that the engine position is further inboard for the three-engine design (38%) than for the two engine design (49%). This is a counterintuitive result, since one would expect that the smaller engines of the three-engine configuration could be further outboard than the larger engines of the two-engine design. However, the smaller engines of the three-engine configuration cannot provide as much inertia relief for the wing structure, since they are lighter. Therefore, there is a smaller advantage to having them far outboard on the wing. The optimizer chose to move the engines to 38% of the span and reduce the size of the vertical tail by 22% relative to the Boeing 777 vertical tail, resulting in lower drag and lower weight. This is another

example of a counterintuitive design produced by the optimizer. A human designer may not have arrived at this synergistic configuration using traditional design methods.

The takeoff gross weight of the two-engine conventional tail configuration is 23,833 lbs. (5.0%) greater than the circulation control configuration, and the weight of the three-engine conventional tail configuration is 14,264 lbs. (3.0%) greater.

Table 4-7: Under-wing engine configuration comparison for the use of a conventional vertical tail for engine-out control

	2 U-W Engines, Circ. Ctrl.	2 U-W Engines, Conv. Tail	3 Engines (2 U-W), Conv. Tail
Wing Span (ft)	258.7	242.6	250.9
Wing Area (ft^2)	3,259	3,498	3,361
Aspect Ratio	20.5	16.8	18.7
Inboard Wing 1/4-Chord Sweep (deg)	24.5	25.8	24.6
Outboard Wing 1/4-Chord Sweep (deg)	24.5	25.8	24.6
Strut 1/4-Chord Sweep (deg)	16.3	16.7	16.4
Wing t/c at the Centerline	11.9%	12.0%	11.8%
Wing t/c at the Chord Breakpoint	5.0%	5.0%	5.0%
Wing t/c at the Tip	5.0%	5.0%	5.0%
Strut t/c	5.0%	5.0%	5.0%
Cruise L/D	27.8	25.7	27.7
Specific Range (nmi/1000 lb)	50.6	44.0	48.8
Seat Miles per Gallon (seats*nmi/gal)	105.2	94.8	101.8
Wing Weight (lb)	68,070	71,364	72,019
Takeoff Gross Weight (lb)	481,236	505,069	495,500
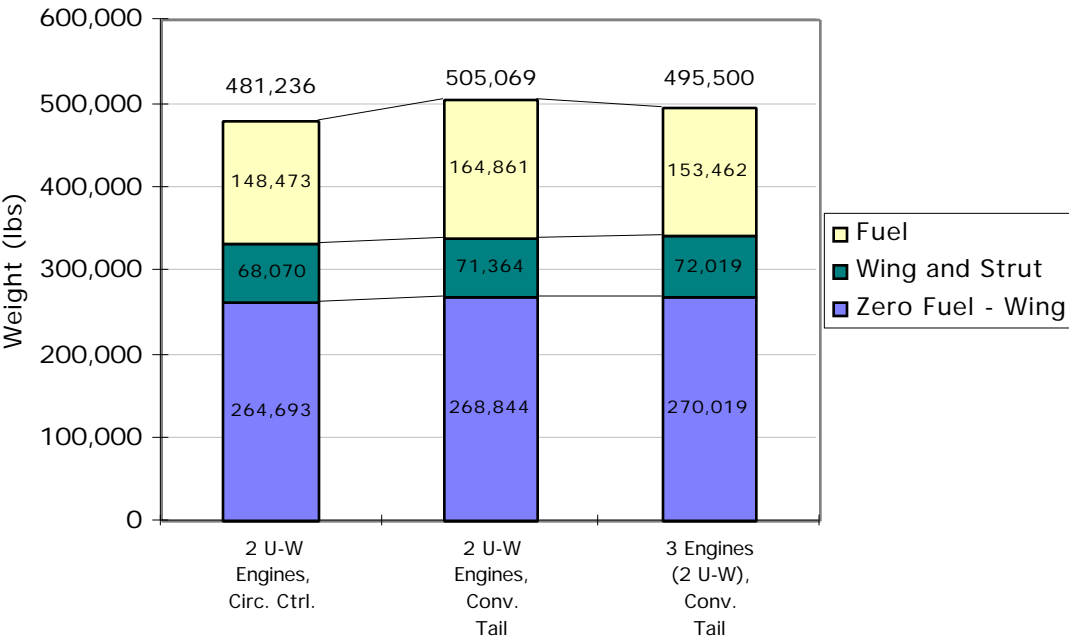
Figure 4-35: Under-wing engine weight comparison for the use of a conventional vertical tail for engine-out control

4.17. Landing Gear Integration

Since the single-strut configurations utilize a high wing, it is not practical to retract the landing gear into the wing. Therefore, it may be necessary to use fuselage-mounted landing gear similar to the gear on a Dornier 128 (Figure 4-36). Since the landing loads would have to be carried around the fuselage to the wing box, an added weight penalty would be associated with fuselage-mounted landing gear. The transonic aerodynamics of the landing gear fairing may also present a detailed design challenge.

Figure 4-36: Dornier 128 landing gear fairing [48]

The landing gear may be integrated with the strut-fuselage intersection to minimize the interference drag and take advantage of some structural synergy. A subsonic example of this concept is shown in Figure 4-37. If the strut chord and depth were very large near the fuselage, the landing gear could possibly be retracted into the strut-fuselage intersection.

Figure 4-37: Landing gear fairing on a Shorts 330 [49]

4.18. *Alternative Objective Functions*

The choice of the objective function used by the optimizer has a strong influence on the shape and performance of the configuration. The most realistic objective function would account for all of the design, manufacturing, operation, maintenance, and disposal issues throughout the entire life of the aircraft, not to mention the political issues. Unfortunately, such a comprehensive objective function cannot be easily expressed in mathematical terms. It may also be difficult to express some objectives (such as manufacturability) in terms of the top-level parameters such as span and sweep that are used at the conceptual design stage.

The takeoff gross weight (TOGW) was chosen as the primary objective function for this study. However, other objective functions were also evaluated. The tip-mounted engine configuration and the under-wing engine configuration were re-optimized for minimum total cost, maximum seat-miles per gallon, and maximum *L/D*. The FLOPS cost model was used to estimate the total cost, which is the sum of acquisition cost (AC), direct operating cost (DOC) and indirect operating cost (IOC).

The configuration comparisons for the objective function sensitivity study with tip-mounted engines are shown in Table 4-8. The weight and cost breakdowns are shown in Figure 4-38 and Figure 4-39, respectively. All four of the tip-mounted engine designs are very similar, with similar performance. The designs are similar because the design space of the tip-mounted engine configuration is highly constrained by the wingtip deflection constraint, and the fixed position of the engine at the tip. This prevents a large increase in span, or a large decrease in wing thickness and sweep to increase the aerodynamic performance.

Table 4-8: Configuration comparison for alternative objective functions (tip-mounted engines)

	Minimum TOGW	Minimum Total Cost	Maximum Seat-Miles per Gallon	Maximum L/D
Wing Span (ft)	198.9	201.2	199.2	199.6
Wing Area (ft2)	3,829	3,834	3,805	3,820
Aspect Ratio	10.3	10.6	10.4	10.4
Inboard Wing 1/4-Chord Sweep (deg)	27.3	28.0	28.4	28.5
Outboard Wing 1/4-Chord Sweep (deg)	27.3	28.0	28.4	28.5
Strut 1/4-Chord Sweep (deg)	17.7	16.8	17.8	17.8
Wing t/c at the Centerline	13.3%	13.6%	12.9%	12.8%
Wing t/c at the Chord Breakpoint	5.0%	5.0%	5.2%	5.2%
Wing t/c at the Tip	5.0%	5.0%	5.2%	5.2%
Strut t/c	5.0%	5.1%	5.1%	5.1%
Cruise L/D	24.4	24.5	24.7	24.7
Specific Range (nmi/1000 lb)	43.7	43.9	43.9	43.6
Seat Miles per Gallon (seats*nmi/gal)	94.2	94.6	94.8	94.8
Wing Weight (lb)	55,544	56,463	57,211	57,860
Takeoff Gross Weight (lb)	488,990	489,059	490,735	492,031
Total Cost ($Million)	1,457.17	1,457.04	1,458.83	1,460.80
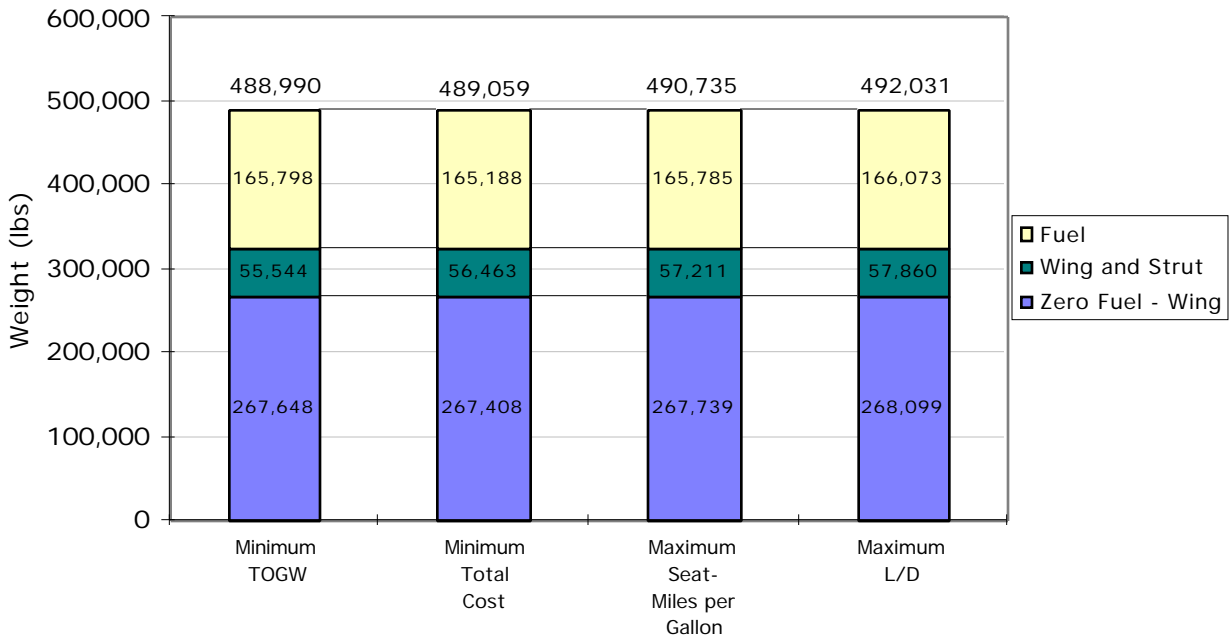
Figure 4-38: Weight comparison for alternative objective functions (tip-mounted engines)
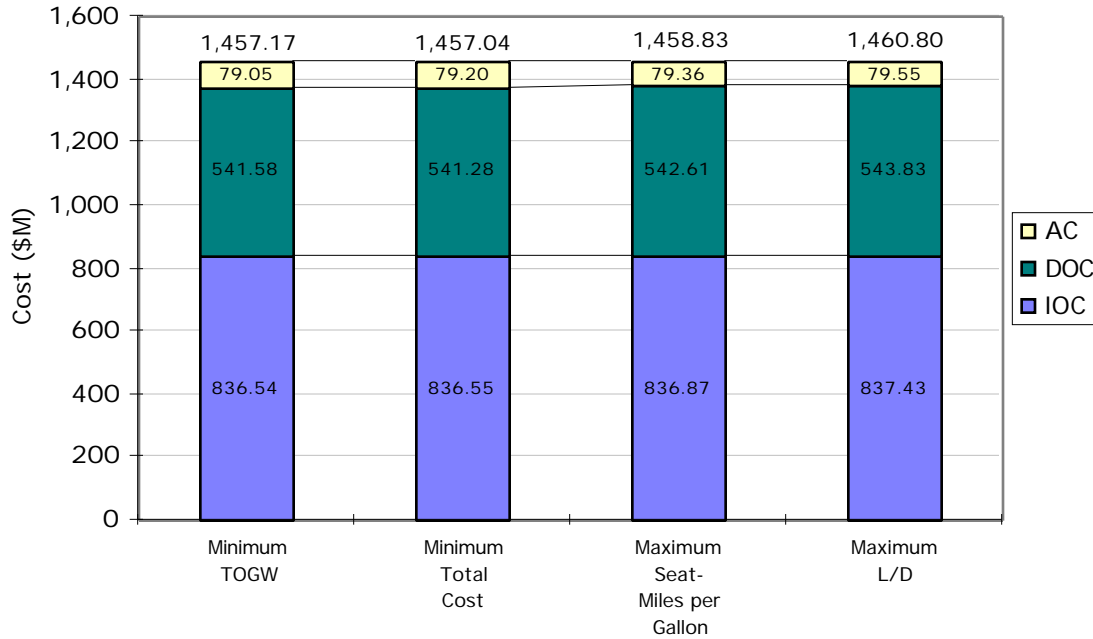
Figure 4-39: Cost comparison for alternative objective functions (tip-mounted engines)

The configuration comparisons for the objective function sensitivity study with under-wing engines are shown in Table 4-9. The weight and cost breakdowns are shown in Figure 4-40 and Figure 4-41, respectively. The design space for the under-wing engine configuration is much more flexible than the design space for the tip-mounted engine configuration. The wingtip deflection constraint is still active for all of the designs, but making the engine position a design variable allows the configuration to evolve more effectively for a given objective function. More design degrees of freedom allow a greater degree of specialization. Since the FLOPS cost estimation method is strongly driven by weight, the configuration optimized for minimum total cost is very similar in shape and performance to the configuration optimized for minimum takeoff gross weight.

The optimizer minimized the fuel weight of the configuration optimized for maximum seat-miles per gallon by increasing the span and decreasing the t/c with almost no increase in wing area. The wing weight is higher relative to the design optimized for minimum TOGW, but the L/D increased from 27.8 to 29.3 and the fuel weight decreased from 148,473 lbs. to 144,058 lbs., resulting in an increase in seat-miles per gallon from 105.2 to 108.4 nmi/1,000 lbs.

The optimizer pushed the span to the 80 meter gate box limit (262.5 ft.) for the configuration optimized for maximum L/D. The wing area increased significantly, along with the wing weight.

This design has an *L/D* of 29.9, while the design optimized for minimum takeoff gross weight has an *L/D* of 27.8. The takeoff gross weight increased from 481,236 lbs. to 507,207 lbs.

Table 4-9: Configuration comparison for alternative objective functions (under-wing engines)

|	Minimum TOGW	Minimum Total Cost	Maximum Seat-Miles per Gallon	Maximum L/D
Wing Span (ft)	258.7	260.0	262.4	262.5
Wing Area (ft2)	3,259	3,257	3,281	4,546
Aspect Ratio	20.5	20.8	21.0	15.2
Inboard Wing 1/4-Chord Sweep (deg)	24.5	24.4	24.3	25.3
Outboard Wing 1/4-Chord Sweep (deg)	24.5	24.4	24.3	25.3
Strut 1/4-Chord Sweep (deg)	16.3	16.1	16.9	17.2
Wing t/c at the Centerline	11.9%	11.8%	10.7%	10.1%
Wing t/c at the Chord Breakpoint	5.0%	5.0%	5.0%	5.0%
Wing t/c at the Tip	5.0%	5.0%	5.0%	5.0%
Strut t/c	5.0%	5.0%	5.0%	5.0%
Cruise L/D	27.8	28.0	29.3	29.9
Specific Range (nmi/1000 lb)	50.6	50.9	52.8	51.7
Seat Miles per Gallon (seats*nmi/gal)	105.2	105.7	108.4	105.4
Wing Weight (lb)	68,070	68,819	76,207	89,615
Takeoff Gross Weight (lb)	481,236	481,257	484,926	507,207
Total Cost ($Million)	1,444.41	1,444.22	1,446.17	1,468.42
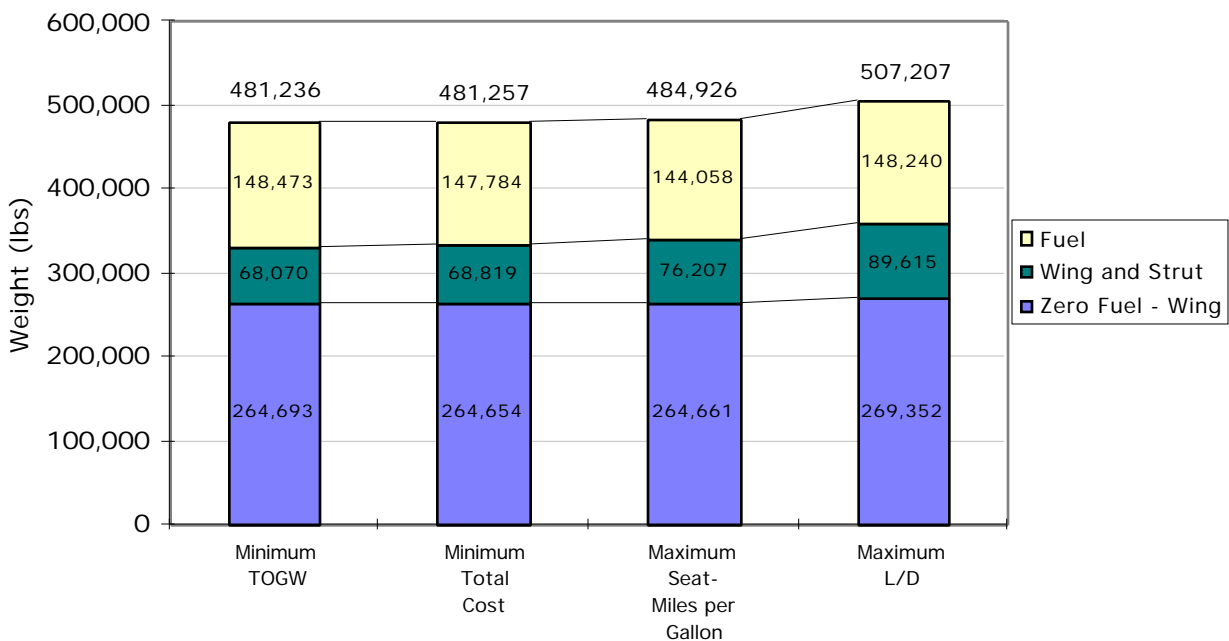
Figure 4-40: Weight comparison for alternative objective functions (under-wing engines)
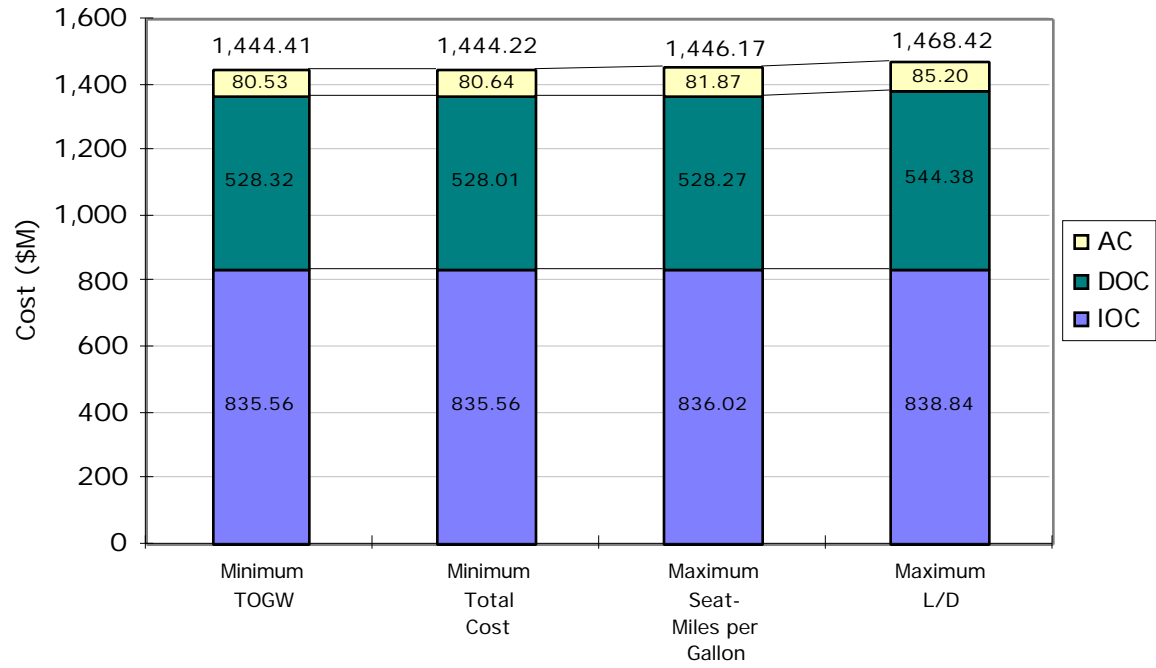
Figure 4-41: Cost comparison for alternative objective functions (under-wing engines)

Chapter 5

Imagineering

In addition to the optimization studies shown above, several brainstorming sessions were held to "imagineer" innovative new design concepts. One of the most promising concepts is the arch-shaped strut, originally conceived by J.A. Schetz [17]. When this strut is placed in tension, it straightens out slightly and acts like a normal strut. However, instead of buckling under compression like a straight, rigid strut, it simply acts like a spring and helps to relieve the bending load.

The arch-shaped strut concept was utilized in the novel configuration shown in Figure 5-1. This configuration features a perpendicular intersection between the wing and struts in the front view, and a chordwise offset of the maximum thickness locations in the plan view. Both of these effects should reduce the interference drag. Additionally, the two struts complement each other by allowing one to be in tension when the other strut is likely to be in compression, thus alleviating the strut buckling problem.
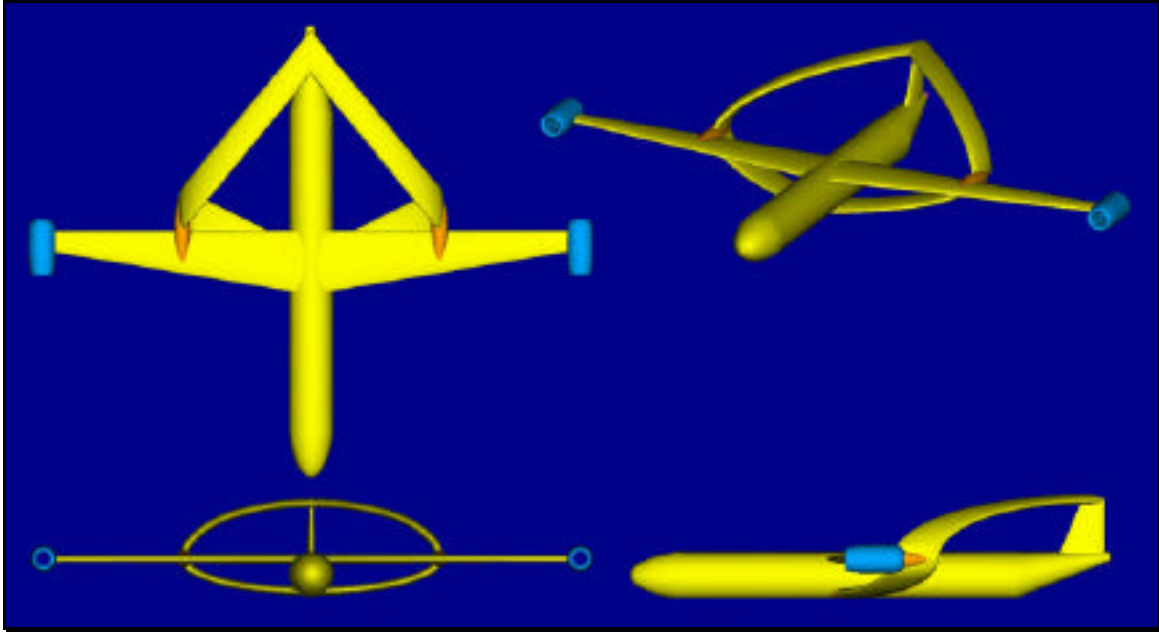
Figure 5-1: Arch-shaped strut configuration

5.1.   Configuration Visualization

When performing MDO studies, it is important to provide the designer with high-quality visual feedback to communicate the shape of the configuration. To meet this goal, a FORTRAN subroutine was written by Mike Libeau [18] to convert the configuration parameters of a given design into a DXF file that can be imported into *AutoCAD* on the PC or *Infini-D* on the Macintosh. These programs can then be used to create three-dimensional, rendered solid models of the configuration, animations, and virtual reality objects. An example of a rendered solid model with a background scene is shown in Figure 5-2. An animation of the aircraft rotating 360˚ is available through the online version of this document by following this hyperlink.

Figure 5-2: Rendered solid model of the single-strut configuration

We also took the configuration visualization work one step further by creating a plastic solid model of the arch-shaped strut configuration using the *I-DEAS* solid modeling software and the rapid prototyping hardware at Virginia Tech (Figure 5-3). This technology will allow us to easily visualize complex configurations in the future.
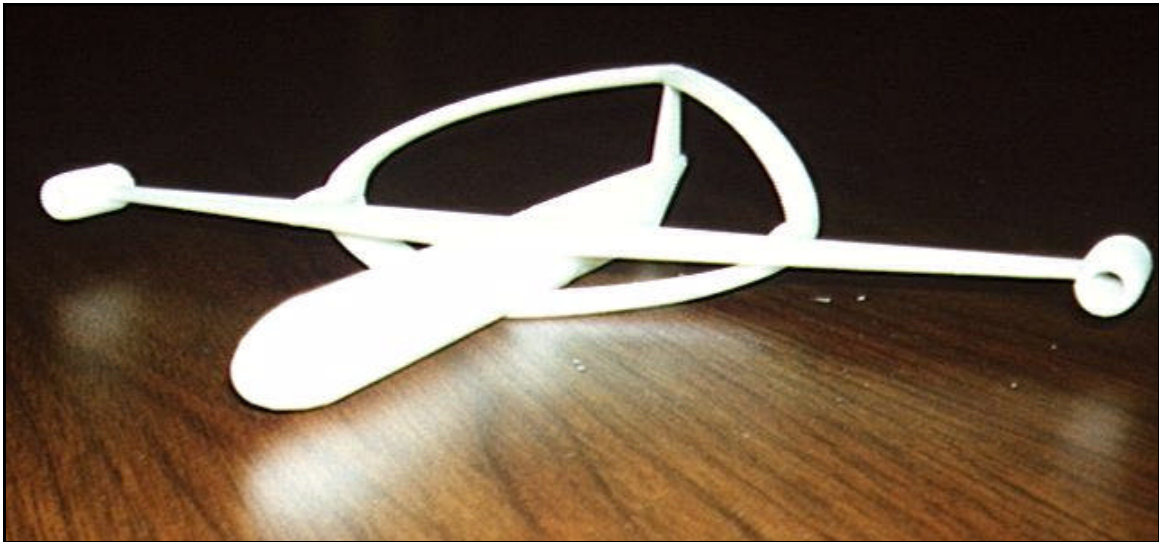
Figure 5-3: Plastic solid model of the arch-shaped strut concept

Chapter 6

Conclusions

The multidisciplinary design optimization approach is absolutely essential for gaining a proper understanding of the nature of the design space and showing the true potential of the strut-braced wing configuration. This study has successfully used MDO to show that the strut-braced wing configuration offers a significant increase in efficiency and decrease in weight and cost relative to a cantilever wing configuration for a large, transonic transport aircraft.

6.1. Advantages of Multidisciplinary Design Optimization

The MDO methodology has many advantages relative to the more traditional design methods. The first advantage of MDO is that it forces the design team to set up a very organized approach to solving the problem. It also forces immediate interdisciplinary interaction instead of a sequential interaction that cycles slowly through each discipline for each design iteration. The end result is that each design created with the MDO methodology obtains the full benefit from the "ripple-through" effect; i.e. an advantage seen in one discipline or subsystem ripples through all of the other disciplines and subsystems. This effectively amplifies the effect of an improvement in one discipline or subsystem on the total system performance.

The most important advantage of MDO is that it helps the design team produce better designs. The optimizer often produces counterintuitive designs, since it is not bound by limited intuition, past experience, and rules of thumb. It also considers the drivers from every discipline and every subsystem simultaneously. The initial response to a counterintuitive design is to look

for a problem with the analysis codes. However, more detailed investigations of the counterintuitive designs usually show very good reasons for the design decisions made by the optimizer. The optimizer also helps the designer to explore the design space more effectively. Parametric trade studies can be performed for a series of optimized design. This means that each design expresses the full potential of a given change in a critical technology or assumption, since the design has re-evolved around the change.

Although the MDO methodology has some significant advantages over the traditional design methodology, there are also some potential pitfalls. The results produced by the MDO methodology can be sensitive to the robustness of the analysis codes, since an optimizer will quickly exploit any weakness in an analysis code. Therefore, the design team should try to ensure that the analysis codes produce accurate results throughout the design space. The MDO methodology should not be viewed as a substitute for expert knowledge and engineering judgement. It is simply another tool in the designer's toolbox, which allows more efficient exploration of the design space.

6.2.   *Advantages of the Strut-Braced Wing Configuration*

The unique advantages of the strut-braced wing configuration can be best understood by tracing the design evolution from a cantilever wing configuration:

- The structural efficiency of the strut is made possible by a novel structural concept allowing the strut to be inactive in compression, and by optimizing the strut force at the 2.5 *g* maneuver load condition.
- The increased structural efficiency provided by the strut can be utilized to reduce the wing weight significantly with a nearly constant span, or the span can be increased to reduce the drag with a smaller wing weight savings.
    - With tip-mounted engines, the span remains under 200 ft., and the wing weight is reduced by 30% relative to the advanced technology cantilever configuration.
    - With under-wing engines, the span is increased to 259 ft., with a wing weight reduction of 14% relative to the advanced technology cantilever configuration.
- The wing *t/c* can be reduced without a large wing weight penalty.
- The smaller *t/c* allows some unsweeping of the wing without a wave drag penalty.
- Lower weight and increased span reduce the induced drag.

- The amount of laminar flow is increased and the parasite drag is reduced for the following three reasons:
    - Unsweeping the wing reduces the cross-flow instability.
    - A higher aspect ratio means smaller chords and smaller Reynolds numbers.
    - Decreasing t/c allows for more favorable pressure gradients and delays the shock formation.
- The taxi bump load condition imposes a natural upper limit on the span. The span of the tip-mounted engine configuration is 198.9 ft. If the spanwise position of the engines is allowed to be a design variable, the engines move to 77% of the semispan and the span increases to 258.7 ft.
- According to the low-speed Hoerner interference drag equations, the wing-strut interference drag is proportional to $(t/c)^3$ and c^2, where the t/c and chord are the average values of the wing and strut. The optimum designs featured a wing and strut t/c of 5% at the wing-strut intersection, and relatively small chords. Therefore, the wing-strut interference drag was predicted to be almost negligible. Future research will be needed to evaluate the transonic effects of the wing-strut intersection using CFD.

The preliminary optimization studies were performed with a single-strut-braced wing, which is the most basic truss-braced configuration. The tip-mounted and under-wing engine single-strut configurations obtain a synergistic increase in overall aircraft efficiency and a large savings in takeoff gross weight relative to the cantilever wing configuration. The configurations are summarized in Table 6-1, and the advantages of the single-strut configurations relative to the cantilever configurations are shown in Table 6-2.

Table 6-1: Configuration summary

	Current Technology Cantilever	Advanced Technology Cantilever	SS with Tip Engines	SS with Under-Wing Engines
Wing Span (ft)	199.9	206.6	198.9	258.7
Aspect Ratio	8.7	9.8	10.3	20.5
Wing Sweep (deg)	31.6	36.7	27.3	24.5
Cruise L/D	18.8	21.7	24.4	27.8
Takeoff Gross Weight (lb)	632,081	568,031	488,990	481,236

Table 6-2: Improvements of the single-strut-braced wing configurations relative to the cantilever wing configurations

Measure of Effectiveness	Relative to Current Technology Baseline Cantilever Configuration		Relative to Advanced Technology Optimum Cantilever Configuration	
	Tip Engine Design	Under-Wing Engine Design	Tip Engine Design	Under-Wing Engine Design
Takeoff Gross Weight	-23%	-24%	-14%	-15%
Fuel Weight	-36%	-42%	-21%	-29%
Operational Empty Weight	-20%	-13%	-16%	-9%
Cruise L/D	30%	48%	12%	28%
Seat-Miles/Gallon	56%	74%	26%	41%

Chapter 7

Future Work

The large performance gains obtained by the truss-braced wing concept rely on several critical assumptions. To reduce the uncertainty associated with the results, these assumptions must be looked at in greater detail in future research.

The first critical assumption is that the wing-strut interference flowfield can be controlled by modern aerodynamic design using CFD. Philippe-Andre Tetrault is currently using an unstructured grid methodology to evaluate the drag of a wing-pylon-store configuration and some representative strut-braced wing configurations.

Another critical assumption is that good aeroelastic characteristics can be obtained without a large weight penalty. Erwin Sulaeman is presently using NASTRAN to assess the aeroelastic properties of a truss-braced wing configuration. Amir Naghshineh-Pour is also developing a NASTRAN analysis to refine the wing bending material weight predictions. Both of these analysis and design efforts are computationally intense. To the extent that the results of these efforts need to be included in the MDO process, they will be represented with response surfaces.

Future research should also identify the weight and power impacts of using circulation control to handle the engine-out flight condition.

The preliminary design studies focused on a single-strut configuration. In the future, arch-strut configurations and multi-element truss configurations should be evaluated. These two concepts may alleviate the strut buckling problem. Load alleviation and the use of composite structures should also be investigated.

References

[1]   Joslin, R.D., "Aircraft Laminar Flow Control," *Annual Review of Fluid Mechanics*, Vol. 30, Annual Reviews Inc., Palo Alto, CA, 1998, pp. 1-29.

[2]   Pfenninger, W., "Design Considerations of Large Subsonic Long Range Transport Airplanes with Low Drag Boundary Layer Suction," Northrop Aircraft, Inc., Report NAI-54-800 (BLC-67), November 1954.

[3]   Gunston, B., *Giants of the Sky: The Biggest Aeroplanes of All Time*, Patrick Stephens Limited, Wellingborough, UK, pp. 249-250.

[4]   Kulfan, R.M., and Vachal, J.D., "Wing Planform Geometry Effects on Large Subsonic Military Transport Airplanes," Boeing Commercial Airplane Company, AFFDL-TR-78-16, Feb. 1978.

[5]   Jobe, C.E., Kulfan, R.M., and Vachal, J.D., "Wing Planforms for Large Military Transports," AIAA-78-1470, 1978.

[6]   Turriziani, R.V., Lovell, W.A., Martin, G.L., Price, J.E., Swanson, E.E., and Washburn, G.F., "Preliminary Design Characteristics of a Subsonic Business Jet Concept Employing an Aspect Ratio 25 Strut-Braced Wing," NASA CR-159361, Oct., 1980.

[7]   Smith, P.M., DeYoung, J., Lovell, W.A., Price, J.E., and Washburn, G.F., "A Study of High-Altitude Manned Research Aircraft Employing Strut-Braced Wings of High-Aspect-Ratio," NASA-CR-159262, February, 1981.

[8]   Ashley, H., "On Making Things the Best–Aeronautical Uses of Optimization," *Journal of Aircraft*, Vol. 19, No. 1, Jan. 1982, pp. 5-28.

[9]   Sobieszczanski-Sobieski, J., Haftka, R.T., "Multidisciplinary Aerospace Design Optimization: Survey of Recent Developments," *Structural Optimization*, Vol. 14, No. 1, 1997, pp. 1-23.

[10]   Kroo, I., "MDO Applications in Preliminary Design: Status and Directions," AIAA 97-1408, 1997.

[11]   Giunta, A.A., Balabanov, V., Haim, D., Grossman, B., Mason, W.H., Watson, L.T., and Haftka, R.T., "Multidisciplinary Optimisation of a Supersonic Transport Using Design of Experiments Theory and Response Surface Modelling," *The Aeronautical Journal*, Oct. 1997, pp. 347-356.

[12] Hutchison, M.G., Unger, E.R., Mason, W.H., Grossman, B., and Haftka, R.T., "Variable-Complexity Aerodynamic Optimization of a High-Speed Civil Transport Wing," *Journal of Aircraft*, Vol. 31, No. 1, 1994, pp. 110-116.

[13] Knill, D.L., Giunta, A.A., Baker, C.A., Grossman, B., Mason, W.H., Haftka, R.T., and Watson, L.T., "HSCT Configuration Design Using Response Surface Approximations of Supersonic Euler Aerodynamics," AIAA 98-0905, 1998.

[14] Patterson, J.C., and Bartlett, G.R., "Evaluation of installed Performance of a Wing-Tip-Mounted Pusher Turboprop on a Semispan Wing," NASA Technical Paper 2739, 1987.

[15] Miranda, L.R., and Brennan, J.E., "Aerodynamic Effects of Wingtip-Mounted Propellers and Turbines," AIAA-86-1802, 1986.

[16] Englar, R.J. and Williams, R.M., "Design of a Circulation Control Stern Plane for Submarine Applications," March 1971, NSRDC Tech. Note AL-200 (AD901-198), Naval Ship Research and Development Center, Bethesda, MD.

[17] Schetz, J.A., Private Communication, Department of Aerospace and Ocean Engineering, Virginia Polytechnic Institute and State University, Blacksburg, Virginia, March, 1997.

[18] Libeau, Mike, Private Communication, Department of Aerospace and Ocean Engineering, Virginia Polytechnic Institute and State University, Blacksburg, Virginia, June, 1997.

[19] Jensen, S.C., Rettie, I.H., and Barber, E.A., "Role of Figures of Merit in Design Optimization and Technology Assessment," *Journal of Aircraft*, Vol. 18, No. 2, February, 1981, pp. 76-81.

[20] Vanderplaats Research & Development, Inc., *DOT User's Manual, Version 4.20*, Colorado Springs, CO, 1995.

[21] McCullers, L.A., *FLOPS User's Guide, Release 5.81*. Text file included with the FLOPS code.

[22] Grasmeyer, J.M., "Truss-Braced Wing Code Description and User's Manual," VPI-AOE-255, Department of Aerospace and Ocean Engineering, Virginia Polytechnic Institute and State University, Blacksburg, Virginia, 24061, January, 1998.

[23] Hoak, D.E. et al., *USAF Stability and Control DATCOM*, Flight Control Division, Air Force Flight Dynamics Laboratory, WPAFB, Ohio, 1978.

[24] Grasmeyer, J.M., "A Discrete Vortex Method for Calculating the Minimum Induced Drag and Optimum Load Distribution for Aircraft Configurations with Noncoplanar Surfaces," VPI-AOE-242, Department of Aerospace and Ocean Engineering, Virginia Polytechnic Institute and State University, Blacksburg, Virginia, 24061, January, 1997.

[25] Braslow, A.L., Maddalon, D.V., Bartlett, D.W., Wagner, R.D., and Collier, F.S., "Applied Aspects of Laminar-Flow Technology," *Viscous Drag Reduction in Boundary Layers*, AIAA, Washington D.C., 1990, pp. 47-78.

[26] Mason, W.H., *FRICTION Code Documentation*, available on the World Wide Web at: http://www.aoe.vt.edu/aoe/faculty/Mason_f/CatxtAppD5.pdf.

[27]   Mason, W.H., "Analytic Models for Technology Integration in Aircraft Design," AIAA-90-3262, September, 1990.

[28]   Malone, B. and Mason, W.H., "Multidisciplinary Optimization in Aircraft Design Using Analytic Technology Models," *Journal of Aircraft*, Vol. 32, No. 2, March-April 1995, pp. 431-438.

[29]   Hilton, W.F., *High Speed Aerodynamics*, Longmans, Green & Co., London, 1952.

[30]   Mair, W.A., and Birdsall, D.L., *Aircraft Performance*, Cambridge University Press, 1992, pp. 255-257.

[31]   Hoerner, S.F., *Fluid-Dynamic Drag*, published by Mrs. Hoerner, 1965. Current address: P.O. Box 65283, Vancouver, WA 98665. Phone: (206)576-3997.

[32]   Raymer, D.P., *Aircraft Design: a Conceptual Approach*, AIAA, Washington D.C., 1992.

[33]   Mattingly, J.D., Heiser, W.H., and Daley, D.H., *Aircraft Engine Design*, AIAA, Washington D.C., 1987.

[34]   Hedges, John. <John.hedges4@virgin.net>, Personal e-mail, April, 1997.

[35]   Naghshineh-Pour, A.H., "Preliminary Structural Analysis of a Truss-Braced Wing," VPI-AOE-256, Department of Aerospace and Ocean Engineering, Virginia Polytechnic Institute and State University, Blacksburg, Virginia, 24061, January, 1998.

[36]   Huang, X., Dudley, J., Haftka, R.T., Grossman, B., and Mason, W.H., "Structural Weight Estimation for Multidisciplinary Optimization of a High-Speed Civil Transport," *Journal of Aircraft*, Vol. 33, No. 3, May-June 1996, pp. 608-616.

[37]   Balabanov, V, Kaufman, M., Knill, D.L., Giunta, A.A., Haftka, R.T., Grossman, B., Mason, W.H., and Watson, L.T., "Dependence of Optimum Structural Weight on Aerodynamic Shape for a High-Speed Civil Transport," AIAA 96-4046, Proceedings of the 6th AIAA/NASA/ISSMO Symposium on Multidisciplinary Analysis and Optimization, Sept. 1996, pp. 599-612.

[38]   Kaufman, M., Balabanov, V., Burgee, S.L., Giunta, A.A., Grossman, B., Haftka, R.T., Mason, W.H., and Watson, L.T., "Variable-complexity response surface approximations for wing structural weight in HSCT design," *Computational Mechanics*, Vol. 18, No. 2, June 1996, pp. 112-126.

[39]   Coster, J.E., and Haftka, R., "Preliminary Topology Optimization of a Truss-Braced Wing," Internal Report, Department of Aerospace Engineering, Mechanics, and Engineering Sciences, University of Florida, Gainesville, Florida, December 1996.

[40]   Haftka, R.T., Private Communication, Department of Aerospace Engineering, Mechanics, and Engineering Sciences, University of Florida, Gainesville, Florida, September 1997.

[41]   Roskam, J., *Methods for Estimating Stability and Control Derivatives of Conventional Subsonic Airplanes*, Roskam Aviation and Engineering Corporation, Lawrence, Kansas, 1971.

[42]   Grasmeyer, J.M., "Stability and Control Derivative Estimation and Engine-Out Analysis," VPI-AOE-254, Department of Aerospace and Ocean Engineering, Virginia Polytechnic Institute and State University, Blacksburg, Virginia, 24061, January, 1998.

[43]   Kulfan, R.M., and Vachal, J.D., "Wing Planform Geometry Effects on Large Subsonic Military Transport Airplanes," Boeing Commercial Airplane Company, AFFDL-TR-78-16, Feb. 1978.

[44]   Sexstone, M.G., Private Communication, Systems Analysis Branch, Aeronautics Systems Analysis Division, NASA Langley Research Center, Hampton, VA 23681-0001, October, 1997.

[45]   *Jane's All the Worlds Aircraft*, Jane's Information Group, Cousldon, Surrey, UK, 1996-1997.

[46]   Torenbeek, E., "Development and Application of a Comprehensive, Design-sensitive Weight Prediction Method for Wing Structures of Transport Category Aircraft," Delft University of Technology Department of Aerospace Engineering, Report LR-693, September, 1992.

[47]   Field, G.G., "MD-11 Design–Evolution, Not Revolution," AIAA 87-2928.

[48]   Mason, W.H., Private Communication, Department of Aerospace and Ocean Engineering, Virginia Polytechnic Institute and State University, Blacksburg, Virginia.

[49]   Dickersbach, Erik. "Shorts 330." <http://www.bslnet.com/accounts/tsimes/wwwerik/shorts.html> (1 April 1998).

Bibliography

Aerodynamics

Moster, G.E., and Venkayya, V.B., "Drag Estimation Using CFD Augmented with Empirical Methods for MDO," 6th AIAA/NASA/USAF Multidisciplinary Analysis & Optimization Conference, Bellevue, WA, AIAA 96-4073, September 4-6, 1996.

Norton, D.A., "Airplane Drag Prediction," *Annals of the New York Academy of Sciences*, V. 154, Art. 2, November 22, 1968, pp. 306-327.

Smith, A.M.O., "High-Lift Aerodynamics," *Journal of Aircraft*, June 1975, pp. 501-530.

Circulation Control

Englar, R.J., "Circulation Control for High Lift and Drag Generation on STOL Aircraft*," J. of Aircraft*, May 1975, pp. 457-463.

Englar, R.J. and Williams, R.M., "Design of a Circulation Control Stern Plane for Submarine Applications," March 1971, NSRDC Tech. Note AL-200 (AD901-198), Naval Ship Research and Development Center, Bethesda, MD.

Design Optimization Tools (DOT)

Vanderplaats Research & Development, Inc., *DOT User's Manual, Version 4.20*, Colorado Springs, CO, 1995.

History

"Anglo-French Aspects: Cross Channel High Aspect Wing Development," *Air Enthusiast*, May/June, 1996, No. 63, pp. 33-37.

Gunston, B., *Giants of the Sky: The Biggest Aeroplanes of All Time*, Patrick Stephens Limited, pp. 249-250.

"H.D.M. 105—Hurel's Aero with Miles' Van," *Flight*, April 19, 1957, pp. 504-505.

Flight Optimization System (FLOPS)

McCullers, L.A., *FLOPS User's Guide, Release 5.81*. Text file included with the FLOPS code.

Induced Drag

Barnes, J.P., "Semi-Empirical Vortex Step Method for the Lift and Induced Drag Loading of 2D or 3D Wings," SAE 975559, Oct. 1997.

Blackwell, J., "Numerical Method to Calculate the Induced Drag or Optimal Span Loading for Arbitrary Non-Planar Aircraft," NASA SP-405, May 1976.

Gray, W.L. and Schenk, K.M., "A Method for Calculating the Subsonic Steady-State Loading on an Airplane with a Wing of Arbitrary Plan Form and Stiffness," NACA TN 3030, Dec. 1953.

Jones, R.T., "Effect of Winglets on the Induced Drag of Ideal Wing Shapes," NASA TM-81230, Sept. 1980.

Kroo, I.M., "A General Approach to Multiple Lifting Surface Design and Analysis," AIAA Paper 84-2507, Oct. 1984.

Kroo, I.M., and Smith, S.C., "Computation of Induced Drag with Nonplanar and Deformed Wakes," Society of Automotive Engineers Transactions, SAE Paper 901933, Long Beach, CA, Sept. 1990.

Kuhlman, J., and Ku, T., "Numerical Optimization Techniques for Bound Circulation Distribution for Minimum Induced Drag of Nonplanar Wings: Computer Program Documentation," NASA CR-3458, 1982.

Lamar, J., "A Vortex Lattice Method for the Mean Camber Shapes of Trimmed Non-Coplanar Planforms with Minimum Vortex Drag," NASA TN-D-8090, June 1976.

Mason, W.H., "Wing-Canard Aerodynamics at Transonic Speeds--Fundamental Considerations on Minimum Drag Spanloads," AIAA 20th Aerospace Sciences Meeting, Orlando, FL, AIAA-82-0097, Jan. 11-14, 1982.

Owens, D.B., "Weissinger's Model of the Nonlinear Lifting-Line Method for Aircraft Design," AIAA 98-0597.

Smith, S.C., and Kroo, I.M., "Computation of Induced Drag for Elliptical and Crescent-Shaped Wings," *J. of Aircraft*, July-Aug., 1993, pp. 446-452.

Special Course on Concepts for Drag Reduction, AGARD R-654

van Dam, C.P., "Induced-Drag Characteristics of Crescent-Moon-Shaped Wings," *J. of Aircraft*, Feb., 1987, pp. 115-119.

Interference Drag

Hoerner, S.F., *Fluid-Dynamic Drag*, published by Mrs. Hoerner, 1965. Current address: P.O. Box 65283, Vancouver, WA 98665. Phone: (206)576-3997.

Joined Wing Studies

Gallman, J.W., Smith, S.C., and Kroo, I.M., "Optimization of Joined-Wing Aircraft," *J. of Aircraft*, Nov.-Dec., 1993, pp. 897-905.

Kroo, I.M., Gallman, J.W., and Smith, S.C., "Aerodynamic and Structural Studies of Joined-Wing Aircraft," *J. of Aircraft*, Jan., 1991, pp. 74-81.

Rhodes, M.D., and Selberg, B.P., "Dual Wing, Swept Forward Swept Rearward Wing, and Single Wing Design Optimization for High Performance Business Airplanes," ICAS-82-1.4.2, pp. 496-511.

Samuels, M.F., "Structural Weight Comparison of a Joined Wing and a Conventional Wing," *Journal of Aircraft*, Jun., 1982, pp. 485-491.

Wolkovitch, J., "The Joined Wing: An Overview," *Journal of Aircraft*, Mar., 1986, pp. 161-178.

Large Transport Studies

Arcara, P.C. Jr., and Bartlett, D.W., "Technology Benefits for Very Large Subsonic Transports," AIAA/AHS/ASEE Aerospace Design Conference, Irvine, CA, AIAA-93-1178, Feb. 16-19, 1993.

McMasters, J.H., and Kroo, I.M., "Advanced Configurations for Very Large Subsonic Transport Airplanes," NASA Workshop on Potential Impacts of Advanced Aerodynamic Technology on Air Transportation System Productivity, June 29-July 1, 1993.

Multidisciplinary Design Optimization

Ashley, H., "On Making Things the Best–Aeronautical Uses of Optimization," *Journal of Aircraft*, Vol. 19, No. 1, Jan. 1982, pp. 5-28.

Huang, X., Dudley, J., Haftka, R.T., Grossman, B., and Mason, W.H., "Structural Weight Estimation for Multidisciplinary Optimization of a High-Speed Civil Transport," *Journal of Aircraft*, Vol. 33, No. 3, May-June 1996, pp. 608-616.

Giunta, A.A., Balabanov, V., Haim, D., Grossman, B., Mason, W.H., Watson, L.T., and Haftka, R.T., "Multidisciplinary Optimisation of a Supersonic Transport Using Design of Experiments Theory and Response Surface Modelling," *The Aeronautical Journal*, Oct. 1997, pp. 347-356.

Hutchison, M.G., Unger, E.R., Mason, W.H., Grossman, B., and Haftka, R.T., "Variable-Complexity Aerodynamic Optimization of a High-Speed Civil Transport Wing," *Journal of Aircraft*, Vol. 31, No. 1, 1994, pp. 110-116.

Knill, D.L., Giunta, A.A., Baker, C.A., Grossman, B., Mason, W.H., Haftka, R.T., and Watson, L.T., "HSCT Configuration Design Using Response Surface Approximations of Supersonic Euler Aerodynamics," AIAA 98-0905, 1998.

Kroo, I., "MDO Applications in Preliminary Design: Status and Directions," AIAA 97-1408, 1997.

Malone, B. and Mason, W.H., "Multidisciplinary Optimization in Aircraft Design Using Analytic Technology Models," *Journal of Aircraft*, Vol. 32, No. 2, March-April 1995, pp. 431-438.

Sobieszczanski-Sobieski, J., Haftka, R.T., "Multidisciplinary Aerospace Design Optimization: Survey of Recent Developments," *Structural Optimization*, Vol. 14, No. 1, 1997, pp. 1-23.

Wakayama, S. and Kroo, I., "A Method for Lifting Surface Design Using Nonlinear Optimization," AIAA 90-3290.

Wakayama, S. and Kroo, I., "Subsonic Wing Design Using Multidisciplinary Optimization," AIAA 94-4409.

Wakayama, S. and Kroo, I., "Subsonic Wing Planform Design Using Multidisciplinary Optimization," *J. of Aircraft*, July-August 1995, pp. 746-753.

Northrop Reports

Bacon, J., "Experimental Investigation of Structural Effect of Sweepback on a Strut-Braced Wing," Northrop Aircraft, Inc., Report NAI-54-475 (BLC-47), July 1954.

Bacon, J., and Fiul, A., "WADC 10-foot Transonic Wind Tunnel Tests on Strut-Braced Boundary Layer Airplane," Northrop Aircraft, Inc., Report NAI-57-826 (BLC-99), June 1957.

Fiul, A., "A Preliminary Report on a Comparison of Aero-Elastic Effects on Cantilevered and Strut-Braced Swept Wings," Northrop Aircraft, Inc., Report NAI-58-529 (BLC-111), July 1958.

Pfenninger, W., "Design Considerations of Large Subsonic Long Range Transport Airplanes with Low Drag Boundary Layer Suction," Northrop Aircraft, Inc., Report NAI-54-800 (BLC-67), November 1954.

Schjelderup, H.C., "An Analysis of a Swept Wing-Strut Configuration," Northrop Aircraft, Inc., Report NAI-54-557 (BLC-57), September 1954.

Performance

Torenbeek, E., "Cruise Performance and Range Prediction Reconsidered," *Prog. Aerospace Sci.*, Vol. 33, 1997, pp. 285-321.

Pfenninger Papers

Pfenninger, W., "Design Considerations of Large Global Range High Subsonic Speed LFC Transport Airplanes," Summarized from the report "Some Thoughts on the Design of Large Global Range LFC Transport Airplanes," Jan., 1976. Internal NASA report.

Pfenninger, W., "About All Laminar Flow LFC Airplanes, Oct., 1981. Internal NASA report.

Pfenninger, W., "R and D Investigation for the Development of High Subsonic Speed LFC Transport Airplanes," Jan. 29, 1990. Internal NASA report.

Pfenninger, W., "Large Long Range High Subsonic Speed LFC Transport Airplanes," Nov. 24, 1992. Internal NASA report.

Pfenninger, W., "Ideas About Basic and Applied Research and Technological Developments for Large high Subsonic Speed LFC Transport Airplanes," Dec. 8, 1992. Internal NASA report.

Propulsion

Mattingly, J.D., Heiser, W.H., and Daley, D.H., *Aircraft Engine Design*, AIAA, Washington D.C., 1987.

Stability and Control

Hoak, D.E. et al., *USAF Stability and Control DATCOM*, Flight Control Division, Air Force Flight Dynamics Laboratory, WPAFB, Ohio, 1978.

Roskam, J., *Methods for Estimating Stability and Control Derivatives of Conventional Subsonic Airplanes*, Roskam Aviation and Engineering Corporation, Lawrence, Kansas, 1971.

Tip-Mounted Engines

Kroo, I., "Propeller-Wing Integration for Minimum Induced Loss," AIAA 84-2470.

Miranda, L.R., and Brennan, J.E., "Aerodynamic Effects of Wingtip-Mounted Propellers and Turbines," AIAA-86-1802, 1986.

Patterson, J.C., "Lift-Induced Wing-Tip Vortex Attenuation," AIAA 74-38.

Patterson, J.C. and Bartlett, G.R., "Evaluation of Installed Performance of a Wing-Tip-Mounted Pusher Turboprop on a Semispan Wing," NASA TP 2739, 1987.

Patterson, J.C. and Flechner, S.G., "An Exploratory Wind-Tunnel Investigation of the Wake Effect of a Panel Tip-Mounted Fan-Jet Engine on the Lift-Induced Vortex," NASA TN D-5729, May 1970.

Patterson, J.C. and Flechner, S.G., "Exploratory Wind-Tunnel Investigation of a Wingtip-Mounted Vortex Turbine for Vortex Energy Recovery," NASA TP 2468, 1985.

Snyder, M.H. Jr., "Effects of a Wingtip-Mounted Propeller on Wing Lift, Induced Drag, and Shed Vortex Pattern," Ph.D. Dissertation, Oklahoma State University, May 1967.

Snyder, M.H. Jr. and Zumwalt, G.W., "Effects of Wingtip-Mounted Propellers on Wing Lift and Induced Drag," *J. of Aircraft*, Sept.-Oct. 1969, pp. 392-397.

Witnowski, D.P., Lee, A.K.H., and Sullivan, J.P., "Aerodynamic Interaction Between Propellers and Wings," *J. of Aircraft*, Sept. 1989, pp. 829-836.

Topological Design with Genetic Algorithms

Balabanov, V.O., and Haftka, R.T., "Topology Optimization of Transport Wing Internal Structure," AIAA 94-4414, 1994.

Chapman, C.D., Saitou, K., and Jakiela, M.J., "Genetic Algorithms as an Approach to Configuration and Topology Design," *Advances in Design Automation, Vol. 1*, ASME, 1993, pp. 485-498.

Chapman, C.D., Saitou, K., and Jakiela, M.J., "Genetic Algorithms as an Approach to Configuration and Topology Design," *J. of Mechanical Design*, Dec., 1994, pp. 1005-1012.

Gage, P.J., and Kroo, I.M., "A Role for Genetic Algorithms in a Preliminary Design Environment," AIAA 93-3933.

Gage, P.J., and Kroo, I.M., "Representation Issues for Design by Topological Optimization by Genetic Methods," Department of Aeronautics and Astronautics, Stanford University, 1995, HTML document available via the World Wide Web.

Gage, P.J., Kroo, I.M., and Sobieski, I.P., "Variable-Complexity Genetic Algorithm for Topological Design," *AIAA Journal*, Nov., 1995, pp. 2212-2217.

Truss-Braced Wing Studies

Hurel, M., "The Advantages of High Aspect Ratios," *Interavia*, Volume VII, No. 12, 1952, pp. 695-699.

Jobe, C.E., Kulfan, R.M., and Vachal, J.D., "Wing Planforms for Large Military Transports," AIAA-78-1470.

Kulfan, R.M., and Vachal, J.D., "Wing Planform Geometry Effects on Large Subsonic Military Transport Airplanes," Boeing Commercial Airplane Company, AFFDL-TR-78-16, Feb. 1978.

Park, P.H., "The Effect on Block Fuel Consumption of a Strutted vs. Cantilever Wing for a Short Haul Transport Including Strut Aeroelastic Considerations," AIAA 78-1454.

Smith, P.M., DeYoung, J., Lovell, W.A., Price, J.E., and Washburn, G.F., "A Study of High-Altitude Manned Research Aircraft Employing Strut-Braced Wings of High-Aspect-Ratio," NASA-CR-159262, February, 1981.

Turriziani, R.V., Lovell, W.A., Martin, G.L., Price, J.E., Swanson, E.E., and Washburn, G.F., "Preliminary Design Characteristics of a Subsonic Business Jet Concept Employing an Aspect Ratio 25 Strut-Braced Wing," NASA CR-159361, Oct., 1980.

Virginia Tech Reports

Grasmeyer, J.M., "A Discrete Vortex Method for Calculating the Minimum Induced Drag and Optimum Load Distribution for Aircraft Configurations with Noncoplanar Surfaces," VPI-AOE-242, January, 1997.

Grasmeyer, J.M., "Stability and Control Derivative Estimation and Engine-Out Analysis," VPI-AOE-254, January, 1998.

Grasmeyer, J.M., "Truss-Braced Wing Code Description and User's Manual," VPI-AOE-255, January, 1998.

Naghshineh-Pour, A.H., "Preliminary Structural Analysis of a Truss-Braced Wing," VPI-AOE-256, January, 1998.

Appendix

	Current Technology Baseline Cantilever	Advanced Technology Optimum Cantilever	SS with Tip-Mounted Engines	SS with Under-Wing Engines
Rubber Engine Flag	0	1	1	1
Bending Material Wt. Substitution Flag	1	1	1	1
Configuration Class	0	0	1	1
Vertical Separation at Centerline (ft)	N/A	N/A	20.30	20.30
Spanwise Position of Wing-Strut Intersection	N/A	N/A	0.87	0.82
Spanwise Position of Chord Breakpoint	0.33	0.33	0.87	0.82
Wing Half-Span (ft)	99.96	103.28	99.46	129.35
Inboard Wing 1/4-Chord Sweep (deg)	31.60	36.65	27.34	24.46
Outboard Wing 1/4-Chord Sweep (deg)	31.60	36.65	27.34	24.46
Wing Dihedral (deg)	6.00	6.00	0.00	0.00
Strut 1/4-Chord Sweep (deg)	N/A	N/A	17.69	16.27
Wing-Strut Offset (ft)	N/A	N/A	1.00	1.00
Wing Centerline Chord (ft)	52.00	52.00	27.06	29.26
Wing Chord at Chord Breakpoint (ft)	28.60	25.97	13.73	10.35
Wing Tip Chord (ft)	6.70	6.90	8.74	9.12
Strut Centerline Chord (ft)	N/A	N/A	4.51	4.00
Strut Tip Chord (ft)	N/A	N/A	5.75	5.57
Wing Inboard t/c (average)	13.00%	12.98%	9.18%	8.47%
Wing Outboard t/c (constant)	10.90%	10.54%	5.02%	5.00%
Strut t/c (constant)	N/A	N/A	5.00%	5.00%
Strut Force (lb)	N/A	N/A	176,997	208,617
Wing Vertical Position on Fuselage (ft)	6.60	6.60	-8.00	-8.00
Fuselage Length (ft)	206.00	206.00	206.00	206.00
Fuselage Diameter (ft)	20.30	20.30	20.30	20.30
Fuselage Upsweep (deg)	3.50	3.50	3.50	3.50
Depth of Fuselage at Vertical Tail (ft)	15.60	15.60	15.60	15.60
Baseline Engine Nacelle Length (ft)	24.60	24.60	24.60	24.60
Baseline Engine Nacelle Diameter (ft)	13.10	13.10	13.10	13.10
Pylon Length (ft)	14.70	14.70	14.70	14.70
Pylon Height (ft)	4.10	4.10	4.10	4.10
Pylon t/c	15%	15%	15%	15%
Horizontal Position of Horizontal Tail (ft)	113.00	113.00	113.00	113.00
Vertical Position of Horizontal Tail (ft)	12.00	12.00	5.00	5.00
Horizontal Tail Half-Span (ft)	36.50	36.50	36.50	36.50
Horizontal Tail Sweep (deg)	37.50	37.50	37.50	37.50

	Current Technology Baseline Cantilever	Advanced Technology Optimum Cantilever	SS with Tip-Mounted Engines	SS with Under-Wing Engines
Horizontal Tail Root Chord (ft)	23.00	23.00	23.00	23.00
Horizontal Tail Tip Chord (ft)	7.40	7.40	7.40	7.40
Horizontal Tail t/c	10%	10%	10%	10%
Horizontal Tail Dihedral (deg)	5.00	5.00	5.00	5.00
Horizontal Position of Vertical Tail (ft)	100.00	100.00	100.00	100.00
Vertical Position of Vertical Tail (ft)	15.00	15.00	0.00	0.00
Vertical Tail Span (ft)	33.00	33.00	33.00	33.00
Vertical Tail Sweep (deg)	43.00	43.00	43.00	43.00
Vertical Tail Root Chord (ft)	30.50	30.50	30.50	30.50
Vertical Tail Tip Chord (ft)	8.50	8.50	8.50	8.50
Vertical Tail t/c	12%	12%	12%	12%
Vertical Tail Horizontal Moment Arm (ft)	89.0	89.0	89.0	89.0
Vertical Tail Vertical Moment Arm (ft)	21.0	21.0	21.0	21.0
Rudder Average Chord (ft)	6.2	6.2	6.2	6.2
Rudder Span (ft)	32.0	32.0	32.0	32.0
Maximum Rudder Deflection (deg)	24.0	24.0	24.0	24.0
Maximum Aileron Deflection (deg)	25.0	25.0	25.0	25.0
Vertical Tail Scaling Factor	1.0	1.0	1.00	1.00
Thrust Vectoring Angle (deg)	0.0	0.0	0.0	0.0
Thrust Vectoring Horizontal Moment Arm (ft)	112.0	112.0	112.0	112.0
Thrust Vectoring Vertical Moment Arm (ft)	3.00	3.00	3.0	3.0
Delta CL due to Circulation Control	0.00	0.00	0.84	0.80
Tail Composite Factor	0.70	0.70	0.70	0.70
Ultimate Load Factor	3.75	3.75	3.75	3.75
Flap Ratio	0.42	0.42	0.30	0.30
Composite Use Factor	0.00	0.00	0.00	0.00
Aeroelastic Tailoring Factor	0.00	0.00	0.00	0.00
Strut-Bracing Factor	0.00	0.00	1.00	1.00
Fuselage Fuel Capacity (lb)	0	0	0	0
Number of First Class Passengers	50	50	50	50
Number of Tourist Class Passengers	255	255	255	255
Number of Flight Crew	4	4	4	4
Number of Stewardesses	18	18	18	18
Number of Galley Crew	4	4	4	4
Landing Weight Factor	0.80	0.80	0.80	0.80
Maximum Allowable Wingtip Deflection (ft)	25.00	25.00	25.00	25.00
Percent Chord of Fuel Tank	0.50	0.50	0.50	0.50
Fuel Density (lb/gallon)	6.80	6.80	6.80	6.80
Number of Strips per Fuel Tank	10.00	10.00	10.00	10.00
Fuel Shift Flag	0.50	0.50	0.50	0.50
Fuel Weight (lb)	258,116	209,249	165,798	148,473
Zero-Fuel Weight (lb)	373,901	358,781	323,189	332,758
Number of Engines on Wings	2	2	2	2
Number of Engines on Fuselage	0	0	0	0
Baseline Engine Static Thrust (lb)	90,764	90,764	90,764	90,764

	Current Technology Baseline Cantilever	Advanced Technology Optimum Cantilever	SS with Tip-Mounted Engines	SS with Under-Wing Engines
Baseline Engine Weight (lb)	23,157	23,157	23,157	23,157
Spanwise Position of First Engine	0.32	0.32	1.00	0.77
Spanwise Position of Second Engine	0.00	0.00	0.00	0.00
Static Specific Fuel Consumption ((lb/hr)/lb)	0.2949	0.2949	0.2949	0.2949
Range (nmi)	7,380	7,380	7,380	7,380
Reserve Range (nmi)	500	500	500	500
Mach Number	0.85	0.85	0.85	0.85
Altitude (ft)	36,107	35,987	39,432	41,900
Approach Velocity (kts)	140	140	140	140
CLmax for Zero Sweep	3.30	3.30	3.30	3.30
Max Allowable Section Lift Coefficient	0.70	0.70	0.70	0.70
Airfoil Technology Factor	0.955	0.955	0.955	0.955
Laminar Flow Technology Factor	1.00	1.00	1.00	1.00
Wing Transition Location (x/c)	0.00	-1.00	-1.00	-1.00
Strut Transition Location (x/c)	0.00	-1.00	-1.00	-1.00
Fuselage Transition Location (x/l)	0.00	0.00	0.00	0.00
Tail Transition Location (x/c)	0.00	0.00	0.00	0.00
Symmetry Flag	1	1	1	1
Pitching Moment Coefficient Flag	1	0	0	0
Design Pitching Moment Coefficient	0.00	0.00	0.00	0.00
X CG Position (ft)	35.00	35.00	35.00	35.00
Airfoil Zero-lift Pitching Moment Coefficient	-0.075	-0.075	-0.075	-0.075
Number of Vortices for idrag	100	100	100	100
Number of Strips for fdrag	3	3	3	3
Number of Strips for wdrag	8	8	8	8
Year for Dollar Calculations	2000	2000	2000	2000
Development Start Time (year)	2000	2000	2000	2000
Year of MQT/FAA Certification	2005	2005	2005	2005
Depreciation Period (years)	14	14	14	14
Operational Life (years)	30	30	30	30
Residual Value at End of Life (percent)	10%	10%	10%	10%
Airframe Production Quantity	1,000	1,000	1,000	1,000
Passenger Load Factor (percent)	65	65	65	65
Fuel Price (dollars per gallon)	1.00	1.00	1.00	1.00
Calculated Takeoff Weight (lb)	632,081	568,031	488,990	481,236
Wing Weight (lb)	77,318	79,420	55,544	68,070
Calculated Range (nmi)	7,380	7,379	7,380	7,380
Specific Range (nmi/1000 lb)	25.98	33.47	43.66	50.55
Seat Miles per Gallon (seats*nmi/gal)	60.52	74.66	94.22	105.22
Maximum Total Lift Coefficient	2.81	2.65	2.93	3.00
Maximum Section Lift Coefficient	0.70	0.70	0.64	0.70
Cruise CL	0.46	0.44	0.52	0.69
Cruise L/D	18.77	21.73	24.40	27.80
Induced Drag	0.0077	0.0062	0.0072	0.0073
Fuselage Parasite Drag	0.0047	0.0049	0.0057	0.0068

	Current Technology Baseline Cantilever	Advanced Technology Optimum Cantilever	SS with Tip-Mounted Engines	SS with Under-Wing Engines
Nacelle and Pylon Parasite Drag	0.0016	0.0012	0.0011	0.0014
Wing Parasite Drag	0.0047	0.0043	0.0031	0.0038
Strut Parasite Drag	0.0000	0.0000	0.0002	0.0003
Tail Parasite Drag	0.0021	0.0022	0.0026	0.0031
Wave Drag	0.0019	0.0003	0.0006	0.0010
Wing-Fuselage Interference Drag	0.0016	0.0011	0.0007	0.0009
Wing-Strut Interference Drag	0.0000	0.0000	0.0000	0.0000
Total Drag	0.0243	0.0203	0.0213	0.0247
Dynamic Pressure (lb/ft^2)	239.6	240.9	204.3	181.5
Reference Area (ft^2)	4,607	4,365	3,829	3,259
Aspect Ratio	8.68	9.77	10.34	20.53
Percent of Laminar Flow on Wing	0.0%	9.3%	31.9%	45.8%
Percent of Laminar Flow on Strut	0.0%	0.0%	100.0%	100.0%
Thrust to Weight Ratio	0.29	0.23	0.24	0.23
Wing Loading (lb/ft^2)	137	130	128	148
Fuel Capacity (lb)	410,153	386,507	169,063	191,930
Calculated Engine Weight (lb)	23,157	16,952	14,824	14,089
Required Maximum Thrust (lb)	90,764	66,445	58,102	55,223
Rubber Engine Length (ft)	24.60	21.05	19.68	19.19
Rubber Engine Diameter (ft)	13.10	11.21	10.48	10.22
Required Cn at Engine-Out	0.039	0.030	0.094	0.080
Available Cn at Engine-Out	0.039	0.038	0.094	0.080
Wingtip Deflection at Taxi Bump (ft)	1.68	2.02	25.01	25.00
Cost Per Available Seat Mile (cents)	4.34	3.94	3.50	3.42
Acquisition Cost ($M)	86.99	85.68	79.05	80.53
Direct Operating Cost ($M)	670.21	608.63	541.58	528.32
Indirect Operating Cost ($M)	854.56	846.50	836.54	835.56
Total Cost ($M)	1,611.76	1,540.80	1,457.16	1,444.41
Zero Fuel Weight Constraint	0.00	0.00	0.00	0.00
Range Constraint	0.00	0.00	0.00	0.00
Landing CLmax Constraint	-0.01	0.00	-0.11	0.00
Section Cl Constraint	0.00	0.00	-0.09	0.00
Fuel Capacity Constraint	-0.37	-0.46	-0.02	-0.23
Engine-Out Constraint	-0.01	-0.21	0.00	0.00
Wingtip Deflection Constraint	-0.93	-0.92	0.00	0.00

Vita

Joel Mark Grasmeyer was born on January 9, 1973 in Grand Rapids, Michigan, and he is the oldest of two sons of Ruth and Tom Grasmeyer. His early love of model airplanes led him to attend Purdue University, where he graduated with Highest Distinction with a Bachelor of Science degree in Aerospace Engineering in May of 1996. During his time at Purdue, Joel participated in the co-op program and spent six work sessions with The Aerospace Corporation in El Segundo, California. As a member of the Vehicle Concepts Department, he helped develop a Concurrent Engineering Methodology, and used it to perform the conceptual design of several spacecraft. However, his true love was aircraft, so he joined the Multidisciplinary Analysis and Design (MAD) Center at Virginia Tech as a graduate student in the summer of 1996. Upon receiving his Master of Science degree in Aerospace Engineering in May of 1998, he will join the Design Development Center of AeroVironment Inc. located in Simi Valley, California.